

MACROFIBER PIEZOELECTRIC COMPOSITE FOR
LUNAR EXPLORATION ACTUATOR

by

Isaac Andrew Henslee

A thesis submitted in partial fulfillment
of the requirements for the degree

of

Master of Science

in

Mechanical Engineering

MONTANA STATE UNIVERSITY
Bozeman, Montana

July 2010

©COPYRIGHT

by

Isaac Andrew Henslee

2010

All Rights Reserved

APPROVAL

of a thesis submitted by

Isaac Andrew Henslee

This thesis has been read by each member of the thesis committee and has been found to be satisfactory regarding content, English usage, format, citation, bibliographic style, and consistency and is ready for submission to the Division of Graduate Education.

Dr. David A. Miller

Approved for the Department of Mechanical and Industrial Engineering

Dr. Christopher H.M. Jenkins

Approved for the Division of Graduate Education

Dr. Carl A. Fox

STATEMENT OF PERMISSION TO USE

In presenting this thesis in partial fulfillment of the requirements for a master's degree at Montana State University, I agree that the Library shall make it available to borrowers under rules of the Library.

If I have indicated my intention to copyright this thesis by including a copyright notice page, copying is allowable only for scholarly purposes, consistent with "fair use" as prescribed in the U.S. Copyright Law. Requests for permission for extended quotation from or reproduction of this thesis in whole or in parts may be granted only by the copyright holder.

Isaac Andrew Henslee

July 2010

ACKNOWLEDGEMENTS

I would like to acknowledge all those who helped and supported me throughout my masters program. Firstly, I would like to express my appreciation to my lovely wife Kiersten, as well as my Parents and family for always supporting me in my endeavors. I would also like to thank Dr. David Miller, my academic advisor, for the countless hours of discussion and guidance, as well as for always having an open door. I would also like to express my sincere thanks to all the faculty and staff in the Mechanical and Industrial Engineering department at Montana State University for their help and assistance during my time at MSU.

This project was supported by a NASA Graduate Student Research Fellowship from the Applied Physics Laboratory at the Kennedy Space Center. I would like to express my sincere thanks to Curtis Ihlefeld, as well as the Applied Physics Laboratory personnel for providing this opportunity.

TABLE OF CONTENTS

1. INTRODUCTION	1
Motivation for Actuator Development.....	1
Lunar Water Exploration.....	1
Applied Physics Laboratory Experiment	2
Smart Material Actuator	3
Lunar Application Requirements	4
Macro Fiber Composites	6
2. BACKGROUND	9
Piezoelectric Material Overview.....	9
Material Behavior.....	9
Constitutive Modeling.....	12
Piezoelectric Actuators	20
Common Actuator Types	20
Monolithic Actuators:.....	20
Beam Actuators:	21
Stacked Actuators:.....	23
Monolithic Actuator with Interdigitated Electrodes:.....	23
Piezoelectric Fiber Composite Overview	25
Macro Fiber Composite Overview	28
Current MFC Charaterization	29
3. EXPERIMENTAL PROCEDURE.....	33
Experiment Design.....	33
Experimental Specimen	35
Electrical Circuit Design.....	45
Strain Gauge.....	47
Testing Apparatus	48
Instrumentation	51
Aramis Setup and Configuration	53
Cyclical Actuation Fatigue Testing	58
Microstructure Imaging	60
4. EXPERIMENTAL RESULTS AND DISCUSSION	61
Operational Life at Temperature.....	61
MFC Cyclical Performance	63
Tip Displacement	66
Strain comparison:.....	70
Microstructure Imaging	73

TABLE OF CONTENTS – CONTINUED

Specimen Failure	75
5. CONCLUSIONS.....	77
WORKS CITED	79
APPENDIX A: Graphs Showing Displacement and Strain Data for Each Specimen After Each Cyclical Interval	83

LIST OF TABLES

Table	Page
Tolerable Temperature ranges for various components (NASA- JPL)	6
P1 Macro Fiber Composite Material Properties (Smart Material Corporation)	30
Specimen Identifier and Testing Temperature for experiments conducted	61

LIST OF FIGURES

Figure	Page
Thermal Images from NASA's Clementine Spacecraft: (Left) Thermal image showing temperatures from 210 to 329.6K as the darkest and lightest shades respectively; (Right) An un-calibrated composite Image of the moons South Pole where many permanently shadowed craters exist.....	5
Image of Surveyor 3 taken by the Apollo 12 mission of the spacecraft, the Apollo 12 Lunar Module “Intrepid” can be seen in the background (Solar System Exploration).	6
An example of the electric dipole of a) a water molecule, and b) the direction of the resulting electric charge	10
a) Non-oriented electric dipoles are b) exposed to significant electric field for some time resulting in c) a general orientation of the molecular dipoles.....	11
Illustration of the material coordinate system showing the three orthogonal directions and the poling direction in the 3 direction	11
A piezoelectric material shown with an applied force producing an electric displacement or charge flow between the electrodes on the ends of the specimen	14
A piezoelectric material specimen, showing a strain response to an applied electric field	15
The dielectric permittivity provides the relationship between electric displacement and electric field.....	15
The effect of changing the electrical boundary conditions on a specimen a) from an open to closed circuit, effects b) the material compliance.....	16
The mechanical boundary conditions of a) blocked stress, and b) free strain are shown	17
Stress strain curve showing the relationship between blocked stress, free strain and electric field	18
The directional dependence of the piezoelectric strain coefficient is shown.....	19
Monolithic Piezoelectric actuator	21
An extensional actuator consisting of two piezoelectric sections of material sandwiching an elastic substrate shown in the deformed shape	22

LIST OF FIGURES – CONTINUED

Figure	Page
Bending actuator design showing the poling direction of the two piezoelectric components	22
Illustration of a Piezoelectric Stack Actuator	23
Illustration of interdigitated electrodes applied to a monolithic piezoelectric material.....	24
The electric field lines formed from interdigitated electrodes on a piezoelectric material	24
Piezoelectric fiber composite with both a) cylindrical fibers, and b) rectangular fibers ...	26
Expanded view of a MFC patch showing the interdigitated electrodes on polyimide film, the structural epoxy, and the rectangular piezoelectric fibers separated by structural epoxy.....	27
An illustration showing the composition of the MFC's	29
Cantilevered beam experimental design showing the MFC laminated on one side of a stainless steel beam and the entire structure being supported at the base of the beam.....	34
Drawing of the first and second resonant mode shapes for a cantilevered beam	35
Specimen design and dimensions showing location of the MFC, strain gauge and clamping area	36
Cross section of the beam laminate showing the tapered edges of the beam	37
A specimen after the plastic sheets have been peeled off showing a) the MFC side of the beam and b) the strain gauge side of the beam	42
Experimental specimen after the Kapton tape and excess epoxy has been removed showing a) the MFC side of the specimen and b) the Strain gauge side after the wire leads have been trimmed.....	43
The electrical drive circuit used to actuate the macro fiber composite which is electrically modeled as a capacitor	45
The location of each component of the electrical circuit.....	46

LIST OF FIGURES – CONTINUED

Figure	Page
The electrical breadboard from both experimental testing apparatus's showing a) the three low power high voltage modules, and b) the single large higher power high voltage module.....	47
Wheatstone bridge circuit, showing the quarter bridge arrangement used with a temperature compensation strain gauge.....	48
The Testing apparatus showing the temperature compensation strain gauge, thermocouple, grounding wire, and the other components of the apparatus	49
The testing apparatus located inside the Heraeus drying oven. The oven was used to maintain elevated specimen temperatures	50
The testing apparatus located in the Absocold refrigerator. The refrigerator used to cool the testing apparatus.....	51
Voltage divider circuit used to measure the voltage applied to the MFC.....	53
A picture of the GOM Aramis 5m system showing the setup used for taking three dimensional position, displacement, and strain data.....	54
The Aramis system setup showing the setup distances as well as the location of the LED lights.....	55
The global coordinate system for the specimen is shown as the Y direction being parallel to the fiber direction of the MFC, the X direction being in the width direction of the MFC and the Z direction being normal to the plain of the MFC, and positive out of the page.....	56
Drawing of specimen and Aramis image side by side, showing the approximant fiber area, the motion correction area and the three section lines	57
Specimen cast in epoxy, and cut into sections for analysis	60
Results for cyclical fatigue testing indicating cycles to failure with respect to temperature	62
Scatter plot of Cycle number to failure verses temperature indicating the specimens at 20 degrees Celsius and 50 degrees never reached failure	63
Drawing of the test specimen indicating the specimen coordinate system.....	64

LIST OF FIGURES – CONTINUED

Figure	Page
Example of normalized data showing each type of data from the Aramis system, as well as the features used to identify the bottom of the piezoelectric fibers and the plateau used to measure the tip displacement	65
Example Data indicating how the Z position Plateau was used to define the Z displacement data points used in tip displacement measurement	67
Example data showing the Z displacement along the Y section length showing the Y location of the plateau defined by the Z position data, and, the approximate location of the tip displacement measurement	67
Graph showing the location along the Y section of the tip displacement measurement ...	68
Experimental data showing the tip displacement for each specimen at the intervals measured	69
Z displacement data for each cyclical interval of each specimen	69
The Strain data was averaged over the section length containing piezoelectric fibers	71
Strain data shown for specimen S2 T1 after 50 million cycles over the Y section length. The average strain and calculated strain are also shown over the averaging section length	72
Average strain for each cyclical interval of each specimen shown alongside the calculated strain	72
Microstructure image of an un-cycled MFC, showing the components that make up the composite. The piezoelectric fibers show no cracking or evidence of degradation ...	73
Microstructure image of a failed specimen showing cracking within the piezoelectric fibers	74
Microstructure image along the Y cross section comparing cracking in the piezoelectric fibers a) of a failed specimen, and b) a un-cycled MFC	75
Specimen S4 T3 with the point of failure indicated	76
Normalized displacement and strain data for S2 T1 after 50 million cycles	84
Normalized displacement and strain data for S2 T1 after 78 million cycles	84

LIST OF FIGURES – CONTINUED

Figure	Page
Normalized displacement and strain data for S2 T1 after 131 million cycles	85
Normalized displacement and strain data for S2 T1 after 188 million cycles	85
Normalized displacement and strain data for S2 T1 after 250 million cycles	86
Normalized displacement and strain data for S3 T2 after 0 cycles.....	86
Normalized displacement and strain data for S4 T3 after 0 cycles.....	87
Normalized displacement and strain data for S5 T4 after 0 cycles.....	87
Normalized displacement and strain data for S5 T4 after 50 million cycles	88
Normalized displacement and strain data for S6 T5 after 0 cycles.....	88
Normalized displacement and strain data for S6 T5 after 100 million cycles	89
Normalized displacement and strain data for S6 T5 after 150 million cycles	89
Normalized displacement and strain data for S6 T5 after 200 million cycles	90
Normalized displacement and strain data for S6 T5 after 250 million cycles	90
Normalized displacement and strain data for S7 T6 after 0 cycles.....	91
Normalized displacement and strain data for S7 T6 after 50 million cycles	91
Normalized displacement and strain data for S7 T6 after 100 million cycles	92
Strain data compared to the average strain and calculated strain for the specified section length for S2 T1 after 50 million cycles	92
Strain data compared to the average strain and calculated strain for the specified section length for S2 T1 after 78 million cycles	93
Strain data compared to the average strain and calculated strain for the specified section length for S2 T1 after 131.3 million cycles	93
Strain data compared to the average strain and calculated strain for the specified section length for S2 T1 after 188 million cycles	94

LIST OF FIGURES – CONTINUED

Figure	Page
Strain data compared to the average strain and calculated strain for the specified section length for S2 T1 after 250 million cycles	94
Strain data compared to the average strain and calculated strain for the specified section length for S3 T2 after 0 cycles.....	95
Strain data compared to the average strain and calculated strain for the specified section length for S4 T3 after 0 cycles.....	95
Strain data compared to the average strain and calculated strain for the specified section length for S5 T4 after 0 cycles.....	96
Strain data compared to the average strain and calculated strain for the specified section length for S5 T4 after 50 million cycles	96
Strain data compared to the average strain and calculated strain for the specified section length for S6 T5 after 0 cycles.....	97
Strain data compared to the average strain and calculated strain for the specified section length for S6 T5 after 100 million cycles	97
Strain data compared to the average strain and calculated strain for the specified section length for S6 T5 after 150 million cycles	98
Strain data compared to the average strain and calculated strain for the specified section length for S6 T5 after 200 million cycles	98
Strain data compared to the average strain and calculated strain for the specified section length for S6 T5 after 250 million cycles	99
Strain data compared to the average strain and calculated strain for the specified section length for S7 T6 after 0 cycles.....	99
Strain data compared to the average strain and calculated strain for the specified section length for S7 T6 after 50 million cycles	100
Strain data compared to the average strain and calculated strain for the specified section length for S7 T6 after 100 million cycles	100

LIST OF FIGURES – CONTINUED

Figure	Page
Z displacement data showing edges of the plateau used to measure the tip displacement, as well as the approximant location of the tip displacement measurement for S2 T1	101
Z displacement data showing edges of the plateau used to measure the tip displacement, as well as the approximant location of the tip displacement measurement for S3 T2	101
Z displacement data showing edges of the plateau used to measure the tip displacement, as well as the approximant location of the tip displacement measurement for S4 T3	102
Z displacement data showing edges of the plateau used to measure the tip displacement, as well as the approximant location of the tip displacement measurement for S5 T4	102
Z displacement data showing edges of the plateau used to measure the tip displacement, as well as the approximant location of the tip displacement measurement for S6 T5	103
Z displacement data showing edges of the plateau used to measure the tip displacement, as well as the approximant location of the tip displacement measurement for S7 T6	103

ABSTRACT

Understanding the nature and location of water and other resources on Earth's Moon is an essential component to the National Aeronautics and Space Administration's (NASA) space exploration efforts. To aid in these exploration efforts, an investigation into lightweight and reliable materials for a lunar valve actuator design has led to characterizing the lifetime performance of the piezoelectric fiber composite, macro fiber composite (MFC). MFC's are thin rectangular patches made of polyimide film, epoxy and a single layer of rectangular lead zirconium titanate fibers and are commercially available. As a basis for this consideration, the useful life of the MFC is being characterized to determine the effect of temperature on the performance of the material as it is fatigued by cyclical piezoelectric excitation or actuation. The test specimen consist of the MFC laminated to a cantilevered stainless steel beam using epoxy and is actuated at the first resonant frequency of the beam laminate by the cyclic application of 1000 volts. Strain and beam tip displacement measurements are used as a basis for determining the performance of the MFC as it is cyclically actuated under various operating temperatures. The temperature of the beam laminate is held constant during cyclic actuation and cycled to failure or 250 million cycles, to determine the useful life of the MFC over a temperature range from -15°C to 145°C . The results of the experimentation efforts show a strong temperature dependence on operational life for the MFC. No significant degradation in operational performance was identified thru monitoring of the MFC, as the MFC was cyclically actuated up to the point of failure, regardless of temperature or actuation cycle. The results of the experimental testing can be used to better inform designs, such as actuators, using MFC in environments where operational temperatures differ from standard laboratory temperatures, as well as, to better design temperature controlled environments where MFC's are used as actuators.

INTRODUCTION

Motivation for Actuator Development

Lunar Water Exploration

Since its conception, the National Aeronautics and Space Administration, NASA, has been expanding mankind's understanding of the known universe. As part of the process of seeking understanding of the far reaches of the cosmos, an understanding of our own solar system must also be obtained. This understanding is not only for the simple sake of understanding mankind's immediate cosmic neighborhood. But, by taking small steps into the expanses of space, mankind has been developing the critical technology, and knowledge that will enable us to continue pursuing an understanding of the far reaches of the known universe. For this reason, a large part of the current space exploration has, and still is, being focused on our own solar system.

NASA's Constellation program continues in this effort by building the spacecraft that will allow humans continue pushing farther into our own universe. NASA's goal is to first establish a lunar outpost from which the moon can not only be studied, but, experience can be gained that will enable mankind to push even farther into our own solar system. By using this outpost as a stepping stone into our solar system, NASA's goal is to continue reaching farther away from earth by place humans on Mars and even farther into our solar system(NASA-Home).

As part of the goal of establishing a lunar outpost, many of the current efforts are being focused on the lunar surface, specifically looking for sources of water, and other resources, in the lunar environment. Finding sources of water, or even the molecular

components that make up water, on the moon would make establishing a lunar outpost a much more feasible endeavor, elevating the need for water to be transported to the moon from the earth. Additionally lunar water could not only be used for drinking, but also for creating oxygen for breathing, and hydrogen that could be used as a fuel source. The possibility of having a fuel source on the moon means that voyages deeper into the solar system could refuel on the moon after consuming most of their fuel escaping earth's orbit, making the efforts to explore deeper into the solar system much more practical(D. D. Williams). Discovering a source of water on the moon is simply another step towards realizing the larger goal of a lunar outpost, and exploring deeper into the known universe.

The question of if water exists on the moon has been asked for some time, however, only recently has significant effort been focused on finding it, resulting in multiple spacecraft being sent to the moon in search water on Earth's Moon(Levy and Phillips). This effort has resulted in the confirmation that water and hydroxyl molecules exist within the first few millimeters of the lunar surface in 2009, specifically in the Polar Regions (Brown).

Applied Physics Laboratory Experiment

As part of this effort, the Applied Physics Laboratory at NASA's Kennedy Space Center, or KSC, has developed, built, and tested a prototype of an experiment, intended to be carried on a future lunar exploration rover. This experiment would test for the presence water, as well as other compounds such as nitrogen gas, in the permanently shadowed craters on the south pole of Earth's Moon. The experiment would provide further information as to the presence and location of water on and in the lunar regolith.

The concept is that a lunar rover carrying the experiment would travel into one of the permanently shadowed craters in the Aitken basin on the southern pole of the moon. The experiment would process samples of lunar regolith, excavated by another component of the rover. The regolith would be deposited into a sealed chamber where is heated to well above the boiling temperature for water at the pressure of the chamber, releasing the gasses of interest from within the regolith. The gaseous content released from the regolith would then be transported through a piping system to different locations within the experiment to be analyzed. As part of the analysis, control gasses, which would be brought from Earth, are also transported to specified locations within the experimental unit. The prototype of the experiment, which was successfully tested during a field test on a Hawaiian volcano, utilized a significant number of conventional, electromechanical solenoid valves to control the flow of the gasses.

The solenoid valves offered repeatable control of the gas flow within the system, however, there were several drawbacks associated with the use of the solenoid valve. The solenoids were heavy due to the permanent magnet and coil windings within the solenoid valve. Current is required to maintain the non-default position of the solenoid which consumes power and results in joule heating of the coil windings in the valves, putting the valves at risk for overheating.

Smart Material Actuator

As an alternative to the conventional solenoid valve technology, and to minimize the weight of the valve, the current work was focused on characterizing a smart material for use in a valve actuator application. The work was focused on qualifying a material as to its

ability to be used in a valve actuator design. The criteria for evaluating the material will be focused on the lunar application, with specific attention being given to the areas of reliability, cyclic actuation, and the effects of operating under a variety of thermal environments.

Lunar Application Requirements

To understand the environment that any designed components for lunar exploration must both withstand and operate under; two areas of focus were identified. The first area of focus was to define the surface temperature of the permanently shadowed portions of the Aitken Basin on the moons south pole, where the equipment would be designed to operate. As the thermal environment for components of the experiment will be controlled, the second area of focus was to define the allowable temperature ranges for components from earlier lunar missions. This temperature data would form a practical basis for defining a realistic thermally controlled environment. These two areas provided temperature data to help define the thermal environment in which the equipment must operate under, and to outline practical expectations for a thermally controlled environment since one will be required for many of the components on the experiment.

NASA has sent numerous spacecraft to orbit and land on the moon, however, only a few passed over the permanently shadowed portions of the Aitken Basin on the moons south pole. NASA's Clementine spacecraft, sent into lunar orbit in the mid-90's, carried a Long Wave Infrared Camera or LWIR, which was used to generate a temperature map of the lunar surface. Clementine systematically mapped many elements of the lunar surface; however, of primary importance are the thermal images of the lunar surface from the LIWR as shown in Figure 1.

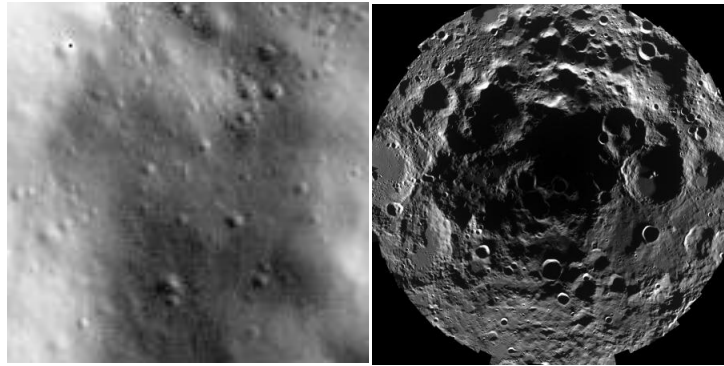


Figure 1: Thermal Images from NASA's Clementine Spacecraft: (Left) Thermal image showing temperatures from 210 to 329.6K as the darkest and lightest shades respectively; (Right) An un-calibrated composite Image of the moons South Pole where many permanently shadowed craters exist.

Due to the very low surface temperature present in the permanently shadowed craters, thermal management systems will be necessary to maintain adequate operating temperatures of equipment operating in these craters, specifically for analyzing gases. To gain a better understanding and expectation of temperatures that could be realistically maintained within this lunar environment, via thermal management systems, the allowable temperature ranges of past spacecraft was investigated. Data regarding various thermally controlled environments from past spacecraft and probes were found from several different components being developed for the surveyor project during the mid-1960. A NASA Jet Propulsion Laboratory (JPL) program summary from 1964 included the temperatures which needed to be maintained for various components within the propulsion system. Acceptable temperature ranges for various components for the Surveyor program were given, data for selected fuel storage tanks, and shock absorbers are given in Table 1. Seven Surveyor Spacecraft landed on the moon from 1966 to 1968 and sent valuable data on the moon back to earth and helped pave the way for the Apollo missions(Solar System Exploration).

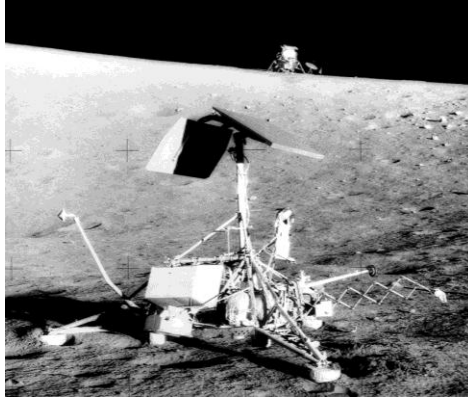


Figure 2: Image of Surveyor 3 taken by the Apollo 12 mission of the spacecraft, the Apollo 12 Lunar Module “Intrepid” can be seen in the background (Solar System Exploration).

Table 1: Tolerable Temperature ranges for various components (NASA- JPL)

Component	Allowable Temperature Range (°F)
RMD Fuel Tanks (fuel and Oxidizer)	0 to 100
RMD Alternate Fuel Tanks (Fuel)	0 to 40
RMD Alternate Fuel Tanks (Oxidizer)	0 to 60
Rocketdyne alternate Tanks (Fuel)	0 to 100
Rocketdyne alternate Tanks (Oxidizer)	20 to 80
Rocketdyne/RMD alternate Tanks (Fuel)	0 to 40
Rocketdyne/RMD alternate Tanks (Oxidizer)	20 to 80
Shock Absorber Case (A)	-20 to 125
Shock Absorber Fluid (B)	20 to 125
Shock Absorber Fluid (C)	20 to 125

Macro Fiber Composites

For use in valve actuators for lunar exploration, macro fiber composites, or MFC's, emerged as the material of choice for a variety of reasons. Typical piezoelectric materials exhibit high cycle lifetimes, specifically when compared to metallic materials (Nuffer, Schönecker and Kohlrautz). However, there are many shortfalls associated with the use of piezoelectric material in the monolithic form. The most significant of these shortfalls being

brittleness, low strain energy density, and a poor ability to be conformed to non-planer surfaces (Wilkie, High and Bockman). MFC's have been designed to overcome many of these material limitations. When compared to many monolithic piezoelectric actuators, MFC's exhibit more desirable reliability, damage tolerance, and flexibility(Sodano, Park and Inman). MFC's have also been integrated into a variety of applications as actuators and sensors. Some of the applications for which MFC's have been used include, health monitoring techniques for unmanned aerial vehicles(Scalea, Matt and Bartoli), automotive drive shafts for vibration control (Whitesides), wing surfaces for geometric control(Kim, Han and Kwon), and underwater surfaces for vibration testing (Schönecker, Daue and Bruckner).

Macro Fiber Composite, commonly referred to as MFC, is a composite material which utilizes thin rectangular piezoelectric fibers suspended in an epoxy matrix. The composite has integrated electrodes which allow activation of the piezoelectric fiber's electro-mechanical properties, causing distortion of the fibers, and thereby allowing displacements to be generated. Although originally designed at NASA's Langley Research Center, MFC is readily available in several different forms from the Smart Materials Corporation, the only known manufacture of the reletivly new piezoelectric fiber composite technology(Schönecker, Daue and Bruckner). The material shows significant promise as it has proven adaptability, and is currently in production, however, limitations exist for use under extreme temperatures, high humidity, as well as high vibration or shock loading (Schönecker, Daue and Bruckner).

In addition to MFC's performance characteristics and application history, MFC's are also commercially available, meaning the consistency and quality control of the material is

controlled within the modern manufacturing environment. Material properties and dimensions are therefore constrained to the capabilities of the manufacturing process and designed tolerances of the MFC system, thereby eliminating the inconsistencies associated with custom manufactured materials. This means that tests performed on the material could be easily repeated elsewhere as essentially the same material could be tested.

BACKGROUND

Piezoelectric Material Overview

Material Behavior

Piezoelectric materials have been commonly used in technical applications for several decades, and have been integrated into many devices commonly used in many technical settings. These devices include many of the different types of accelerometers, load cells, and alignment mechanisms that enable many types of modern research to be possible. These devices exhibit a wide array of features, from high accuracy and sensitivity, to reliability and robust operation. Material limitations do exist, including brittleness, low tensile strength and low material flexibility.

Piezoelectric materials are materials that exhibit a coupling between the mechanical and the electrical states of the material, commonly referred to as an electromechanical coupling. In other words, in a piezoelectric material, the mechanical and electrical conditions that the material is under are linked. Depending on the boundary conditions, the material can produce an electric displacement, or the movement of electrons, when a mechanical load is applied and a mechanical displacement when an electric field is applied to the material. The electrical response due to a mechanical excitation for this class of materials was discovered first and is thus termed the direct piezoelectric effect. The term converse piezoelectric effect therefore refers to an applied electric field generating a mechanical displacement, when not mechanically constrained (Leo).

The electromechanical coupling within these materials exists as a result of the presence of oriented electric dipoles within the material. An electric dipole is a molecular

structure that has a resulting positive charge at one end and a negative charge at the opposite end. As shown in Figure 3, water is a great example of an electric dipole, having resultant positive charge coincident with the two hydrogen atoms, and a resultant negative charge associated with the oxygen atom. The piezoelectric materials electromechanical response is due to the response of these electric dipoles within the ceramic material to an applied mechanical or electric excitation (Srinivasan and McFarland). The electric dipoles are oriented after the material is manufactured by the application of an electric field, similar to that shown in Figure 4. The process of orientating the electric dipoles is referred to as poling the material, and is accomplished by the application of an electric field. The process of poling is generally aided by raising the temperature of the piezoelectric material past its Curie temperature (Srinivasan and McFarland). There are, however, some cases where raising the temperature of the piezoelectric material is not necessary for poling (Williams, Guyhae and Inman).

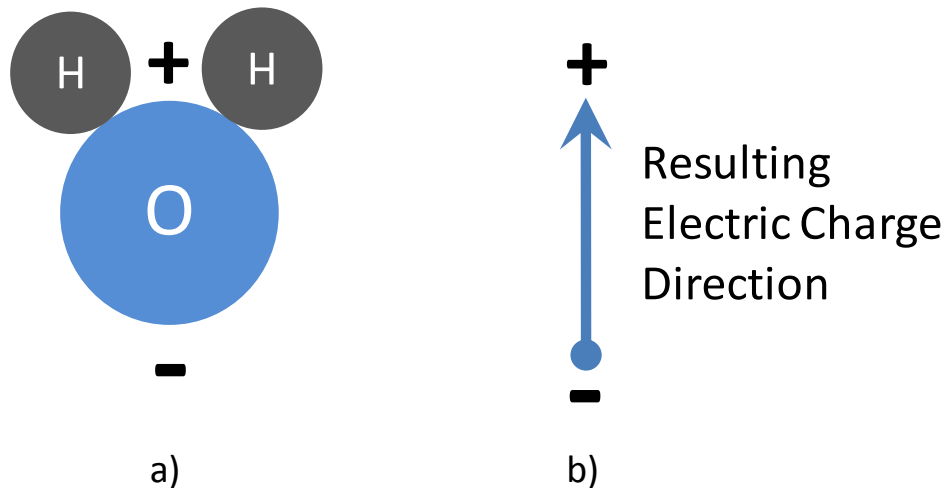


Figure 3: An example of the electric dipole of a) a water molecule, and b) the direction of the resulting electric charge

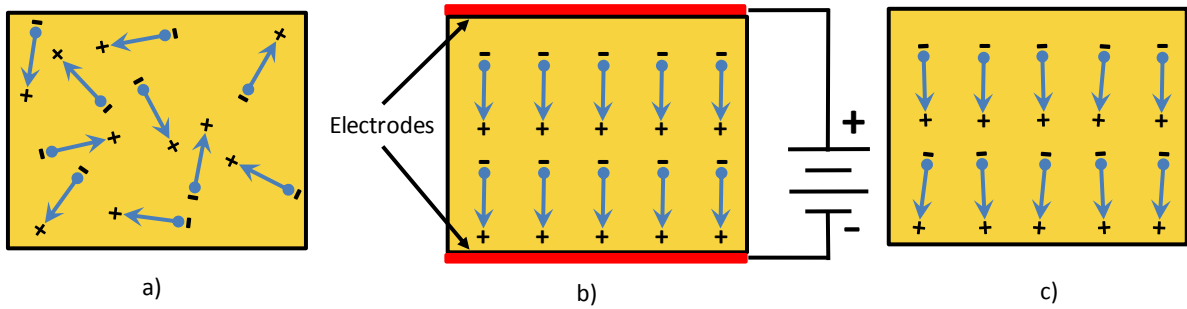


Figure 4: a) Non-oriented electric dipoles are b) exposed to significant electric field for some time resulting in c) a general orientation of the molecular dipoles

The poling direction is commonly used as the basis for a local material coordinate system, which uses three orthogonal axis referred to as the 1, 2, and 3 direction. As shown in Figure 5, it is common practice to take the poling direction as the 3 axes, leaving the 1 and 2 axis being mutually orthogonal to the poling direction (Leo).

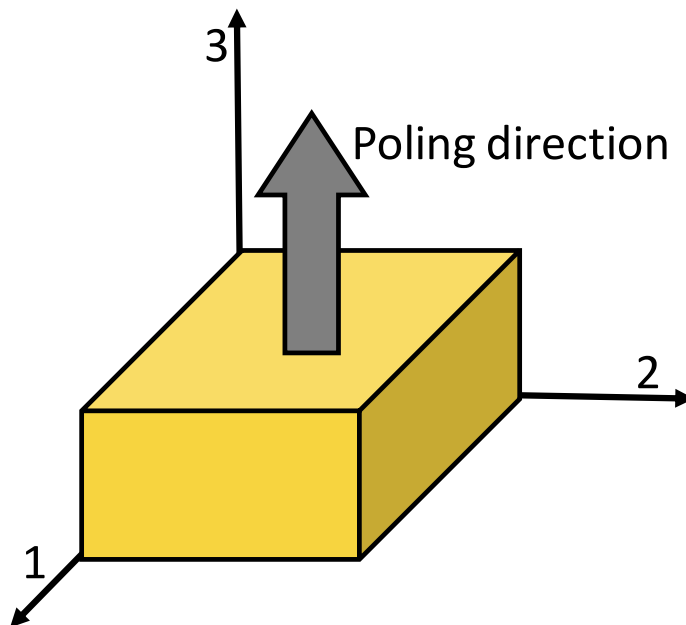


Figure 5: Illustration of the material coordinate system showing the three orthogonal directions and the poling direction in the 3 direction

Constitutive Modeling

The unique coupled mechanical and electrical behavior of piezoelectric materials requires the use of a constitutive model that couples both the electrical and mechanical loading to model both the electrical and mechanical material response. As part of this constitutive model several standard mechanical material properties are used in conjunction with several material properties unique to piezoelectric materials to account for the coupled electromechanical behavior of the piezoelectric material. The material properties used to describe piezoelectric materials consist of the mechanical compliance, s (m^2/N), commonly used in the Hooke's law constitutive model, along with the piezoelectric strain coefficient, d (C/N), and the dielectric permittivity, $\bar{\epsilon}$ (F/m). These material properties are used along with mechanical stress, σ (N/m^2), mechanical strain, ϵ (m/m), electric displacement, D (C/m^2) to model the materials electrical and mechanical response to electrical and mechanical loading conditions. The resulting constitutive equation, shown in equation 1, shows the relationship between the electrical and mechanical elements. The equation is presented in a condensed form, where each component in equation 1 represents a multi-dimensional matrix.

$$1 \quad \begin{Bmatrix} \epsilon \\ D \end{Bmatrix} = \begin{bmatrix} s & d \\ d & \bar{\epsilon} \end{bmatrix} \begin{Bmatrix} \sigma \\ E \end{Bmatrix}$$

This constitutive model, unique to piezoelectric material, contains terms similar to those found in the Hooke's law constitutive equation, which describes the relationship between mechanical stress and strain for an elastic material. This relationship, in an elastic

material, is given by the material compliance, s as can be seen from equation 2. If the piezoelectric effect in equation 1 were set to zero, the equation would simplify the linear elastic constitutive equation found in equation 2.

$$2 \quad \sigma = \frac{1}{s} * \epsilon$$

Stress being the external force on the material per unit area, and for an elastic material is generally a result of an applied load. Stress within a piezoelectric material is generated either by an applied load or generated as a result of other mechanical or electrical boundary conditions. Strain describes mechanical deformation in a material, by means of either electric or mechanical loading conditions.

This piezoelectric constitutive model expands on the Hooke's law model, shown in equation 2, to include the effects of the electromechanical coupling within the piezoelectric material. Take a specimen made of a piezoelectric material as shown in Figure 6, when stress is applied to the specimen, the force causes the material to deform. This deformation causes a displacement of the electric dipoles within the material, which then causes a charge to flow from electrodes placed on the ends of the specimen (Leo). The electric displacement, D , is the electric charge flow produced by the deformation per the cross sectional area of the specimen.

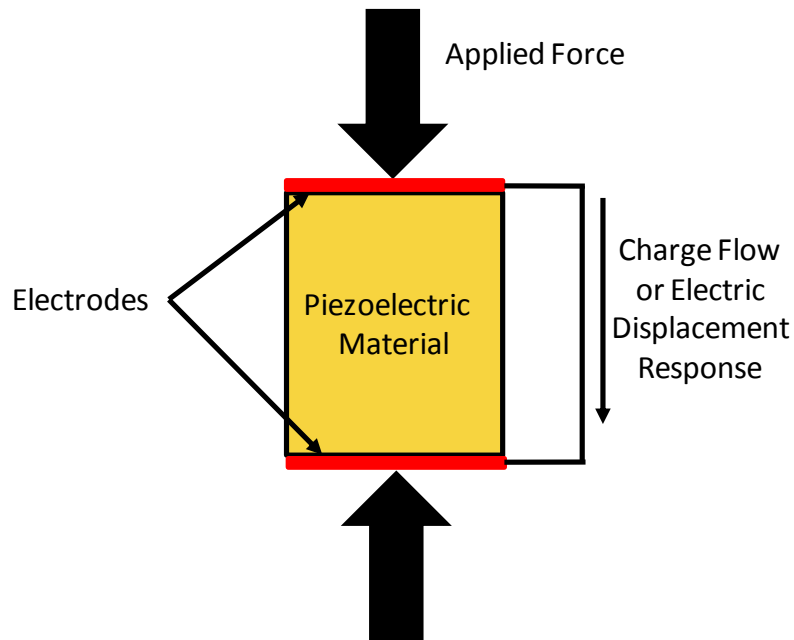


Figure 6: A piezoelectric material shown with an applied force producing an electric displacement or charge flow between the electrodes on the ends of the specimen

The piezoelectric strain coefficient, d , is a material property used to relate the mechanical and electrical conditions within the material. More specifically, the piezoelectric strain coefficient relates the terms for strain and electric field as shown in Figure 7. The piezoelectric strain coefficient represents the coupling between the electrical and mechanical behavior within the material. This can be seen by examining the piezoelectric constitutive equation. In the top row of equation 1, the piezoelectric strain coefficient relates the material strain response to the electric field applied to the material. In the bottom row of equation 1, the piezoelectric strain coefficient relates the material electric displacement to the material stress state. The dielectric permittivity, $\bar{\epsilon}$, is the material property that relates the electric

displacement to the strength of an electric field, as shown in Figure 8 (Leo). The electric field, E , is the applied electric field divided by the thickness of the material.

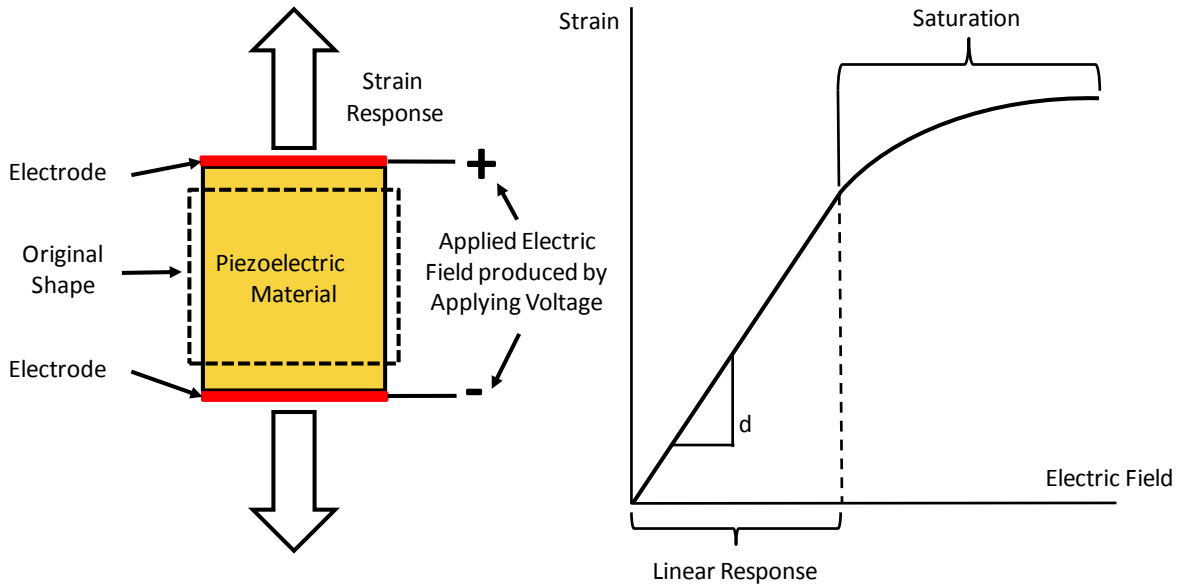


Figure 7: A piezoelectric material specimen, showing a strain response to an applied electric field

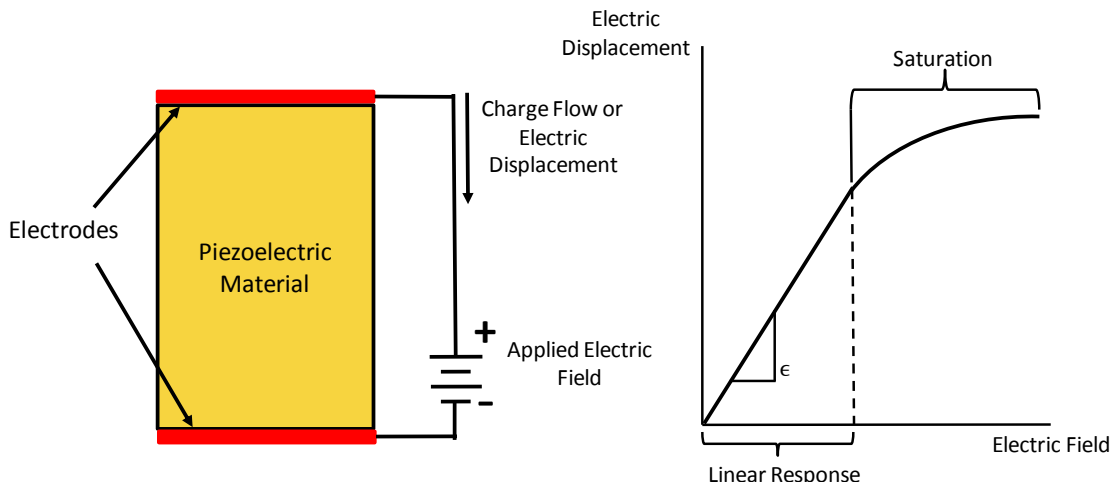


Figure 8: The dielectric permittivity provides the relationship between electric displacement and electric field

The electric and mechanical boundary conditions not only affect the response of an electromechanically coupled material, but these boundary conditions also influence the properties of the material (Leo). Firstly, the electrical boundary conditions can be an open or closed circuit. An open circuit produces no electric displacement but does produce an electric field. This is different from the closed circuit condition which produces an electric displacement but no electric field. Figure 9 shows the relationship between the open and closed circuit conditions, and the material compliance. The open and closed circuits represent the two boundary condition extremes, with an infinite number intermediate conditions possible.

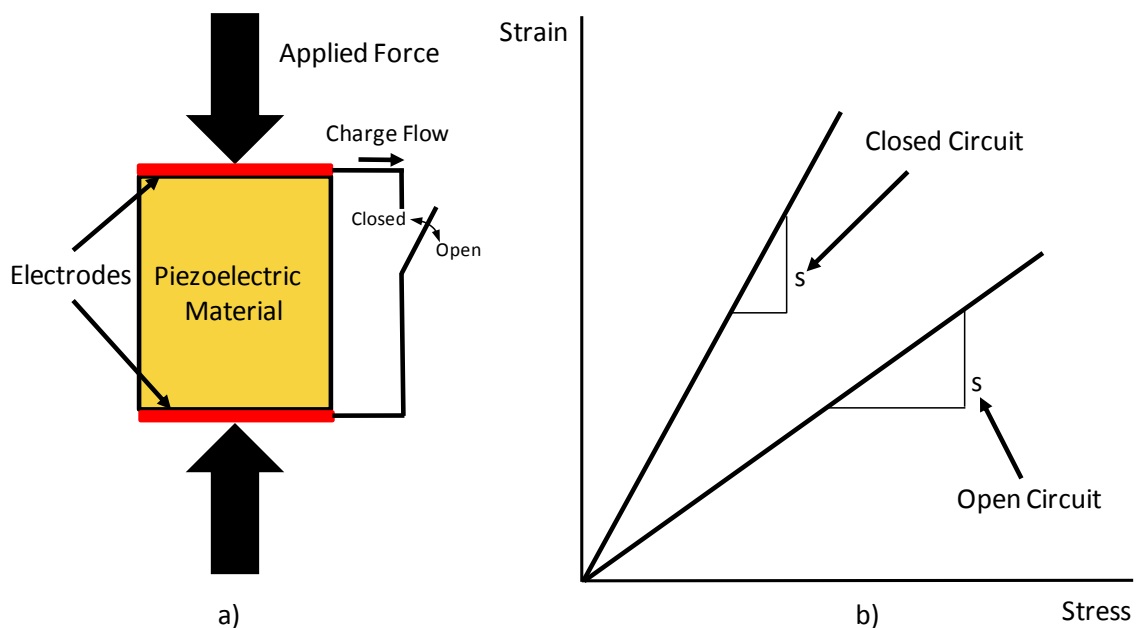


Figure 9: The effect of changing the electrical boundary conditions on a specimen a) from an open to closed circuit, effects b) the material compliance

A similar relationship also exists for the electric permittivity when the mechanical boundary conditions are changed. Just as there were two fundamental electrical boundary

conditions, there are two fundamental mechanical boundary conditions. These conditions are blocked stress and free strain. In the blocked stress boundary condition, the piezoelectric material is constrained to have no strain when an electric field is applied to the material. This boundary condition, shown in Figure 10, can be accomplished by mounting the piezoelectric material in a supporting structure that is much stiffer than the piezoelectric material or relatively ridged when compared to the piezoelectric material. The block stress condition results in a mechanical stress response within the material without a mechanical strain response when an electric field is applied.

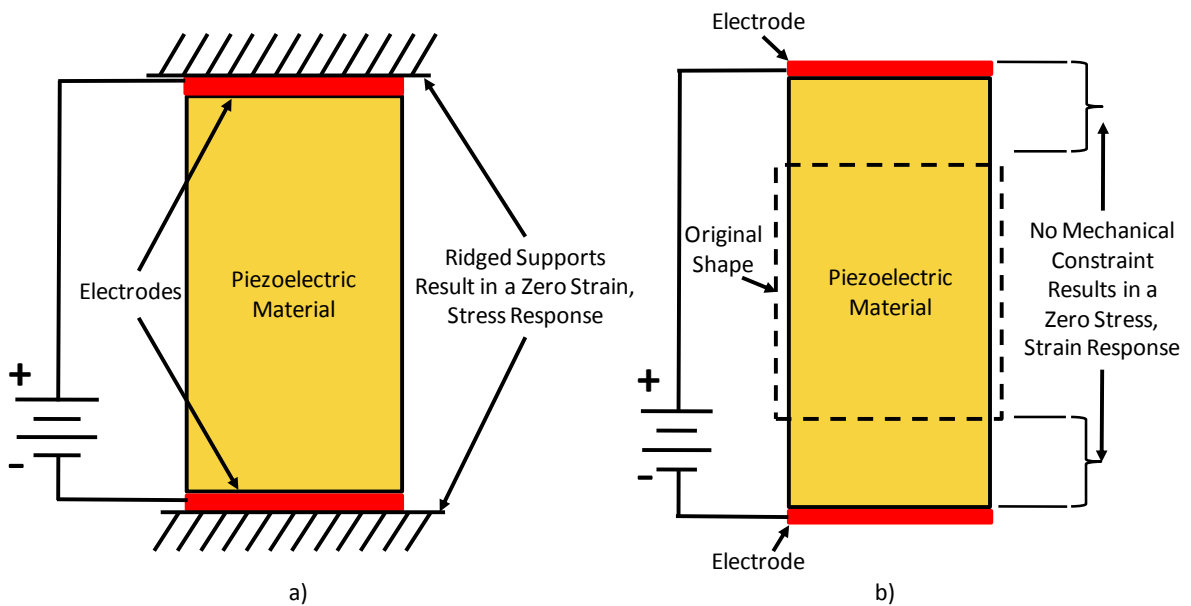


Figure 10: The mechanical boundary conditions of a) blocked stress, and b) free strain are shown

The other boundary condition, referred to as the free strain condition, is that of a structure that is free to deform from the application of an electric field. This mechanical

boundary condition produces zero stress within the material. This means that the material exhibits a stress free strain response to an applied electric field as shown in Figure 10.

The relationship between the blocked stress and free strain condition can be seen by examining a plot on a stress strain diagram. Shown in Figure 11 the curve shows that under the blocked stress condition there is no strain generated, but significant stress is generated within the material. Similarly under the free strain condition, no internal stress is generated by applying an electric field to the material. The mechanical response is limited, therefore, to a strain response. As shown in Figure 11 a linear line between the blocked stress and free strain represents the relationship between stress and strain between these two boundary conditions. The position of this line can change depending on the magnitude of the electric field applied to the material. . The blocked stress and free strain conditions represent the two boundary condition extremes, with an infinite number of intermediate conditions possible.

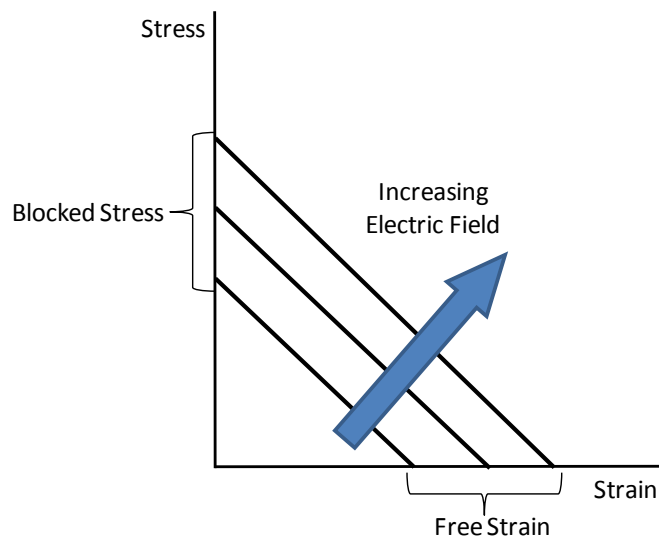


Figure 11: Stress strain curve showing the relationship between blocked stress, free strain and electric field

The piezoelectric constitutive model represents the loading and response of the material in three dimensional space. Therefore the terms within the model are defined, and are represented as multi-dimensional matrixes. The terms within the matrixes are referenced to the material coordinate system. Each material property therefore, also is dependent on the material direction for which it is defined. For example the piezoelectric strain coefficient, d , is a three by six matrix of terms that each represent a directional strain response from a directional electric field. For example, the d_{31} term represents the effect of an electric field in the 3 direction on the strain in the 1 direction. The value of these terms can also vary significantly, as illustrated in Figure 12. As shown the piezoelectric strain coefficient, d_{31} , is significantly lower than the d_{33} term, and has a different sign.

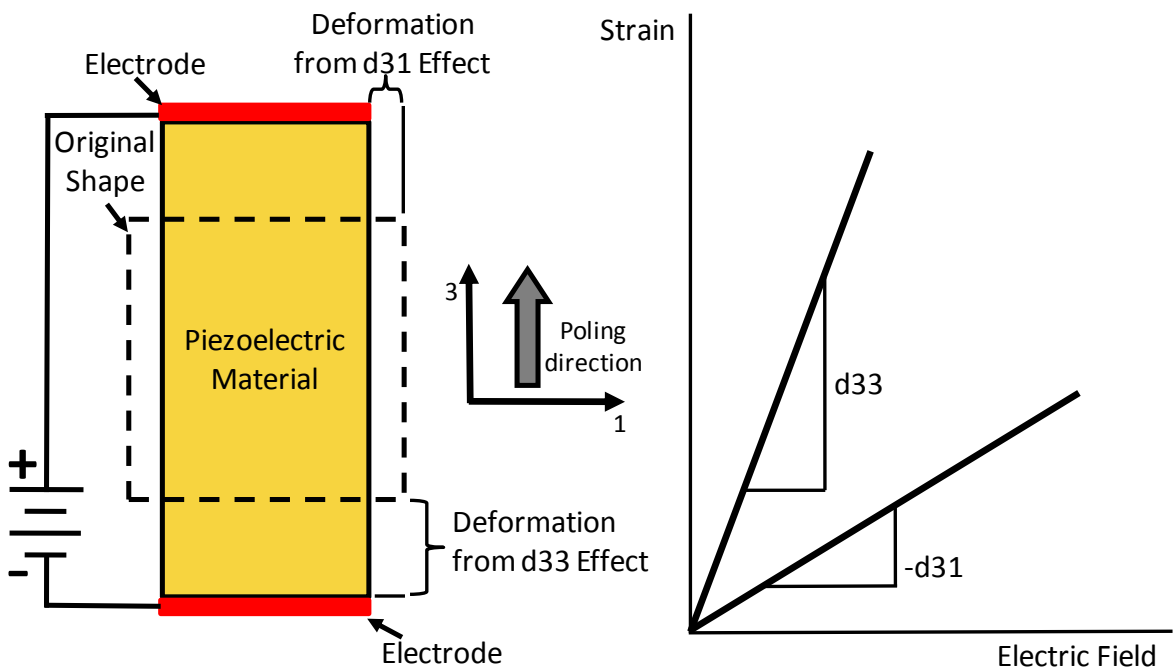


Figure 12: The directional dependence of the piezoelectric strain coefficient is shown

Piezoelectric Actuators

When used as actuators, it is common for piezoelectric materials to have a primary direction of intended operation. The orientation of the electrodes, the poling direction, as well as the manner in which the piezoelectric material is constrained determine this direction. This means that generally only one of the terms in the piezoelectric strain coefficient matrix is in the intended direction of operation. It is therefore common to refer to the various modes of operation by the term in the piezoelectric strain coefficient matrix that dominate the material response. For example the d_{31} mode actuator refers to an actuator that uses the mechanical response in the 1 direction from an applied electric field in the 3 direction.

Common Actuator Types

Monolithic Actuators: One of the simplest applications of a piezoelectric material as an actuator is to use the piezoelectric material in monolithic form. The basic electromechanical relationship of the material can be utilized directly to produce mechanical stress, mechanical strain, electric voltage, or electric displacement from a single, continuous piece of material. Often one drawback to monolithic actuators is that they are required to be thin in order to apply strong enough electric fields at reasonable electrode voltages to generate significant strains in the material. This type of actuator design, as seen in Figure 13 is useful for generating small but precise displacements or even to produce audible sound(Leo)(Omega Piezo).

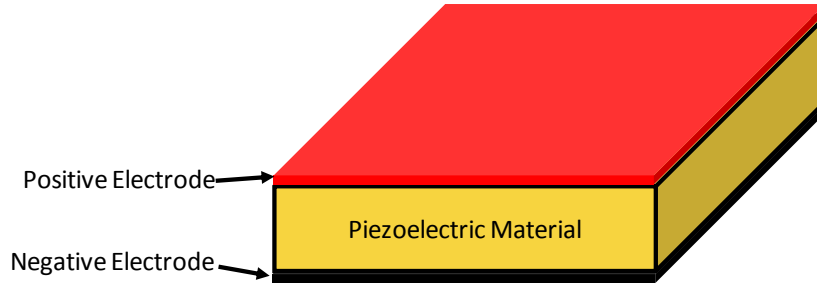


Figure 13: Monolithic Piezoelectric actuator

In certain applications, the overall displacement generated by a monolithic piezoelectric actuator can be increased by utilizing the d_{31} mode rather than in the d_{33} mode of operation, even though the d_{33} mode produces a larger displacement responses for a given electric field (Hagood, Kindel and Ghandi). This is due to the fact that with only simple electrodes, the d_{31} mode is more easily used on large actuators. By operating in this mode, the resultant strain generated by applying an electric field is smaller but can be when applied over larger lengths than the d_{33} mode, the d_{31} mode actuator can generate larger displacements.

Beam Actuators: The d_{31} mode monolithic actuator can be integrated into composite laminated beam configuration to produce either an extensional or bending beam actuator. The extensional type actuator, as shown in Figure 14, uses two pieces of piezoelectric material laminated to the opposing sides of an elastic substrate. The poling direction of the piezoelectric materials, as well as the direction of the applied electric field, are oriented to result in a uniform extensional deformation along the length of the actuator. This is done by actuating both piezoelectric components such that they produce an extensional deformation.

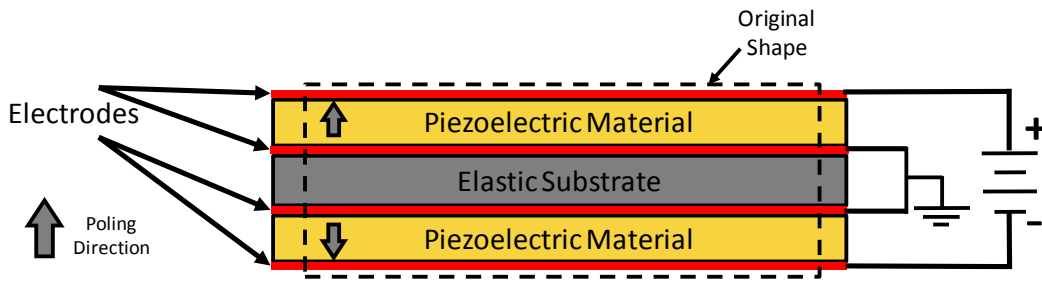


Figure 14: An extensional actuator consisting of two piezoelectric sections of material sandwiching an elastic substrate shown in the deformed shape

The design of the extensional laminated composite beam actuator can be slightly changed to produce a bending actuator. This can be accomplished by changing the poling direction of one of the piezoelectric components, as shown in Figure 15. When actuated, one piezoelectric component produces an extensional strain response, and the other piezoelectric component produces a contracting strain response, resulting in a bending deformation of the entire structure. The resultant bending of the actuator can be very useful as it creates significant displacements at the tip of the beam and can be integrated into many applications.

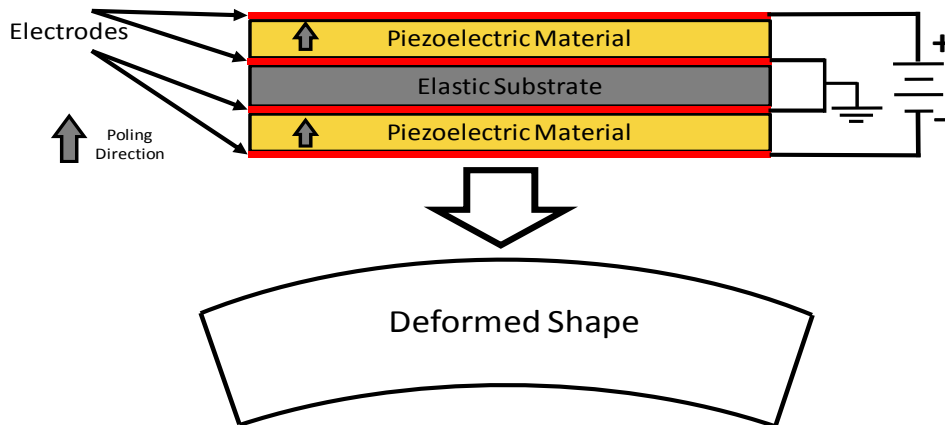


Figure 15: Bending actuator design showing the poling direction of the two piezoelectric components

used rather than the d_{31} term, producing a larger strain response for a given electric field (Hagood, Kindel and Ghandi).

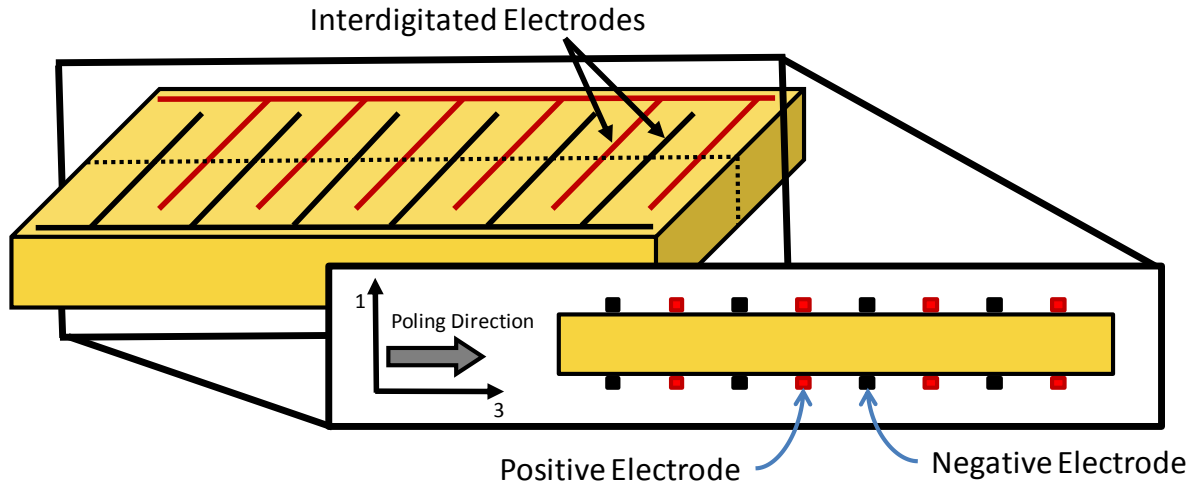


Figure 17: Illustration of interdigitated electrodes applied to a monolithic piezoelectric material

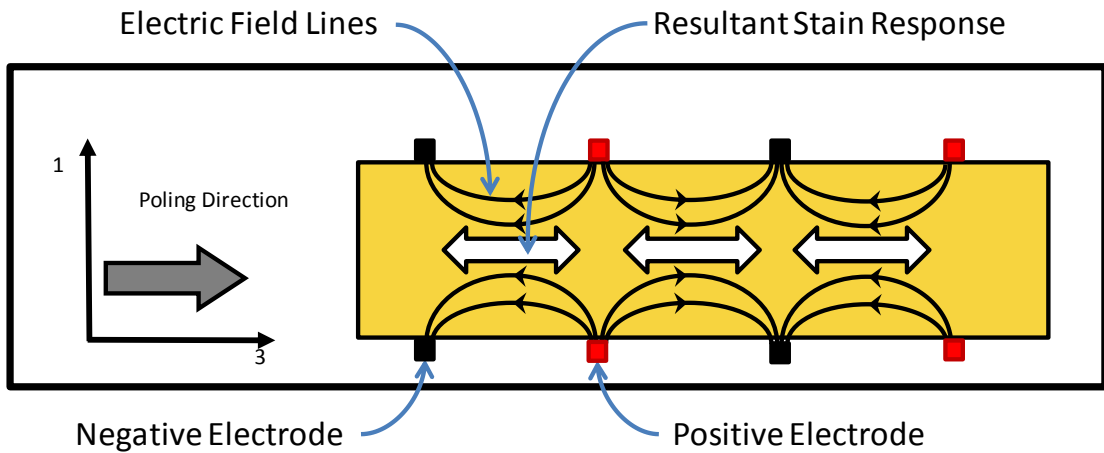


Figure 18: The electric field lines formed from interdigitated electrodes on a piezoelectric material

Piezoelectric Fiber Composite Overview

Monolithic piezoelectric systems have proved to be of significant usefulness as actuators, sensors and similar device, however, several shortfalls associated with their use do exist. The most significant of these shortfalls being brittleness, low strain energy density, and a poor ability to be conformed to non-planer surfaces (Wilkie, High and Bockman). To expand upon the usefulness of monolithic piezoelectric systems and to overcome certain obstacles associated with their use, piezoelectric materials have also been integrated as fibers into composite laminate systems.

Several versions of piezoelectric fiber composites exist today, however, there are two leading types of that are specify designed from structural applications. These types are Active Fiber Composites or AFC's and Macro Fiber composites or MFC's (Williams, Guyhae and Inman). AFC were originally developed at the Massachusetts Institute of Technology (MIT) starting in the early 1990's (Bent and Pizzochero, Recent Advances in Active Fiber Composites for Structural Control). Macro fiber composites were originally developed at NASA Langley Research Center (Wilkie, High and Bockman).

There are several advantages to using piezoelectric fiber composites. The flexible epoxy around the fibers allows the composite to easily conform to contoured surfaces, and using ceramic fibers have a smaller volume fraction of flaws in fiber form resulting in an increase in specific strength (Williams, Guyhae and Inman). Piezoelectric fiber composites can also offer significant damage tolerance, and reliability when compared to monolithic piezoelectric actuators (Sodano, Park and Inman).

Interdigitated electrodes, as shown in Figure 17 and Figure 18, were also integrated into piezoelectric fiber composites as a means of increasing the maximum achievable strain possible from the composite. This advancement continued the development of piezoelectric fiber composite to improve the potential of these composite systems (Bent and Hagood, Improved performance in Piezoelectric Fiber Composites using interdigitated electrodes).

To utilize the advantages of piezoelectric fiber composites, the early generations of piezoelectric fiber composites combined interdigitated electrodes with cylindrical fibers as shown in Figure 19 (Wilkie, High and Bockman). The AFC developed by MIT typically utilizes extruded cylindrical fibers imbedded in a polymer matrix, and can be combined with much smaller fiberglass fibers to increase strength (Williams, Guyhae and Inman). AFC's can also be made from molded fibers, or rectangular fibers diced from a piezoelectric wafer (Williams, Guyhae and Inman).

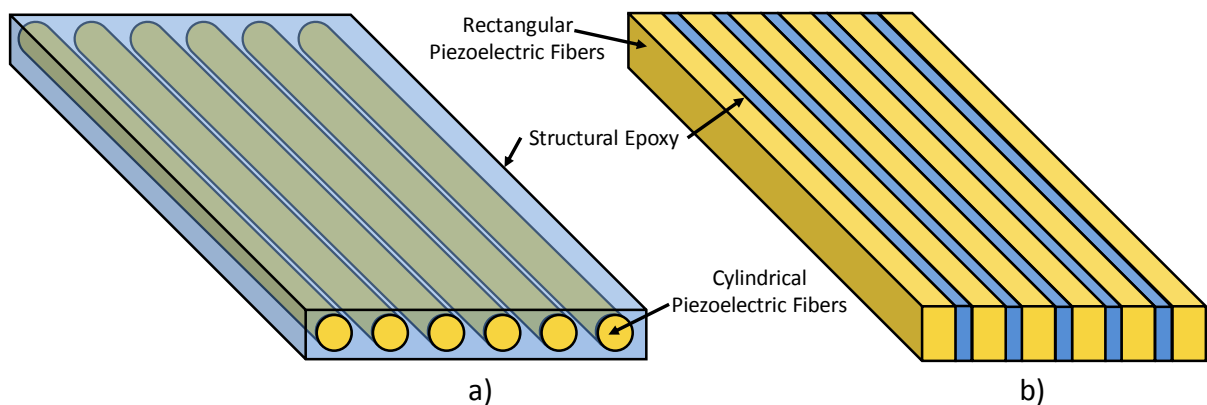


Figure 19: Piezoelectric fiber composite with both a) cylindrical fibers, and b) rectangular fibers

The NASA Langley Research Center also developed the piezoelectric fiber composite called the macro fiber composite or MFC. MFC's are now mass produced by Smart Materials of Sarasota Florida. MFC's come from the manufacturer ready to be used once laminated to a structure and the proper electrical connections have been made. The Piezoelectric fibers in MFC's are packaged between two layers of polyimide film making a patch that can be easily integrated into both mechanical and electrical systems as shown in Figure 20.

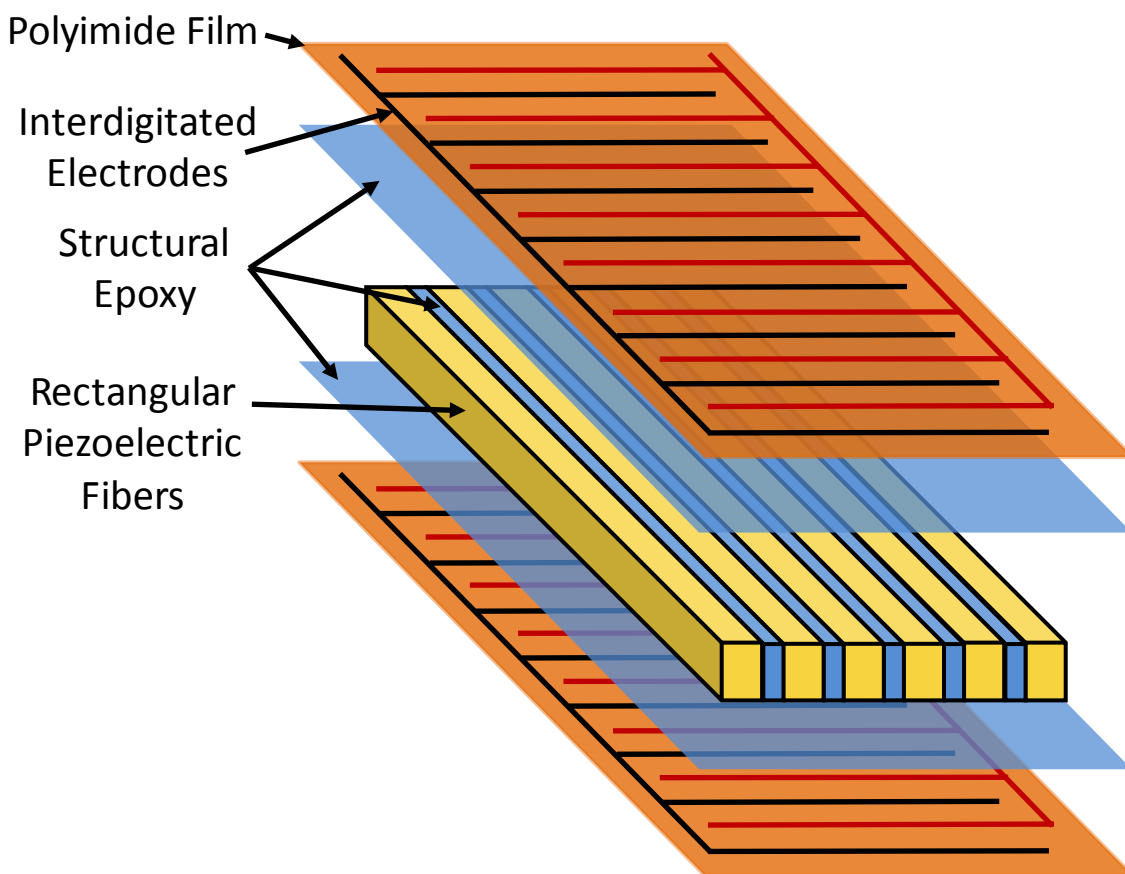


Figure 20: Expanded view of a MFC patch showing the interdigitated electrodes on polyimide film, the structural epoxy, and the rectangular piezoelectric fibers separated by structural epoxy

Macro Fiber Composite Overview

MFC's have proven to be useful in a variety of applications including structural actuation, energy harvesting, vibration control, health monitoring, and sensor applications (Scalea, Matt and Bartoli)(Kunzmann and Daue)(Matt and Scalea)(Schultz and Hyer)(Ruggiero, Park and Inman). Work associated with integrating MFC's into such a variety of applications has resulted in a large body of knowledge regarding MFC's and their characterization.

MFC's take advantage of the advances in piezoelectric fiber composites and use interdigitated electrodes. The electrodes in the MFC are made by photo restive etching a polyimide and copper laminate material (Wilkie, Bryant and High). MFC uses the PZT 5A1 piezoelectric material for piezoelectric fiber material (Smart Material Corporation). The fibers are rectangular and are produced by dicing the fibers from a low cost piezoelectric wafer (Williams, Guyhae and Inman). The special dicing and assembly process allows the MFC reduces the production cost of MFC's while continuing to be a precise and repeatable process (Wilkie, Bryant and High).

A thermosetting polymer epoxy system, specifically Loctite DURABOND E-120H, is used to bond not only the fibers to each other, but also to attach both layers of electrodes and polyimide to the fibers (Williams, Grimsley and Inman). The components that make up the MFC are shown in Figure 21. The figure shows the fiber and electrode orientation which utilize interdigitated electrodes to produce a potion of the electric field in the fiber direction (Hagood, Kindel and Ghandi).

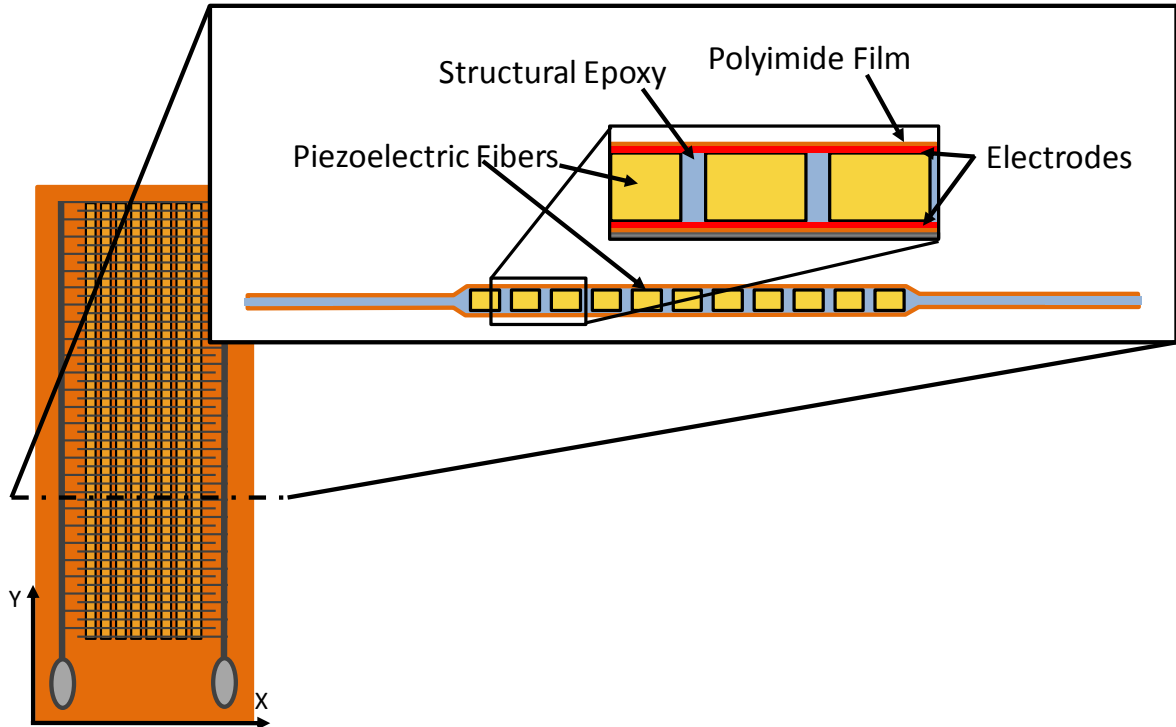


Figure 21: An illustration showing the composition of the MFC's

Current MFC Charaterization

Literature presents a fairly substantial quantity of information about MFC's allowing them to be integrated into many actuator applications. The general material properties, such as material stiffness, Poisson's ratio, piezoelectric strain coefficient, blocked force, and free strain are given by the manufacturer as known information (Smart Material Corporation).

The manufacturer's information is presented in Table 2.

Table 2: P1 Macro Fiber Composite Material Properties (Smart Material Corporation)

High Field (Greater than 1kv/mm)		
d_{33}	460 pC/N	460 pm/V
Low Field (Less than 1kv/mm)		
d_{33}	400 pC/N	400 pm/V
Free Strain per Volt	0.75-0.9ppm/V	0.75-0.9ppm/V
DC Poling Voltage	1500V	1500V
Poled Capacitance	0.42 nF/cm ²	207 nF/in ²
Constant Electric Field Elastic Properties		
Tensile Modulus (fiber direction)	30.336 GPa	4400 Ksi
Tensile Modulus (electrode direction)	15.857 GPa	2300 Ksi
Poissons Ratio (V12)	0.31	0.31
Poissons Ratio (V21)	0.16	0.16
Material Limitations		
Operational Voltage Range	-500 V to +1500 V	-500 V to +1500 V
Strain Limit (linear elastic)	1000 ppm	1000 ppm
Max Tensile Strain (operational)	< 4500 ppm	< 4500 ppm
Work-Energy Density (peak)	~1000in-lb/in ³	~1000in-lb/in ³
Max Temperature (operational)	< 80°C	< 176°F
Lifetime @ 1kVp-p (operatitonal)	>10 Billion Cycles	>10 Billion Cycles
Lifetime @ 2kVp-p, 500V DC (operatitonal)	> 100 Million Cycles	> 100 Million Cycles

The data presented by the manufacture does not address variability of the material propertied of the composite constituents. For example the composite constituents have significantly different coefficients of thermal expansion, which could lead to internal stresses within the composite when the temperature of the MFC is changed from the temperature that it was manufactured at (Williams, Inman and Wilkie, Temperature-Dependent Coefficients of Thermal Expansion for Macro Fiber Composite Actuators). This could be of significant concern with respect to the reliability of the material, specifically when operated at elevated or lowered temperatures.

Research has been performed regarding the reliability of MFC at different temperatures however, the experiments were limited to only a few temperatures and no information is available for temperatures below 22 degrees Celsius or for temperatures above 75 degrees Celsius. The results of these experiments were in agreement and showed the MFC not only displayed long fatigue cycle life, but also displayed a minimal degradation in performance over the temperature range from 22 degree Celsius to 75 degrees Celsius under various loading conditions(Nuffer, Schönecker and Kohlrautz) (Wilkie, High and Bockman).

Past reliability studies have used the converse piezoelectric effect to test the MFC's useable life as an actuator. Meaning that for the different loading conditions, a voltage potential was applied across the electrodes on the MFC inducing a mechanical response within the MFC. This testing was performed for specimens under no load, and, for specimens that were constrained by a laminated beam structure. The specimens tested under no load closely simulate the free strain condition for monolithic piezoelectric material. The only difference is that the fibers are slightly constrained by the composite constituents which would contribute to a small stress resulting in the fibers from the electrical excitation.

For the specimens that were incorporated into laminated beam structures, two main loading regimes were investigated. One test laminated a d_{33} MFC inside a fiberglass testing coupon with E-glass cloth being placed on each side of the MFC. The coupon was loaded using a hydraulic testing system to a displacement of 1,000 micro strains. The MFC was then actuated by applying 1000kVp-p at 100 Hz to the MFC electrodes, causing the MFC to extend during each voltage application. The exact waveform is not specified, however, the applied voltage was the maximum voltage that could be applied to this version of a MFC.

The testing was performed at 30 degrees Celsius and 65 degrees Celsius. No higher temperature was tested due to a reduction in of the mechanical strength of the epoxy used in this version of a MFC. Specimens were tested for 10 million cycles with minimal degradation in performance (Wilkie, High and Bockman).

The second type of beam laminate using a cantilevered beam design was also characterized with respect to actuation life. The laminate consisted of an inactive substrate with a contracting d_{31} MFC laminated to one surface. When voltage was applied to the MFC, the MFC would contract resulting in the beam bending. To test the laminated beams voltage was applied at 125 Hz, exciting the second resonant mode for the laminated beam. The exact waveform of the applied voltage and the amplitude of the applied voltage is not specified. Specimens were cycled at 22 degrees Celsius and 75 degrees Celsius for 500 million cycles with negligible degradation (Nuffer, Schönecker and Kohlrautz).

The current reliability testing has defined a region of reliable use for MFC's. This region is specific to the testing parameters used, and leaves certain aspects of the design space unexplored. Specifically, information is not available that identifies the usable temperature limits of the MFC or how operation temperature effects the performance, and the usable life of MFC. For many applications this is critical information, especially when reliability is a critical design parameter.

EXPERIMENTAL PROCEDURE

Experiment Design

Reliability is one of the most important parameters for any actuator design that is to be sent into space, where maintenance is simply not available. For MFC's to be characterized sufficiently for use as a valve actuator for the lunar environment the relationship between useable life and operating temperature must be understood, specifically as the operating temperature must be maintained for applications such as in the permanently shadowed craters in the Aitken Basin on the moons south pole. The current research has been conducted to fill this gap in knowledge, so as to provide information that could allow MFC's to be used as a valve actuator on future lunar exploration mission.

Specifically the current research was focused on determining the operational performance of MFC's over a temperature range from 0 degrees Celsius to 100 degrees Celsius. Efforts were also focused on determining the usable life of MFC's over this temperature range. To accomplish this goal, specimens were tested either to failure, or to 250 million cycles, from -15 degrees Celsius up to 145 degrees Celsius.

The loading condition or mechanical configuration of the specimen specimen was designed to closely relate to possible valve actuator designs, as this is the end goal of this effort. As all actuator designs utilized a bending beam actuation technique, the experimental test also would test the MFC in bending. From among the various options for testing a MFC in bending, a cantilevered beam setup emerged as the most practical test. The cantilevered beam was laminated on one side with a MFC, when voltage was applied to the MFC it would

extend along the length of the beam, causing the MFC and the beam to bend as shown in

Figure 22.

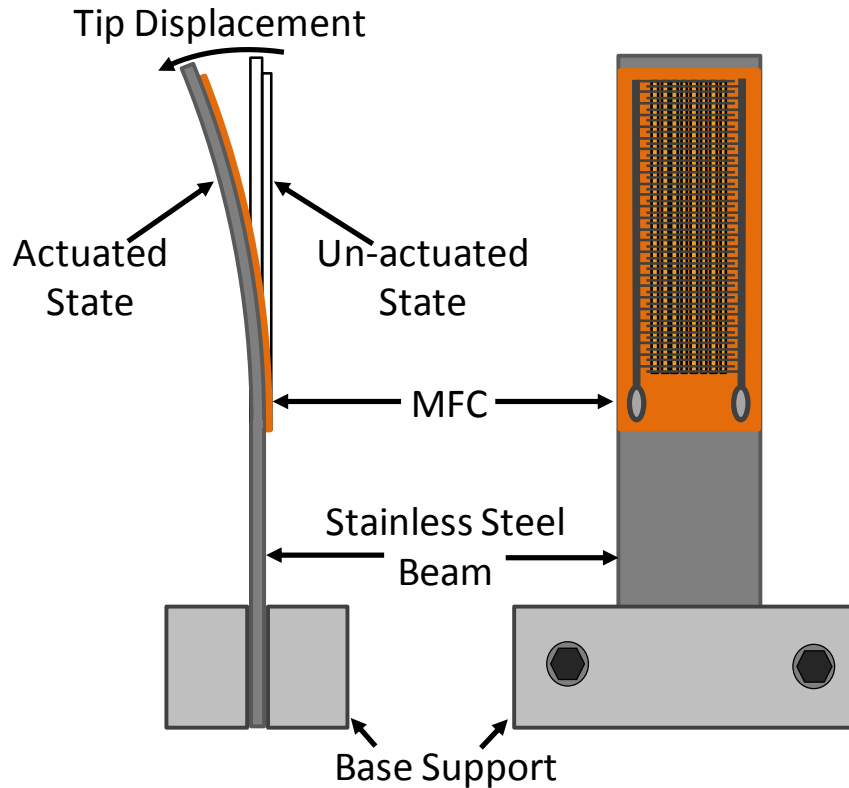


Figure 22: Cantilevered beam experimental design showing the MFC laminated on one side of a stainless steel beam and the entire structure being supported at the base of the beam

This experimental design also allowed for comparisons to be drawn between the current and past experiments, for validation. The experimental design was similar to one performed in the past for a beam in bending, however, many key differences did exist. The most significant is the MFC that was tested in the past operated using the d_{31} effect, and the current experiments used the d_{33} effect. The d_{33} effect MFC's were used as it has a larger piezoelectric strain coefficient as well as higher maximum operational voltage, and could therefore generate larger deformations and would be more practical for use as an actuator.

The past experiments also applied a cyclical voltage at a frequency that excited the second resonant mode for the laminate, as described by Figure 23. This generates a compression and tension zone along each side of the laminate, creating a dynamic loading condition. An actuator, specifically for use in a valve would not display this loading condition. Therefore to more closely represent a real world actuator, the current experiment used cyclical voltage was applied at the first resonant frequency, as in Figure 23.

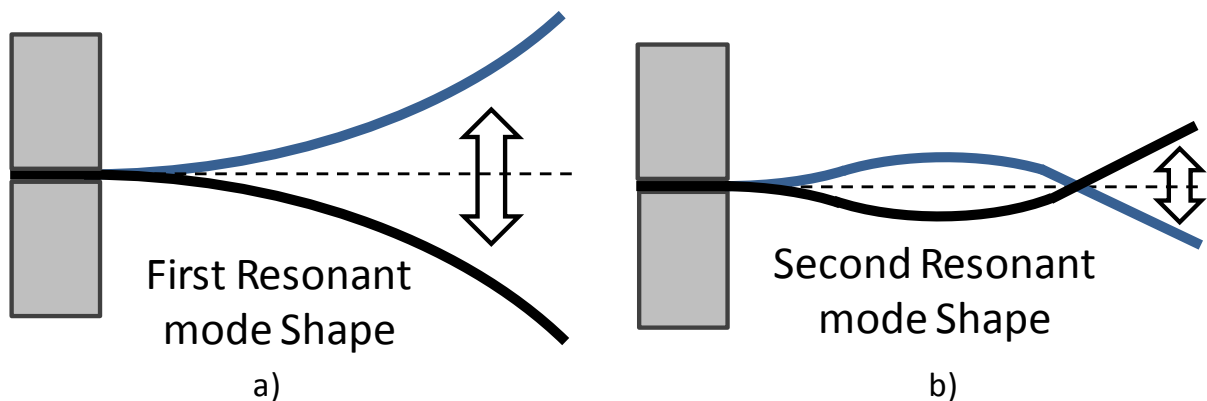


Figure 23: Drawing of the first and second resonant mode shapes for a cantilevered beam

Experimental Specimen

The specific dimensions of the test specimens, as shown in Figure 24, were designed to provide the required information on MFC's. The MFC used was an M-2807-P1 manufactured by Smart Materials. This MFC has an overall length of 40mm, an overall width of 18mm and a thickness of 0.3mm (Smart Material Corporation)(Smart Material). The MFC contains Lead Zirconium Titanate (PZT) fibers that make the active area within the MFC. This active area is 28mm long in the fiber direction and 7mm wide transverse to the fiber direction (Smart Material). The fibers are 0.18 mm thick and made of PZT 5A1(Smart Material Corporation). The MFC's have interdigitated electrodes, which are used for poling

the piezoelectric material and results in the poling direction coincident to the fiber direction (Williams, Guyhae and Inman). The MFC operates in the d_{33} mode and therefore produces an extensional strain response when an electric field is applied. The stainless steel beam was three inches long and 0.715 inches wide. The beam had tapered edges, as shown in Figure 25, to alleviate any stress concentrations at the edge of the laminate. This was done to minimize any tendency for delamination at the edges of the beam, as the focus of the study was to investigate to usable life of the MFC rather than to investigate MFC's tolerance of stress concentrations at the edges of the laminate. An Omega Precision strain gauge model SGD-7/350-LY11, was attached to the beam on the opposite side of the MFC as shown in Figure 24. As seen in Figure 24 the strain gauge was located lower than the MFC as to not overlap the MFC, keeping the beam cross section consistent under the MFC.

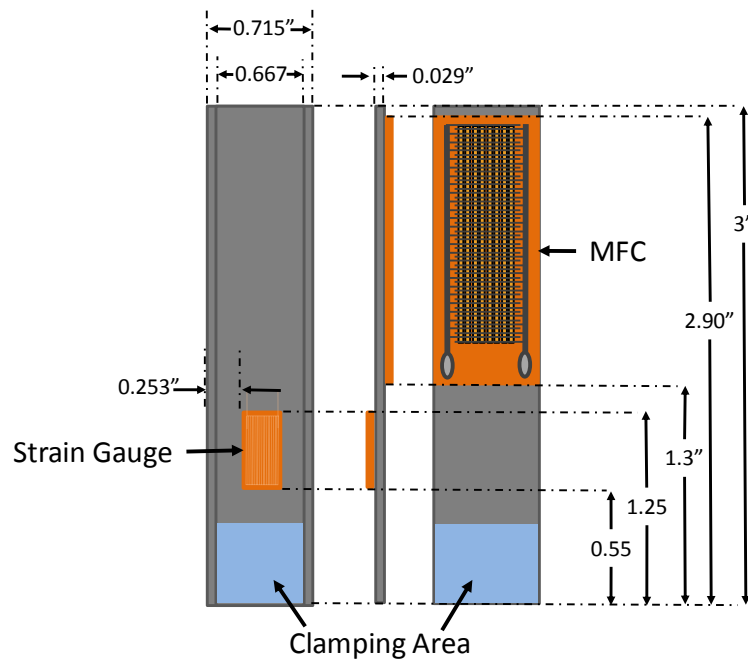


Figure 24: Specimen design and dimensions showing location of the MFC, strain gauge and clamping area

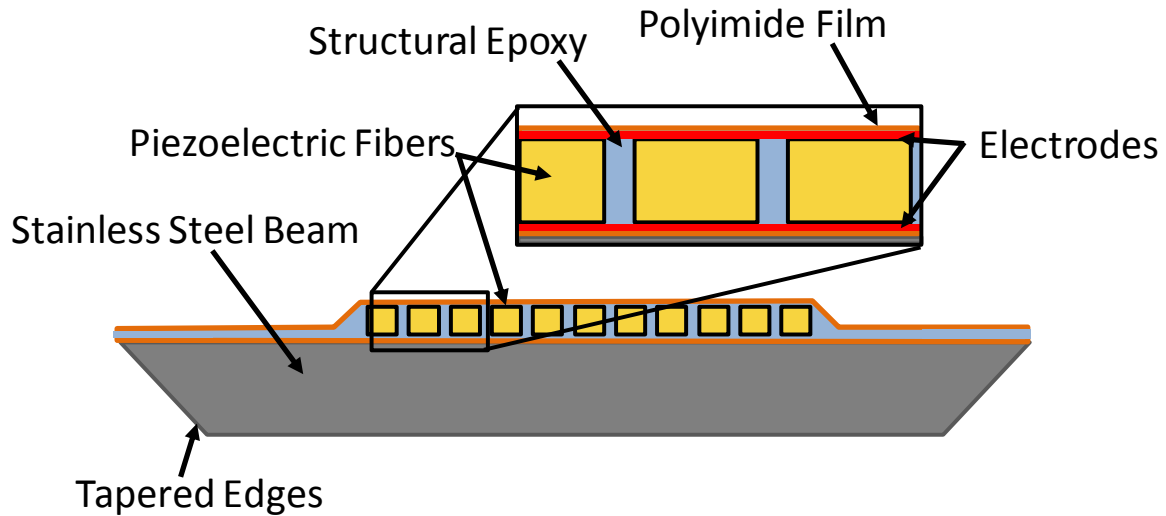


Figure 25: Cross section of the beam laminate showing the tapered edges of the beam

A repeatable beam lamination procedure was used for consistency between specimens. Two specimens were laminated at a time, for simplicity the procedure is only described once, but performed twice, once for one specimen, and once for the other specimen. The procedure began by preparing the stainless steel beam by cutting the stainless steel stock to length. The stainless steel stock was previously cut to the desired width, with the edges tapered, so no further preparation of the edges was required. Next the beam was sanded using 100 grit emery cloth to provide a rough area to promote bonding between the MFC and the beam. The beam was then wiped with the solvent Xylol to clean the beam and remove any oils from the surface of the beam.

A thin sheet of smooth protective plastic, such as a blank overhead sheet, was attached with tape to a lab table to protect the table from the epoxy used to laminate the beam. A secondary sheet of the thin plastic sheet was then attached with tape on top of the first sheet to form a hinge. This allowed the top sheet to be folded back to reveal the first and

bottom sheet of plastic. The bottom sheet was used as a base on which the laminate would be constructed. Once the lamination process was complete, the top sheet could then be folded back over the laminated beam. The sheets aided in the lamination process in several ways. First, by containing the laminated structure within two sheets of plastic that were mechanically attached to each other limited any forces on the laminated structure to be normal to the two sheets of plastic. As only a small amount of uncured epoxy connects the top sheet to the beam structure very small tensile loads could be applied to the plastic sheets before the top sheet simply lifts off the beam structure. This effectively limits the force that can be applied on the beam structure to be pure compression, ensuring the alignment of the components of the laminated structure. The plastic sheets also were very smooth and bonded poorly to the epoxy, making them easy to remove from the specimen once the epoxy had cured.

To begin the lamination process, the beam was attached to the bottom plastic sheet with Kapton tape. The tape was only placed on the one edge of the beam to form a hinge that would allow the beam to be folded over for access to both sides while restraining the motion of the beam. The tape was positioned in a location other than that of the MFC or strain gauge.

The beam was then turned over to reveal the Strain gauge side. Calipers were then used to measure the proper location of the strain gauge on the beam, which were then marked. The strain gauge was carefully removed from the packaging so that the bottom side of the strain gauge was not touched. The strain gauge was then placed on the beam. The strain gauge was aligned with the measurement marks and rotated so that the wire leads

would face the top or the unclamped end of the beam. The strain gauge was then held in place with Kapton tape. The tape was only placed on the end of the strain gauge opposite the leads so that it could be hinged to preserve alignment when the epoxy was later added. The tape covered the entire back section of the strain gauge to prevent any epoxy build up from occurring. A single layer of 0.375 inch wide, 0.002 inch thick Kapton tape was then applied to the beam as an electrically insulating layer under the wire leads of the strain gauge. The tape was also applied on much of the face of the beam as a mask to minimize the amount of epoxy on the beam that would flow out from under the MFC and strain gauge when it was later pressed.

The beam was then turned back over to the side where the MFC was to be attached. Calipers were then used to measure the proper location of the MFC on the beam, which was then marked. The MFC was then carefully removed from the packaging so as to not touch the bottom side of the MFC. The MFC was then placed on the beam. The MFC was aligned with the measurement mark, and held in place with Kapton tape. The tape was only placed on one end of the MFC so that it could be hinged when the epoxy was later added. This preserved alignment of the MFC on the beam when it was lifted up to apply the epoxy. Kapton tape was applied to the top surface of the MFC as a protective layer to prevent epoxy from building up on the MFC. The tape was also applied on much of the face of the beam as a mask to minimize the amount of epoxy on the beam that would flow out from under the MFC and strain gauge when it was later pressed.

A 3M Scotch Weld Epoxy Adhesive Dp 460 two part thermosetting epoxy system was used to bond both the MFC and the strain gauge to the beam. This epoxy system

exhibited properties desirable for the designed testing. The epoxy system had also been used in past testing of MFC's without notable difficulty. The system was therefore adopted for the current testing efforts.

Before applying the epoxy system the beam was hinged over to reveal the strain gauge. The strain gauge was gently lifted by the backing Kapton tape and a thin layer of premixed epoxy was spread on the beam surface to ensure a smooth even coating with a paperboard applicator. The strain gauge was placed back on the beam. Starting at the Kapton hinge, the strain gauge was seated in the epoxy with a gently rubbing motion, starting at and moving away from the hinge. This helped to remove air bubbles trapped in the epoxy as well as push excess epoxy out from under the strain gauge.

The beam was then hinged back over to the MFC side of the specimen, taking care to not disturb the strain gauge. The MFC was then gently lifted by the backing Kapton tape, with care being taken to not touch the bottom side of the MFC. Next premixed epoxy was applied to the beam using a paperboard applicator. The epoxy was applied in a thin and smooth layer. The MFC was then gently placed on the epoxy. In a manner similar to that used on the strain gauge, the MFC was set into the epoxy with a gentle rubbing motion moving from the hinged end of the MFC to the opposite end.

The top sheet of plastic was then carefully folded back over entire beam structure, and a thin sheet of closed cell foam was placed over the top sheet plastic. The foam conforms to the irregular shape of the MFC while still maintaining a compressive force on the laminate. Next a square aluminum beam is placed over the foam to distribute the

compressive loads from the clamps used to compress the laminate. The 6061 aluminum beam was 0.75" wide, 0.7" high and 10" long.

Three clamps were used to establish an even compressive force on the beam structure while the epoxy cured. First a clamp is placed in the center of the beam, and tightened enough to hold the beam, foam, plastic and beam structure securely. Next two identical Pony 246 large C-clamps are placed on the beam at equal distances from the center clamp just slightly farther out than the laminated beams. The two side clamps were then simultaneously tightened until further tightening began to deform the clamps rather than compress the foam. The center clamp was then tightened to approximate the same pressure as the two side clamps.

The epoxy was allowed to cure per the manufacture's data sheet recommendations at room temperature. The center clamp was loosened and also set aside. The two side clamps were then loosened and set aside. The aluminum beam and the foam were then removed from the top of the plastic sheet, and set aside. As the epoxy had cured, plastic sheets were bonded to the beam structure, however, the smooth plastic sheets were easily removed from the beam without damaging the beam laminate. Extra care was taken, while removing the plastic sheets from the beam, to not exert any significant forces on the beam structure. Care was taken to limit the forces on the beam to those in plane with the stainless steel beam. The beam laminate was then ready to be cleaned of excess epoxy residue as shown in Figure 26.

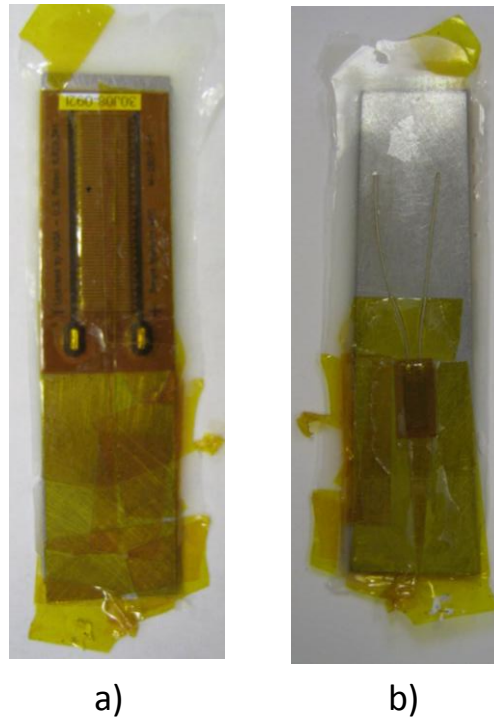


Figure 26: A specimen after the plastic sheets have been peeled off showing a) the MFC side of the beam and b) the strain gauge side of the beam

The next step in the process of preparing a specimen was to remove the remaining Kapton tape. In a similar process to that used to remove the plastic sheets, special care was used to keep the force exerted on the beam small and in the plane of the beam. Next the remaining epoxy that flowed from under the MFC and the strain gauge was carefully removed with a razor. To accomplish this, the beam was held vertically on a table, and the razor was gently slid down the outer edges of the beam. The epoxy on the top of the beam was also removed in a similar manner with the beam on its side. The cleaned beam is shown in Figure 27.

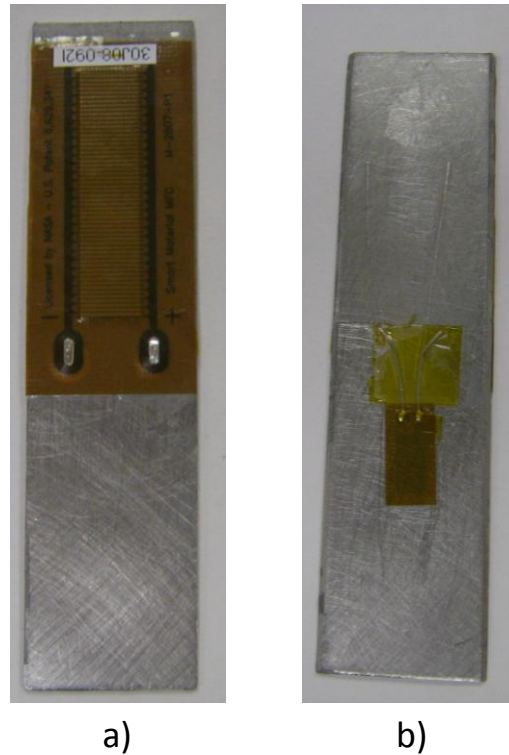


Figure 27: Experimental specimen after the Kapton tape and excess epoxy has been removed showing a) the MFC side of the specimen and b) the Strain gauge side after the wire leads have been trimmed

The wire leads on the strain gauge were then trimmed with a razor blade to not hang off the edge of the Kapton tape used as an electrical insulator under the leads. Using a gentle sawing motion, the leads were trimmed. Figure 27 shows the trimmed strain gauge leads.

Wire leads made of 29 gauge wire, approximately 2.5 in long, were soldered to the specimen. Solid copper wire ends were then attached to the wire lead as the copper were more easily mounted into the testing apparatus. The laminated beam could be mounted in the test fixture and at this point could be tested. However, a special strain measurement tool was to be used that required the specimen to be painted with a high contrast speckle pattern.

The GOM Aramis 5m optical deformation analysis system was used to measure three dimensional displacement and strain information at various cycle numbers while the specimens were cycled at different temperatures. The system requires a contrasting speckle pattern to be applied to the specimen. Using two cameras, the system can track the location of each speckle as the specimen is deformed. The system then calculates and outputs both the displacement and strain data as specified by the user.

Before applying the paint to the specimen, the areas where paint was not required were masked using tape. First Kapton tape was used to mask the strain gauge and the strain gauge leads. Then masking tape, used to prevent paint from being applied to the clamping section of the beam, was applied to the base of the MFC. The MFC wire leads were also masked, however, some paint was applied to the wires as they were attached to the MFC near the location that displacement and strain data was to be collected.

To apply the speckle pattern, specimens were first painted flat white, using spray paint. Several thin coats of paint were applied, until you could not see through the white paint. A small bristle brush, was then used to apply a flat black paint to the specimen to form the contrasting speckle pattern. To apply the black paint, first flat black spray paint was sprayed into a small container, such that it formed a small pool of paint. Next the small bristle brush was dipped into the paint. The brush was then quickly rubbed across a small metal cylinder. The cylinder was approximately 1/8th of an inch in diameter and 4 inches long. This action caused the paint to be thrown off the bristles of the brush forming a consistent speckle pattern on the surface. Particular attention was needed to achieve a consistent speckle pattern. To maintain a consistent speckle pattern between specimens, a

blank surface used to monitor speckle size after fresh paint was applied to the brush before the specimen was speckled. A guide to optimized speckle size that came with the Aramis system was initially used to judge speckle size. The masking tape was then removed from the specimen and the specimen mounted into the testing apparatus

Electrical Circuit Design

An electrical circuit had to be designed and built that could not only provide the high voltage excitation to the MFC but also allow the voltage to be cycled on and off at the desired testing frequencies of between 0 and 120Hz. EMCO High Voltage Corporation, high voltage power supply modules were used to convert an input of 12 volts to 1000 volts. An insulated gate bipolar transistor was used as a switch to connect or disconnect the MFC from ground. The electrical circuit, shown in Figure 28, shows the designed circuit. The MFC is modeled electrically as a capacitor.

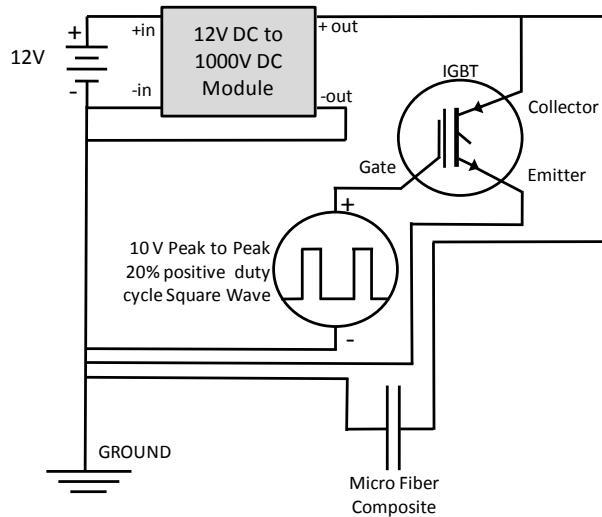


Figure 28: The electrical drive circuit used to actuate the macro fiber composite which is electrically modeled as a capacitor

Each component of the circuit was not actually located on the breadboard used to connect the components of the circuit. The 12 volt DC power supply as well as the arbitrary waveform generator were off the shelf lab equipment and as such were located next to the breadboard. The MFC was also not located on the breadboard, as it was located on the test specimen in the testing apparatus. Figure 29 shows the location of each component of the electrical diagram.

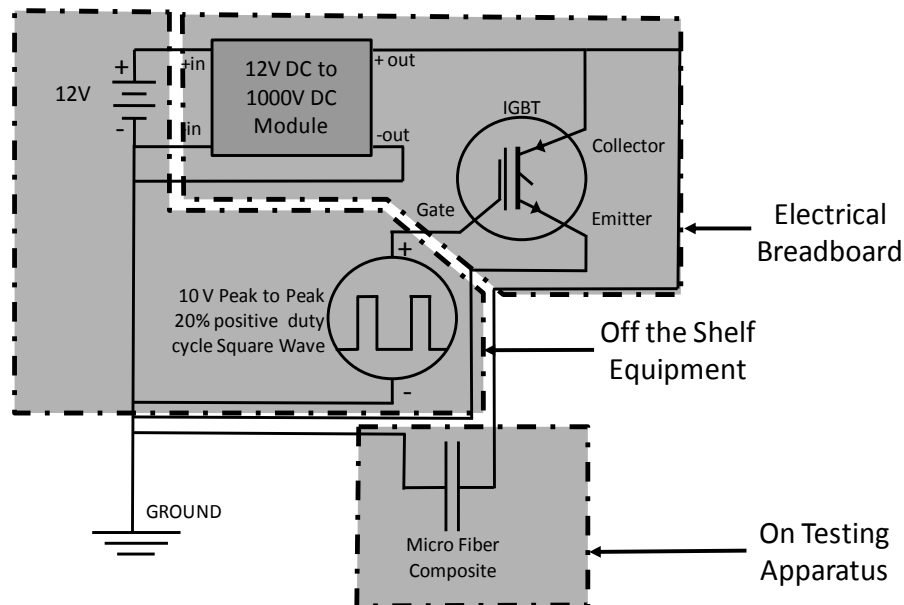


Figure 29: The location of each component of the electrical circuit

As two testing apparatus's were built to facilitate simultaneous testing of multiple specimens, two electrical circuits were also built. The two circuits built were electrically identical, however, due to equipment availability had different power output of the high voltage power supply modules. To generate the required power to the circuit, three small low-power high voltage units were used in parallel. The other circuit used only one larger unit with a higher power output. Each circuit can be seen in Figure 30

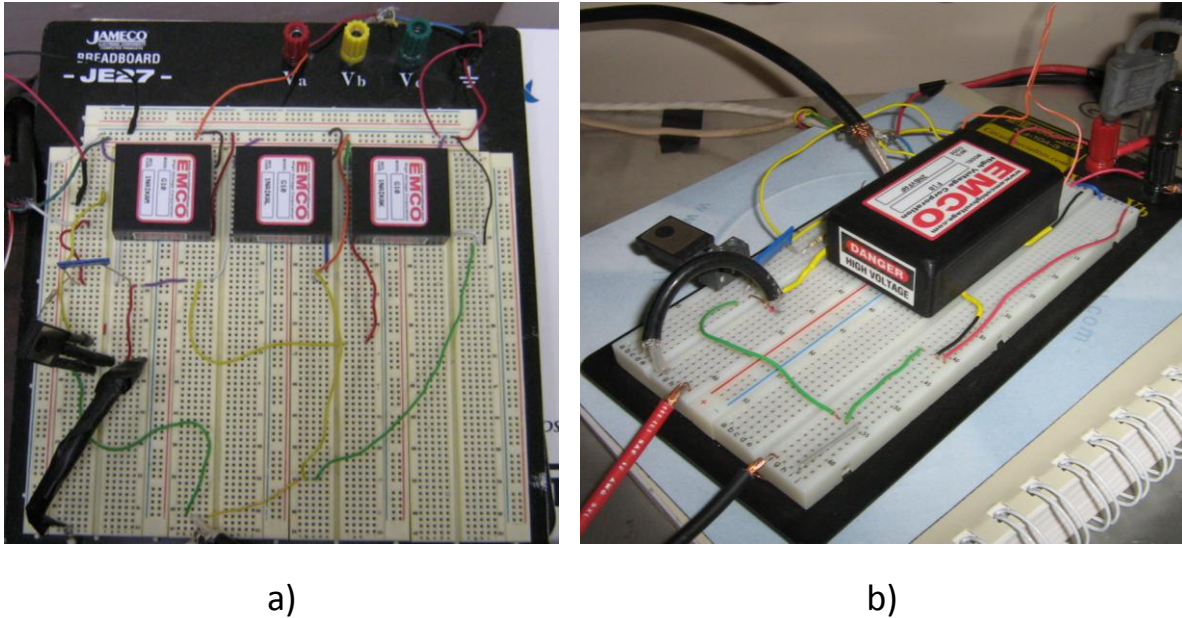


Figure 30: The electrical breadboard from both experimental testing apparatus's showing a) the three low power high voltage modules, and b) the single large higher power high voltage module

Strain Gauge

A strain gauge was laminated onto the beam specimen to monitor the vibratory motion of the beam as the MFC was cycled. The gauge was used to indicate when the MFC had begun to deteriorate or had failed. An Omega Precision strain gauge model SGD-7/350-LY11 strain gauge was used. The strain gauge was incorporated into a quarter Wheatstone bridge circuit to be monitored. As the experimental design involved testing at various temperatures, a temperature compensation strain gauge was also incorporated into the Wheatstone bridge circuit. The temperature compensation strain gauge was laminated to a small section of the same steel beam used in the test specimen and was laminated in the same manner as was used for the testing specimen. The bridge circuit, shown in Figure 31, used fixed 1megaohm resistors for R1 and R2. The circuit was excited with 20 volts.

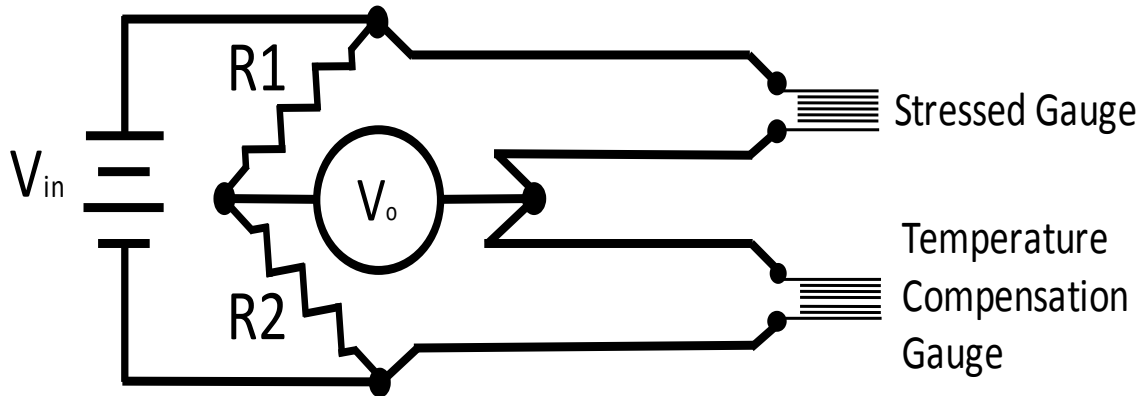


Figure 31: Wheatstone bridge circuit, showing the quarter bridge arrangement used with a temperature compensation strain gauge

Testing Apparatus

The Testing apparatus was designed to facilitate the desired experiment. As shown in Figure 32, a large aluminum mounting block was made from 6061 aluminum. The mounting block consisted of three main components, the base, the upper support and the clamping plates, as shown in Figure 32. High temperature ceramic terminal blocks were installed to provide a convenient mounting method for the high voltage wires while also providing a method for installing the test specimens electrical leads. The terminals were tested to withstand over 1200 volts. These same terminals were also used as strain relief for the strain gauge wiring. A type K thermocouple was used to monitor the apparatus temperature.

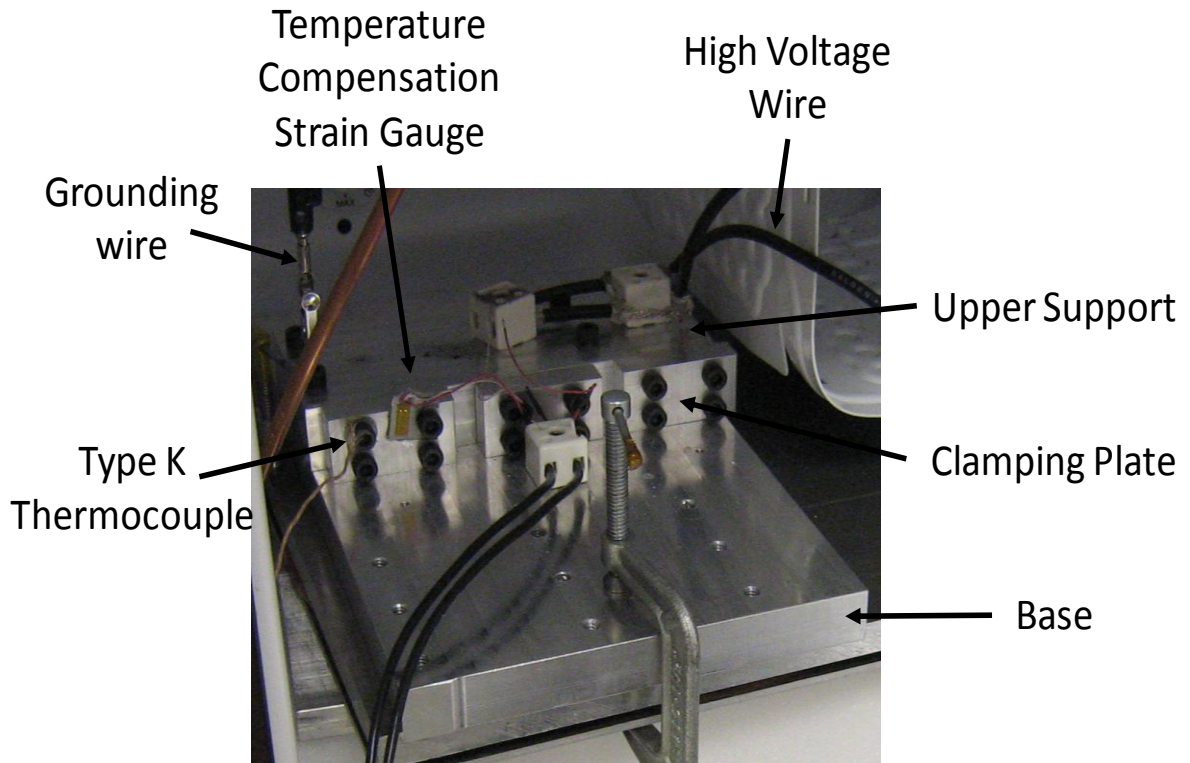


Figure 32: The Testing apparatus showing the temperature compensation strain gauge, thermocouple, grounding wire, and the other components of the apparatus

To maintain the thermal environment around the specimen, a temperature control chamber was incorporated around each of the two testing apparatus's. One apparatus was located in a Heraeus UT 6120 scientific drying oven, as shown in Figure 33. The oven could reach temperatures of up to 300 degrees Celsius, however, temperatures of only 145 degrees Celsius was actually utilized. A Teflon wire port on the top of the oven was used to pass wires to the testing apparatus inside the oven.

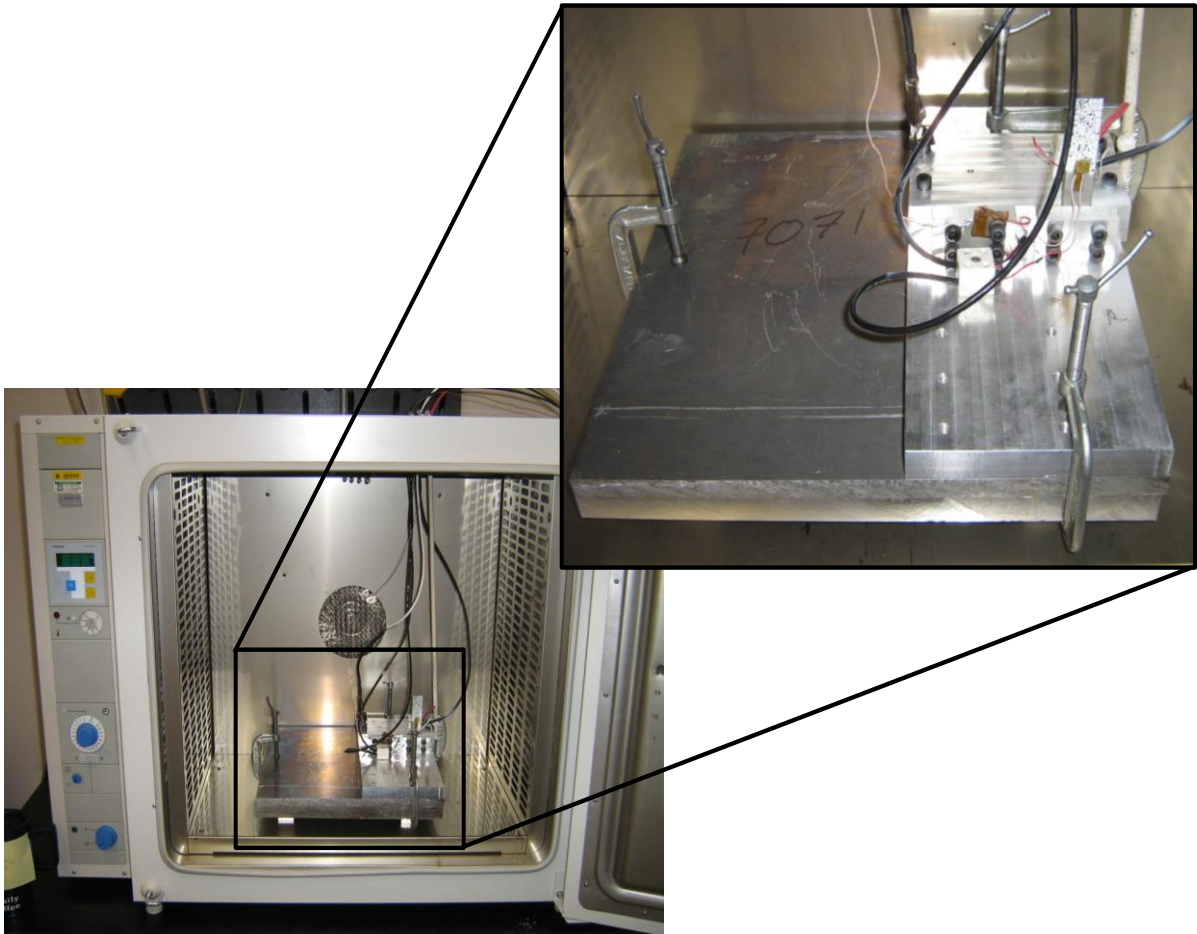


Figure 33: The testing apparatus located inside the Heraeus drying oven. The oven was used to maintain elevated specimen temperatures

The second testing apparatus was located in a small Absocold refrigerator model AR021MG15R, as shown in Figure 34. When running at steady state the refrigerator could maintain a cold temperature of -15 degrees Celsius. A type K thermocouple with an Omega cold junction compensator was used to monitor the temperature of the apparatus.

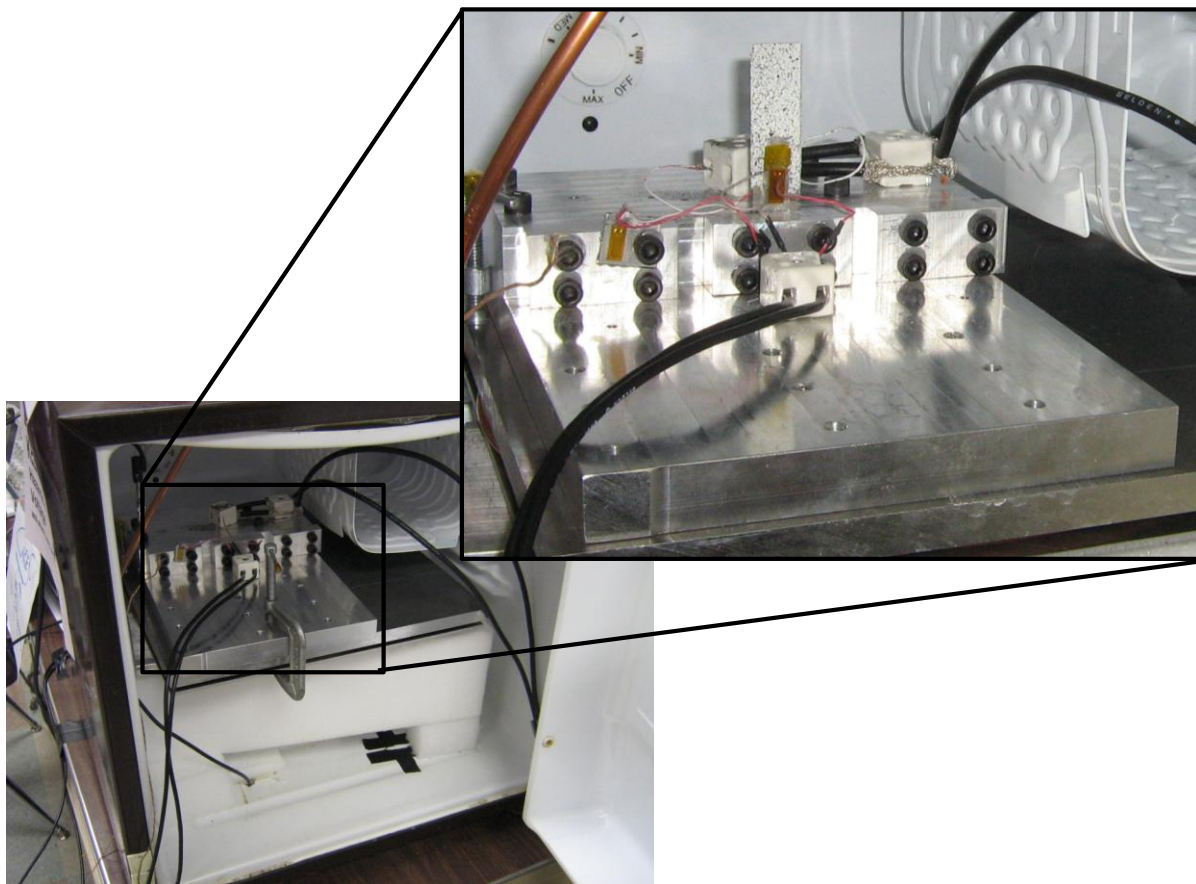


Figure 34: The testing apparatus located in the Absocold refrigerator. The refrigerator used to cool the testing apparatus

Instrumentation

A National Instruments Labview 8.5.1 program was written to collect voltage data from the Wheatstone bridge, the thermocouple, as well as the voltage being applied to the MFC. A National Instruments data acquisition system was used for both of the two experimental setups. As identical data acquisition systems were not available, two different but comparable systems were used. A National Instruments USB-6212 data acquisition system was used to collect voltage data for the experimental step in the drying oven. A

National Instruments USB-6221 data acquisition system was used to collect voltage data for the experimental step in the refrigerator.

Each data acquisition system collected analogue voltage data from multiple locations on the testing apparatus. Data was collected at 1000 specimens per second. The analog voltage data was collected from the Wheatstone bridge, the thermocouple, and the electric circuit driving the MFC.

The Labview software was used to automatically calculate the strain on the beam from the Wheatstone bridge circuit. As the beam was vibrating at its first resonant frequency, the strain signal appeared as a sinusoidal signal. A third order Butterworth bandpass filter was used to reduce the noise in the signal. The upper and lower limit of the filter were set to 0.5Hz above and below the driving frequency. The software then was programmed to calculate the peak to peak amplitude of the sinusoidal signal. To reduce file size, data was averaged at 10 second intervals. The strain amplitude was then monitored, to indicate specimen failure.

The thermocouple was calibrated by placing it in a hot water bath and an ice bath. The temperature of each bath was measured using a mercury thermometer. The thermocouple signal was filtered with a fourth order Butterworth lowpass filter to eliminate noise caused by the fluctuating electromagnetic fields in the experiment. The filter used an upper frequency limit of 12Hz. As experiments were to be performed outside of the calibration window for the thermocouple, non-calibrated data points were used to measure temperatures above and below the calibration temperatures. The calibration temperatures were as close to 0 degrees Celsius and 100 degrees Celsius as possible.

The voltage driving the MFC was measured using a voltage divider to lower the voltage to within the limits of the data acquisition systems. Two resistors in series were used to scale the voltage down by a factor of 100, so a voltage of 1000 volts was measured as 10v. As shown in Figure 35, a 100megaOhm resistor was placed between the measurement point and the high voltage supply. A 1megaOhm resistor was placed between the measurement point and ground. The high resistance of this voltage divider required only 0.01mA or .1% of the available power.

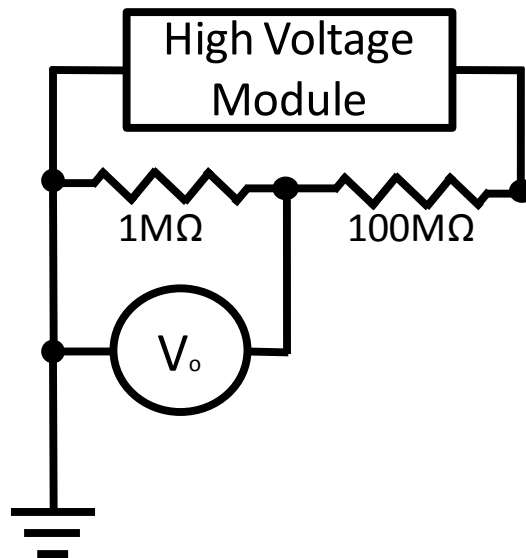


Figure 35: Voltage divider circuit used to measure the voltage applied to the MFC

Aramis Setup and Configuration

The GOM Aramis 5m optical deformation analysis system, shown in Figure 36, was used to measure three dimensional displacement and strain information at various cycle numbers while the specimens were cycled at different temperatures. The Aramis system is flexible, and can be setup to capture data from a wide range of sample types and sizes. For

the MFC test specimen, the Aramis system was setup with 17mm lenses, the two lenses were located 78mm off center with a measuring distance of 230mm. The tripod was adjusted such that the bubble levels on the tripod indicated that the tripod was level. Both LED lights on the system were used to illuminate the specimen. These lights were positioned in the same plain as the cameras and specimen, and located outside of the cameras as is Figure 36. The overhead lights were occasionally required to be turned off to minimize glare, however, this was not always required. A diagram of the system is shown in Figure 37, outlining the setup dimensions.



Figure 36: A picture of the GOM Aramis 5m system showing the setup used for taking three dimensional position, displacement, and strain data

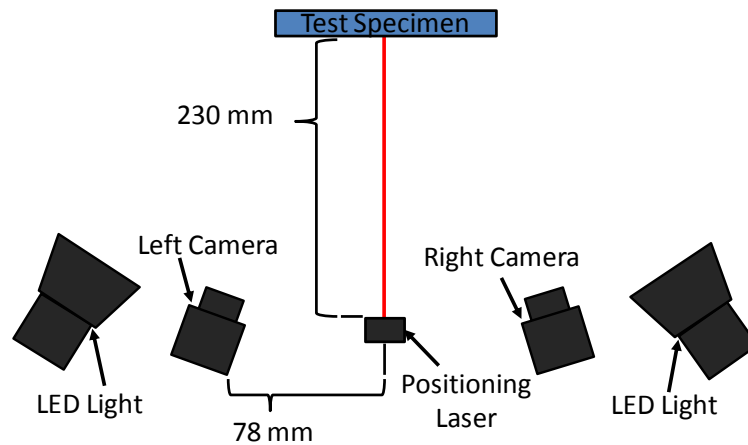


Figure 37: The Aramis system setup showing the setup distances as well as the location of the LED lights

The Aramis system software calculates displacement and strain information by correlating the position of the speckled pattern from one loading condition to another. The software allows the user to fine tune many of the parameters that are used to control these calculations. The exact parameters were chosen to provide the most accurate results rather than to minimize computation time. The chosen parameters of 30 and 15 were used for facet size and facet step respectively. For the strain calculation, a computation size of 7 was used with a validity quotient of 50%, meaning at least 50% of the required data had to be available for the software to calculate a strain value. The validity quotient comes into play at edges or a interior location where data was not collected due to the influence of glare or poor speckling.

The Aramis software automatically applies a running averaging to both the displacement and strain data. While the default averaging produced smooth curves, the averaging feature in the software was minimized. To meet this goal, all averaging was removed for the displacement data. The measured strain values were within the

recommended range of the Aramis systems sensitivity, however, some averaging was used to smooth the strain data as some noise was present. A small calculation size of 3 was used to average the strain data.

The Aramis system was used to collect data for the cyclical fatigue tests at standard intervals. The data shows the performance of the MFC after being cycled at the different temperatures. As a measure of performance, the tip displacement of the beam, as well as strain generated within the MFC were analyzed. In order to process the data, three section lines along the y axis of the beam. The global coordinate system for the test specimen is shown in Figure 38. The coordinate system is defined by the Y axis being parallel to the MFC fiber direction, the X direction is in the MFC width direction, and the Z direction being normal to the plain of the MFC, and positive out of the page. As shown in the figure, the X axis is located at the bottom of the piezoelectric fibers, and the Y axis is located at the center of the MFC.

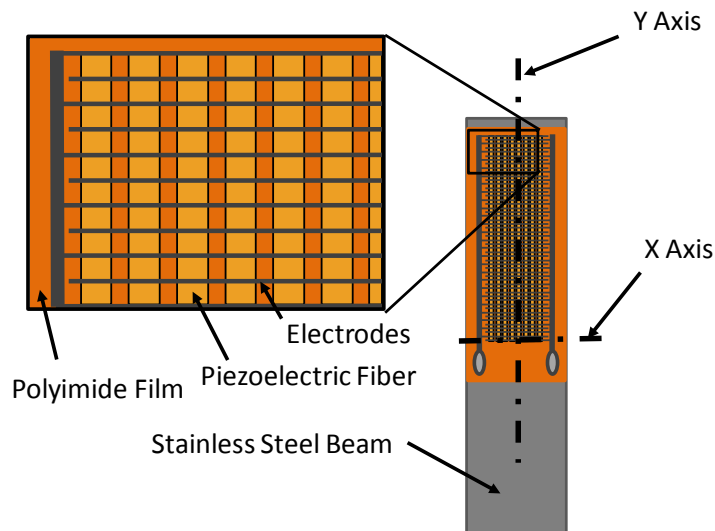


Figure 38: The global coordinate system for the specimen is shown as the Y direction being parallel to the fiber direction of the MFC, the X direction being in the width direction of the MFC and the Z direction being normal to the plain of the MFC, and positive out of the page.

To process data taken with the Aramis system, three section lines of data were taken parallel to the y axis. The section lines were taken along the y-axis at the center of the MFC, and 1mm to each side of the y-axis. The three section lines, as shown in Figure 39, were then averaged together to generate one data set of position, displacement and strain data. Also shown in Figure 39, the bottom inactive area of each specimen was defined as the motion correction area, per the Aramis system operation manual. By enabling the motion correction algorithm, the software eliminates rigid body motion in the system. Rigid body motion would occur as a result of the cameras or the test fixture moving.

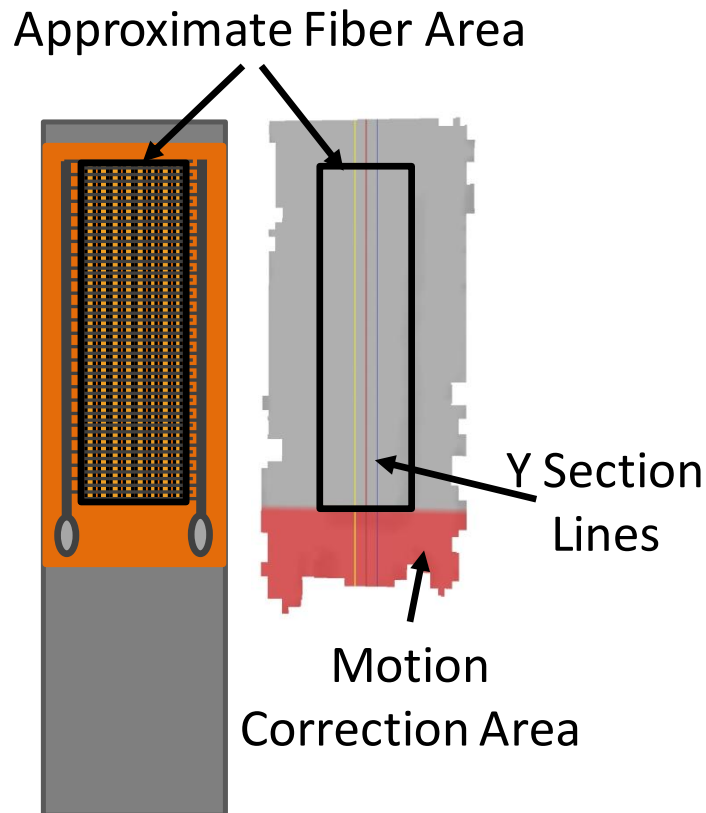


Figure 39: Drawing of specimen and Aramis image side by side, showing the approximant fiber area, the motion correction area and the three section lines

Cyclical Actuation Fatigue Testing

Cyclical fatigue testing over a temperature range from 0 degrees Celsius to 100 degrees Celsius was identified as the area of focus for experiments to be performed as this information was previously unavailable, yet required for the lunar application. To accomplish this testing the prepared specimens were installed into the testing apparatus. The installation process was done by simply clamping the specimen's clamping area between the clamping plate and the upper support. The specimen was oriented vertically, with MFC facing the high voltage wires. The high voltage wires were clamped in the ceramic terminal blocks, and the strain gauge wires were soldered onto the strain gauge. While the specimen was at room temperature, the Aramis system was then used to collect a set of displacement and strain data before any cycling had occurred.

To collect data using the Aramis system, the system's accuracy was first checked using the appropriate calibration artifact and procedure as per the Aramis operation manual. This procedure checks to ensure that the system was setup correctly, and that the system is able to make accurate measurements. If the accuracy was within the allowable limit specified, the system was then moved into position to collect data on the specimen. Data was then collected first with no applied voltage as a reference. Then data was taken with 1000 volts applied to the MFC, as measured with a voltmeter.

The system was then allowed to reach the steady state temperature that the individual test was to be operated at. The Labview program was activated, starting the data recording process. Next the power was turned on to both the 12 volt DC power supply as well as the arbitrary waveform generator, causing the beam to begin vibrating. If necessary, the 12 volt

DC power supply was adjusted so that the positive electrode on the MFC was being charged to 1000 volts, as monitored by the Labview program.

The frequency of the square wave was then adjusted until it matched the first resonant frequency of the beam. The frequency was found using a two step process to ensure that the beam was being driven as close to the first resonant mode as possible. The first step to finding the frequency was to simply watch the beam, and adjust the frequency to where the amplitude of the beam was the largest. Next, the frequency was adjusted to maximize the strain amplitude that was calculated by the Labview data acquisition program reading the strain gauge. This second step of adjustment was only used to fine tune the frequency, and in practice, only small adjustments were found to be necessary. If the natural frequency of the beam was below 104Hz or above 109Hz, the effective length of the beam was adjusted by raising or lowering where the test specimen was mounted in the testing apparatus. This effectively tuned the length of the specimen that was vibrating during the testing.

The tests were then allowed to run until a MFC failure occurred, or until approximately 50million cycles were reached. While the tests were running, they were frequently checked to ensure the test was running at the desired temperature, voltage and frequency. Once one of the two ending criteria were reached the 12 volt power supply as well as the arbitrary waveform generator were turned off, thus ending the test. The entire testing fixture was then allowed to either cool or warm to room temperature. If the specimen reached 50 million cycles without failing, the Aramis system was then used to collect data on the performance of the MFC. Once data was taken, the procedure for running a test was started over and repeated until either the MFC failed or 250 million cycles were reached.

Microstructure Imaging

For further analysis of the fatigue and failure process within the MFC, microstructure images were made. The micrographs were only made from selected specimens that represented the characteristic failure type of an electrical shorting within the MFC, as well as an un-actuated MFC specimen for comparative purposes. The un-actuated MFC was not laminated to a beam, but rather examined in the as-received state.

Before micrographs could be made, test specimens were cast in epoxy to stabilize the specimen while it was cut into the sections that were to be analyzed, as shown in Figure 40. The figure shows the section cut near a failure location, so the location could be imaged and analyzed further. The sectioned materials were then cast in transoptic powder, and polished following standard metallic specimen preparation procedures. A digital camera mounted on an optical microscope was used to capture the images of the prepared specimens.

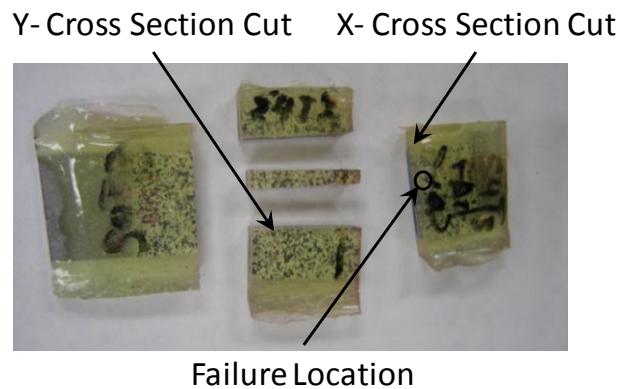


Figure 40: Specimen cast in epoxy, and cut into sections for analysis

EXPERIMENTAL RESULTS AND DISCUSSION

Operational Life at Temperature

The testing of the MFC laminated beams showed a strong relationship between temperature and the operational or useable life of the MFC as a bending actuator. The specimen identifier and testing temperature, presented in Table 3, indicate the tests that were conducted. Figure 41 shows the cycle to failure for the MFC with respect to temperature. All specimens tested 75 degrees Celsius and above experienced a failure, were as the specimens tested at 20 degrees Celsius and at 50 degrees Celsius did not experience a failure. Testing at temperatures of 75 degrees Celsius and above showed a decreasing cyclic life was achieved. The specimen at 75 degrees Celsius only achieved a operable life of 50 million cycles before failure was experienced. The usable life of the specimen at 75 degrees Celsius was only 20 percent of the useable life of the specimens at 20 degrees Celsius and 50 degrees Celsius, which never experienced failure.

Table 3: Specimen Identifier and Testing Temperature for experiments conducted

Specimen Identifier	Testing Temperature (Celsius)
S7T6	-15
S2T1	20
S6T5	50
S5T4	75
S8T7	90
S4T3	95
S3T2	145

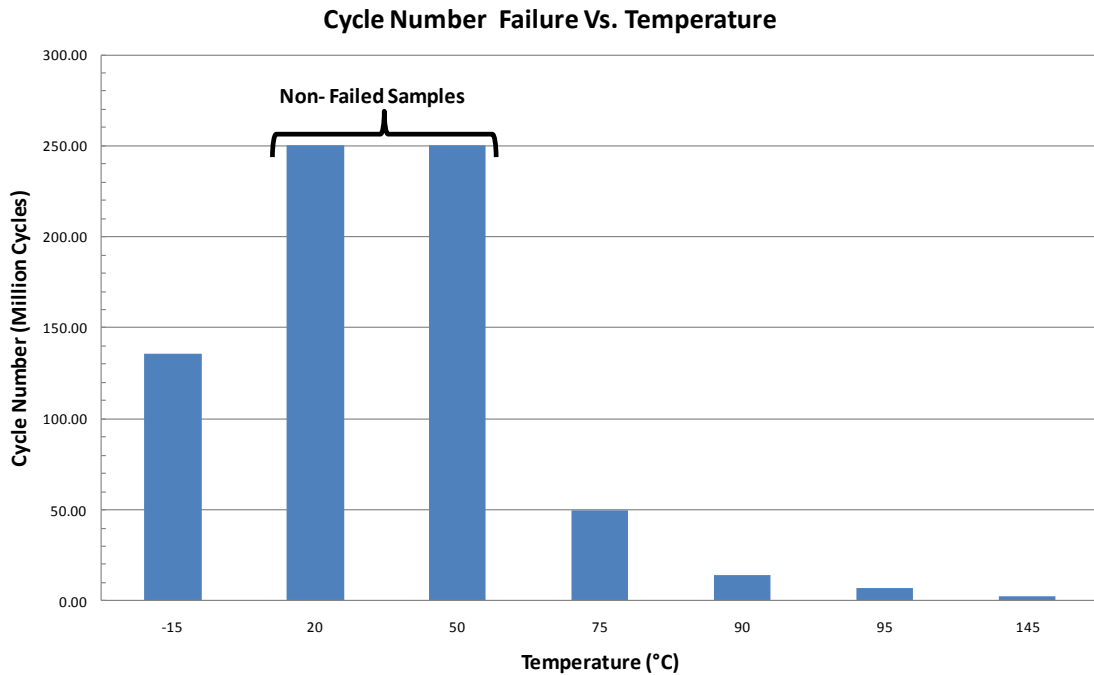


Figure 41: Results for cyclical fatigue testing indicating cycles to failure with respect to temperature

The temperature dependent operational life of the MFC was evident for temperatures above 75 degrees Celsius. The specimen tested at 95 degrees Celsius lasted 7.2 million cycles, or 2.8 percent of the measured life at 50 degrees. The measured life at 145 degrees Celsius was only 2.72 million cycles, displaying a usable life of only 1.1 percent of the measured life of the specimens that did not experience a failure. This trend shows a significant reduction in usable life of the MFC as the temperature of the operating environment is increased. The technical specifications for the MFC, provided by Smart Materials indicate a maximum operating temperature of 80 degrees Celsius (Smart Material Corporation). The results of the current experimental testing, however, indicate that while

there is significant reduction in the expected usable life of the MFC as operating temperature is increased, the MFC could be operated at elevated temperatures.

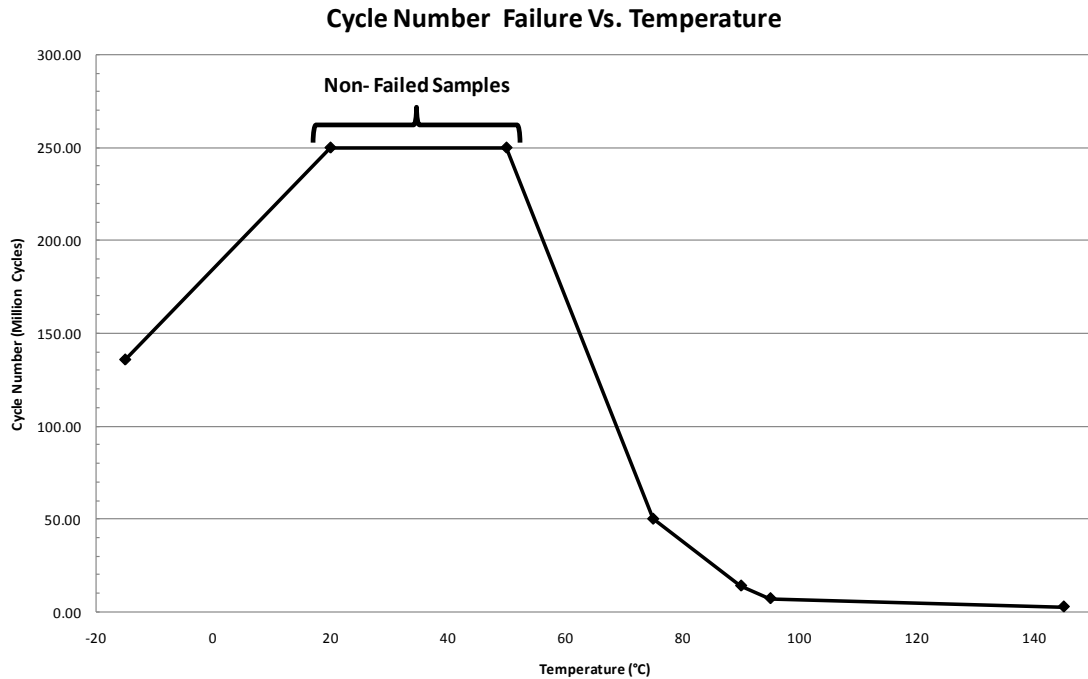


Figure 42: Scatter plot of Cycle number to failure verses temperature indicating the specimens at 20 degrees Celsius and 50 degrees never reached failure

MFC Cyclical Performance

In addition to the usable life of the MFC, the performance of the system was monitored. The Aramis system was used at cyclical intervals to monitor the static performance of the MFC. The Aramis system produces three dimensional position, and displacement data, as well as, two dimensional strain data. This data was processed to show the performance of the MFC as the MFC was cycled. Data was calculated for each specimen at each cyclical interval showing position, displacement and strain data. Before discussing this data, it is important to understand the orientation of the coordinate system used to define

the data. The global coordinate system for the test specimen is shown in Figure 43. The coordinate system is defined by the Y axis being parallel to the MFC fiber direction, the X direction is in the MFC width direction, and the Z direction being normal to the plain of the MFC, and positive out of the page. As shown in the figure, the X axis is located at the bottom of the piezoelectric fibers, and the Y axis is located at the center of the MFC.

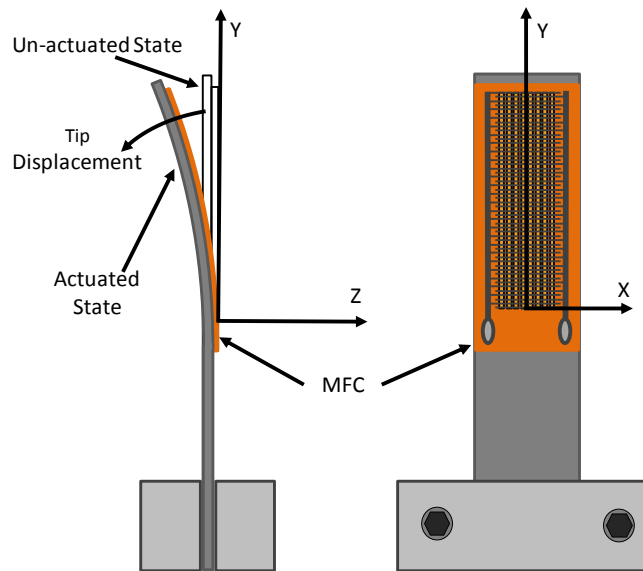


Figure 43: Drawing of the test specimen indicating the specimen coordinate system.

Data was collected along the three section lines located parallel to the Y-axis in the center of the MFC, and 1mm to each side of the center of the MFC. The data from the three section lines was averaged together to generate one data set for analysis. For the points along the section, the data set contained three dimensional position data, three dimensional displacement data, as well as strain data in the X and Y directions. From this data, analysis was performed on only a subset of the overall data set. The data used in the analysis was the position data in the Z direction, the strain in the Y direction, and the displacement in the Y

and Z directions. For comparative purposes, a normalized form of the data is presented in the in format shown in Figure 44. Data in this format is presented at each cyclical interval for each specimen in Appendix A.

The Z position along the cross section, defined the surface contour of the specimen. As shown in Figure 44, this contour was used to identify the coordinates of the bottom edge of the piezoelectric fibers. This location was used to define the zero position along the cross section, with the positive direction towards the unclamped end of the beam. The Z position data was also used to locate the flat plateau, above the top edge of the piezoelectric fibers on the polyimide film of the MFC, indicated in Figure 44. The location of this plateau was used to define the location where the tip displacement would be measured. The Y strain and Y displacement are also shown in the figure.

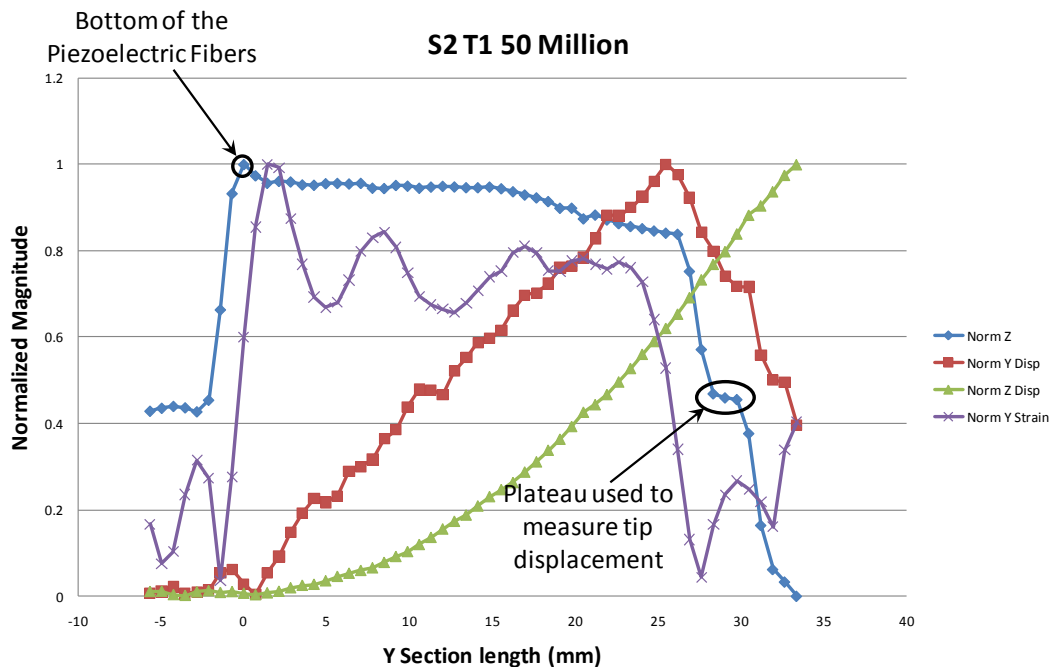


Figure 44: Example of normalized data showing each type of data from the Aramis system, as well as the features used to identify the bottom of the piezoelectric fibers and the plateau used to measure the tip displacement

Tip Displacement

The specimen tip displacement was used to characterize the performance of the MFC as it was cyclically actuated. The Z displacement data from the Aramis system shows the beam curvature as the beam bends in response to the actuation of the MFC. The magnitude of this curvature or the deflection at a point on the beam is directly related to the performance of the MFC, and would decrease as the performance of the MFC degraded.

The plateau defined by the Z position data covered several points along the Y section length. These position data points along the section length also defined Z displacement data points associated with the corresponding physical feature on the test specimen. The Z displacement data points along this feature were averaged together to form one tip displacement measurement, as shown in Figure 45. The location along the Y section length of the resulting tip displacement measurement point was also calculated as a comparison between specimens. Figure 46 shows the Z displacement along the Y section length for each cyclical interval for one specimen. The figure shows the approximant location of the edges of the Z position plateau as well as the approximant location of the tip displacement measurement.

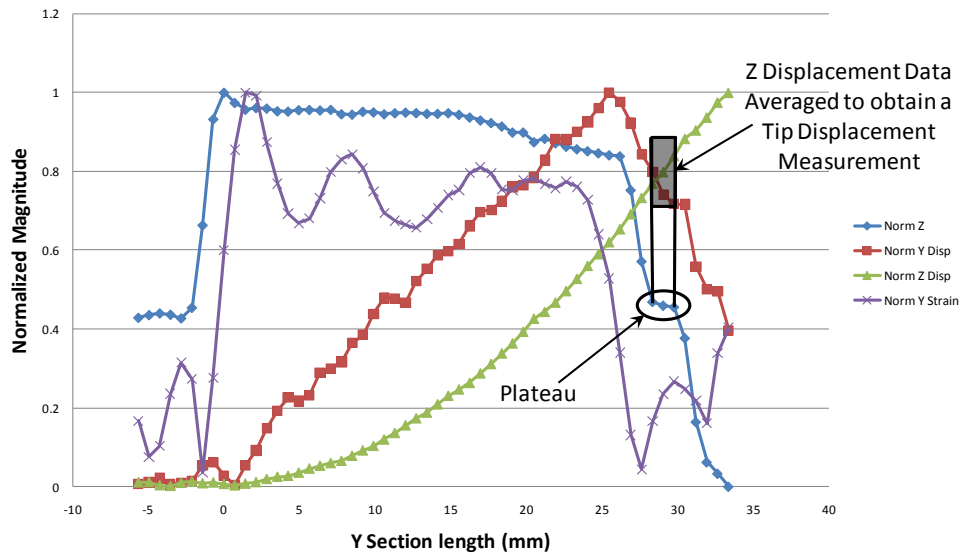


Figure 45: Example Data indicating how the Z position Plateau was used to define the Z displacement data points used in tip displacement measurement

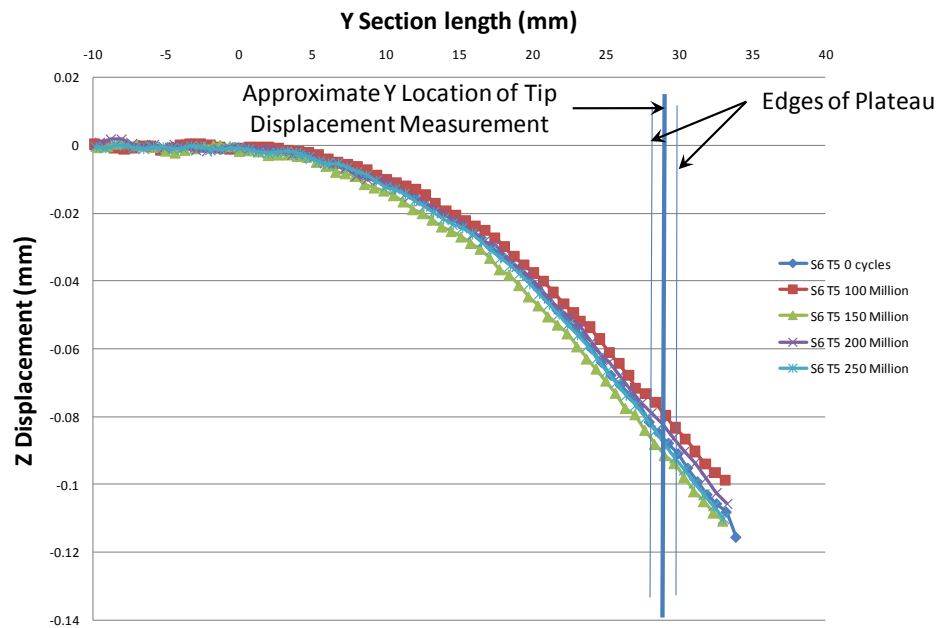


Figure 46: Example data showing the Z displacement along the Y section length showing the Y location of the plateau defined by the Z position data, and, the approximate location of the tip displacement measurement

Z displacement data at the location on the specimen for measuring the Z displacement data has a significant slope. Therefore, it is important that the location for measuring the tip displacement be consistent. The location of the tip displacement measurement along the Y section length is shown in Figure 47. The figure shows the consistency in the measurement location between specimens, and indicates the level of repeatability that was achieved during the data collection and processing procedure.

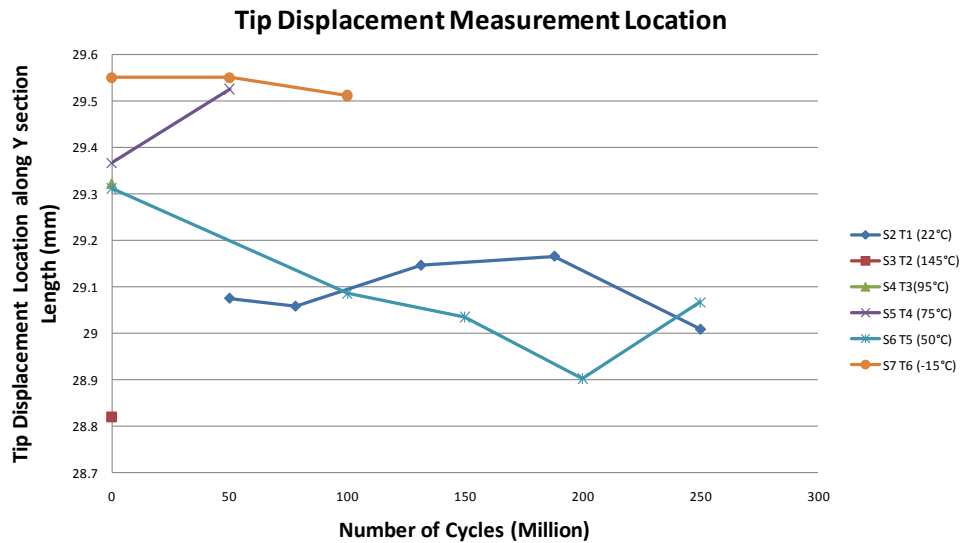


Figure 47: Graph showing the location along the Y section of the tip displacement measurement

The measured tip displacements for each specimen were also plotted against the number of cycles that each specimen had actuated when data was taken. The results, presented in Figure 48, show no indication of cyclical dependence on performance. This was true even for data collected before failure occurred, indicating that the failure mechanism was independent of the performance on the MFC. This trend is also evident in Figure 49, which shows the Z displacement data for each cyclical interval of each testing specimen. The

curvatures of each specimen closely resemble each other, regardless of testing temperature or the number of actuation cycles that the specimen endured.

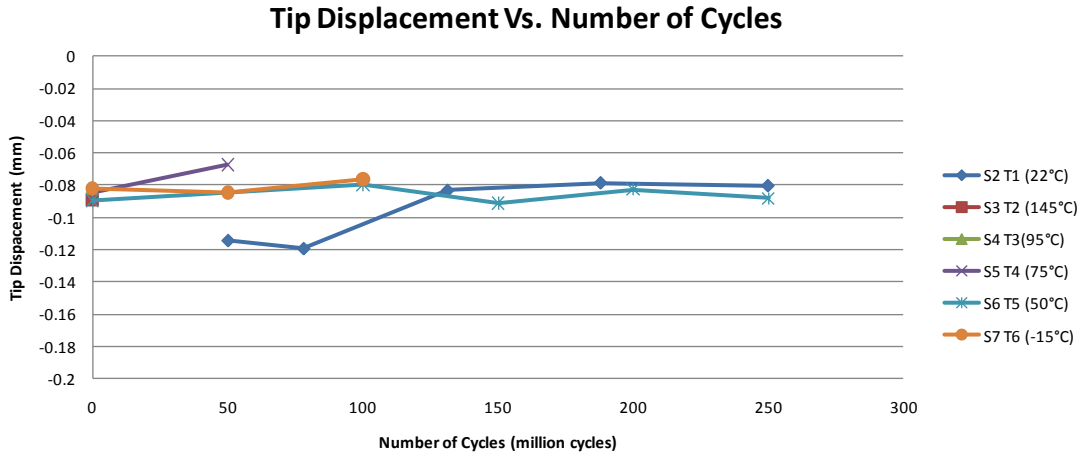


Figure 48: Experimental data showing the tip displacement for each specimen at the intervals measured

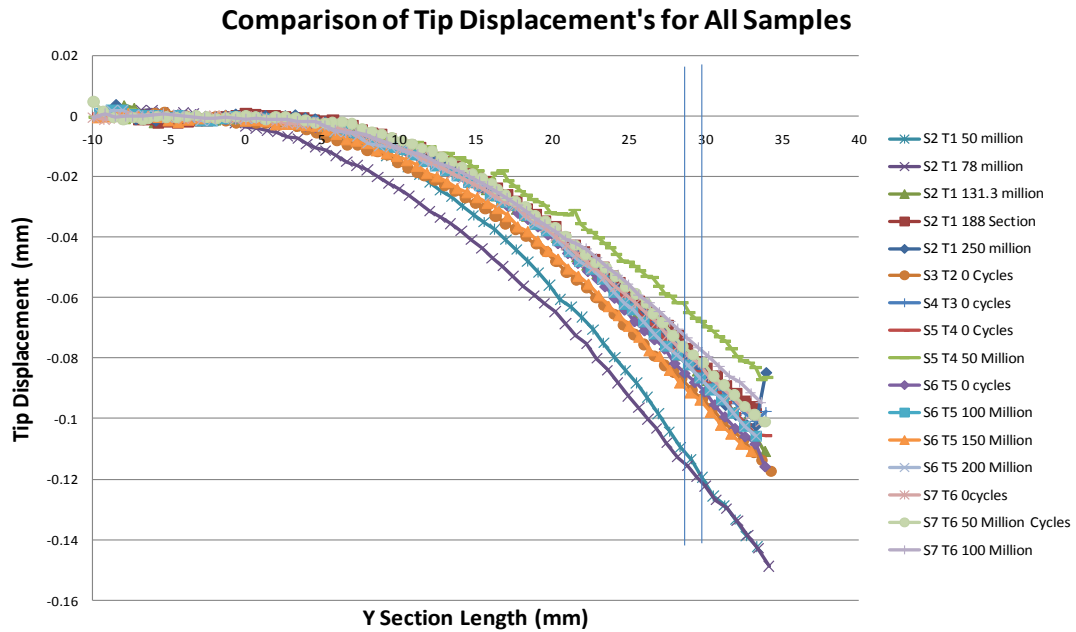


Figure 49: Z displacement data for each cyclical interval of each specimen

Strain comparison

The strains produced by the MFC were within the recommended range specified for the Aramis system, however, some noise can be seen in the strain data collected with the Aramis system. The strain data does provides useful information for comparing MFC performance, specifically to the calculated strain for this type of piezoelectric beam laminate.

The strain data was processed in a manner in which comparisons could be made both between the different test specimens, as well as between a test specimen and the calculated strain values. In order to form a basis for comparing the strain data, the Z position data was used to identify the section length on the beam were strains could occur. As the piezoelectric fibers are the source of the strain within the specimen, the section length where piezoelectric fibers exist was the section length used to analyze the strain. To approximate the location on the piezoelectric fibers, the edges of the central plateau in the Z position data were identified. This is only an approximation of the actual length of the fiber as the edges of the plateau actually indicate the physical edge of the region of the MFC containing the fibers, and not the actual end of the fibers, however, these features are closely related to the fiber position. Figure 50 shows the locations used to approximate the location of the ends of the piezoelectric fibers. The strain within this section length should be constant, and so the strain was averaged over this section length. By averaging the strain for analysis, any changes in strain along the section length cannot be seen.

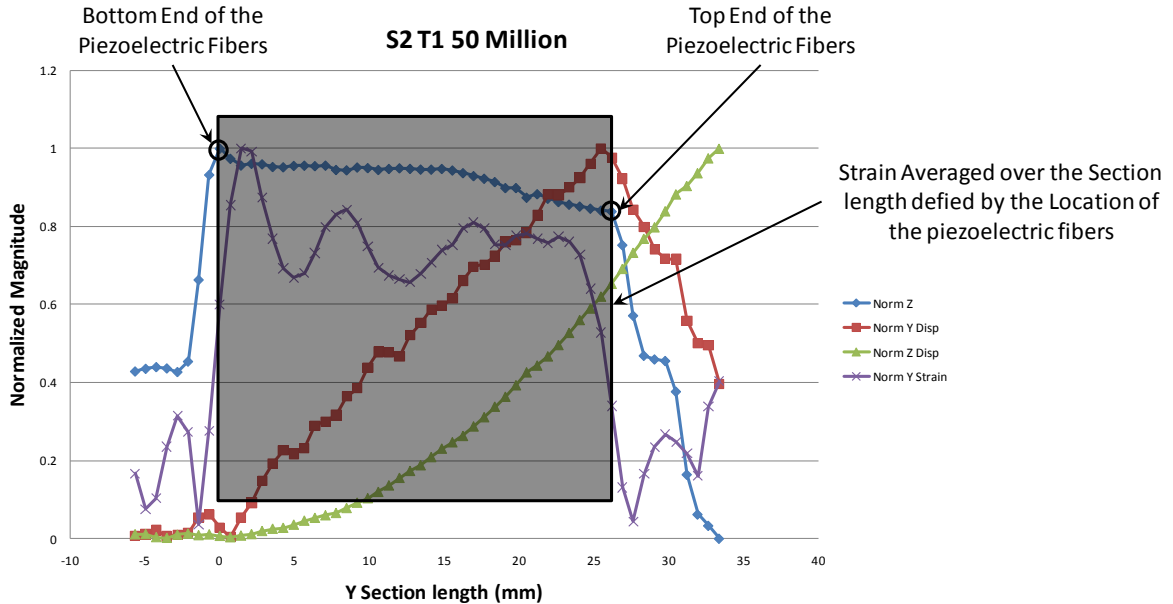


Figure 50: The Strain data was averaged over the section length containing piezoelectric fibers

Based on the Bernoulli-Euler beam assumptions, the strain within the top layer of the MFC should be 181.47micro strains based on the manufacture's material specifications. This calculation along with the averaged strain data were plotted with the original strain data, as shown in Figure 51. The graph indicates that the average of the measured strain data is similar to that calculated over the fiber length. The value of the averaged strain for each cyclical interval of each specimen can then be shown side by side, as in Figure 52, which also includes the calculated strain at each interval. The data shows no strong correlation between the number of cyclical actuations and strain level.

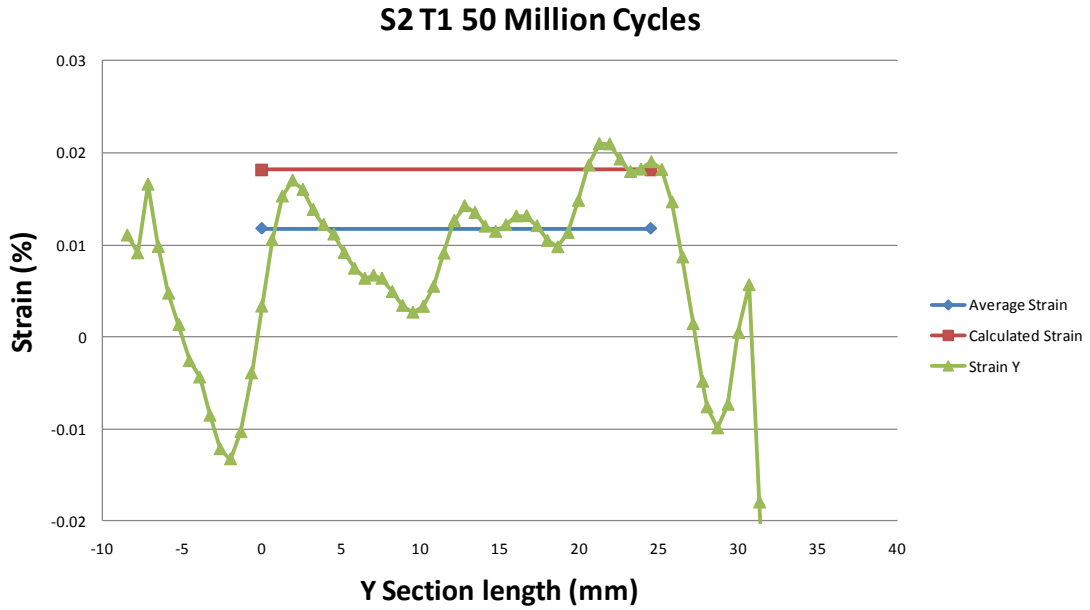


Figure 51: Strain data shown for specimen S2 T1 after 50 million cycles over the Y section length. The average strain and calculated strain are also shown over the averaging section length

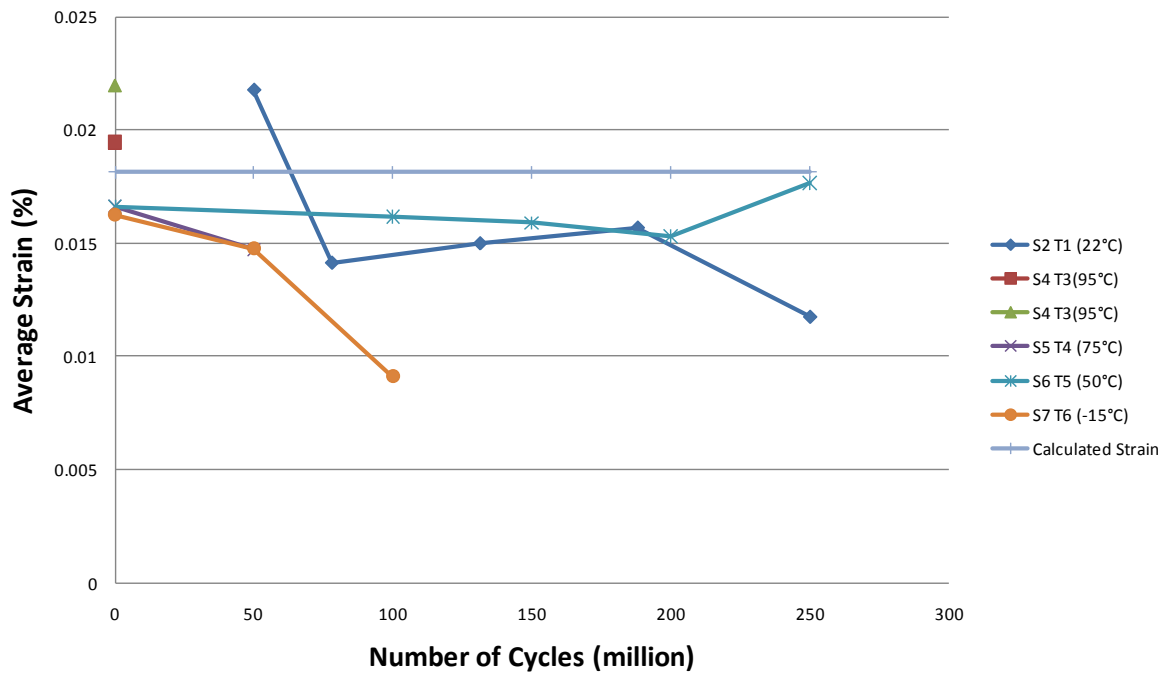


Figure 52: Average strain for each cyclical interval of each specimen shown alongside the calculated strain

Microstructure Imaging

Analysis of the microstructure images revealed cracking within the piezoelectric fibers for the specimen that had been fatigued. Cracking was evident in the images from both the X and Y- cross Section. Figure 53 shows an un-actuated MFC specimen with no apparent cracking. This image shows piezoelectric fibers free of cracks, the epoxy between the fibers, and the electrodes.

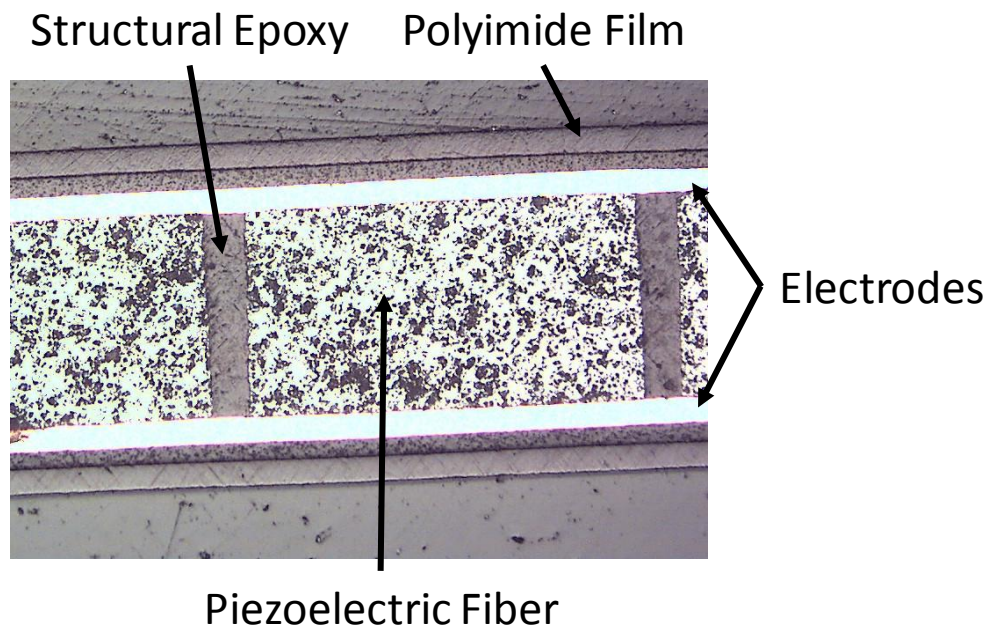


Figure 53: Microstructure image of an un-cycled MFC, showing the components that make up the composite. The piezoelectric fibers show no cracking or evidence of degradation

An image from a failed specimen, as seen in Figure 54, shows cracking within the piezoelectric fibers. The figure shows the X cross section of the failed specimen, away from the failure location. The image shows no change in the structural epoxy holding the MFC together, or in the polyimide film, however, the cracking is localized to the fibers.

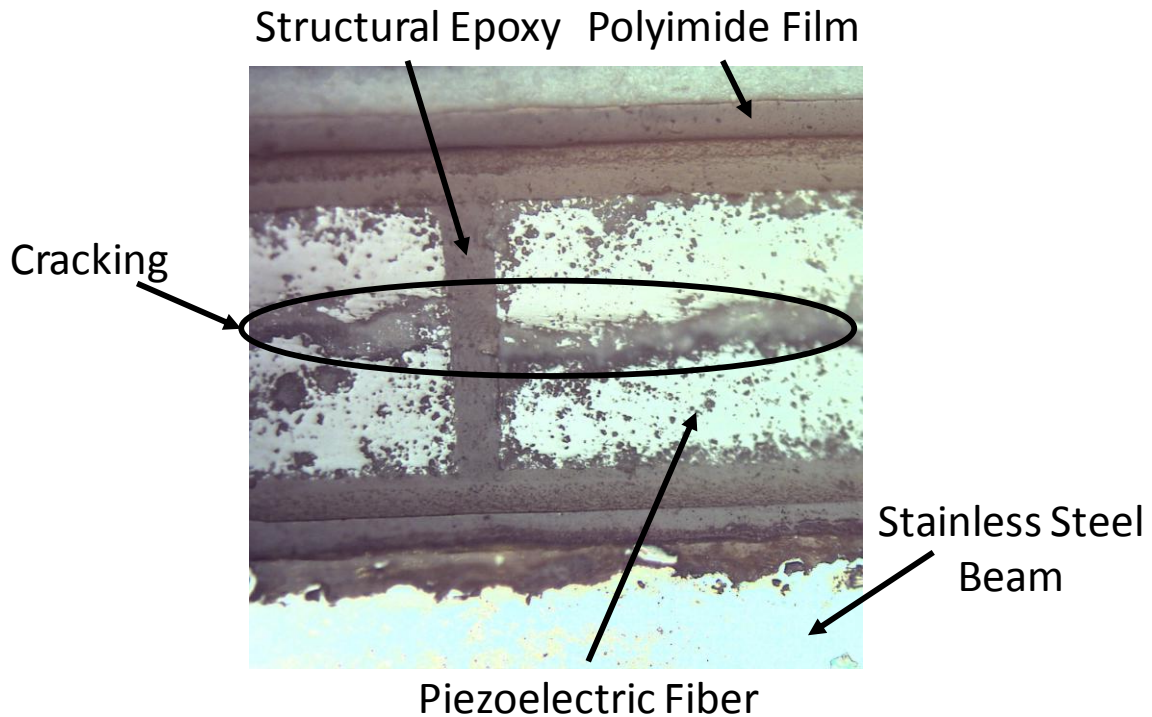


Figure 54: Microstructure image of a failed specimen showing cracking within the piezoelectric fibers

Cracking similar to that seen in the X cross sections is also evident in the Y cross section images. Figure 55 shows a comparison between a failed specimen and an un-cycled MFC. In the figure, widespread horizontal cracking can be seen within the failed specimen. Vertical cracks can be seen in the un-actuated MFC, however, the cracks appear at relatively standard distances along the section length. The cracks could have originated during the manufacturing of the MFC, or possibly are evidence that the fibers are actually made of small segments of fibers rather than continuous fibers. Cracking within the piezoelectric fibers of MFC's has been documented for the d_{31} effect MFC's. The investigation concluded that the

cracking did not affect the performance of the MFC and was tolerated by the composite as a whole (Nuffer, Schönecker and Kohlrautz).

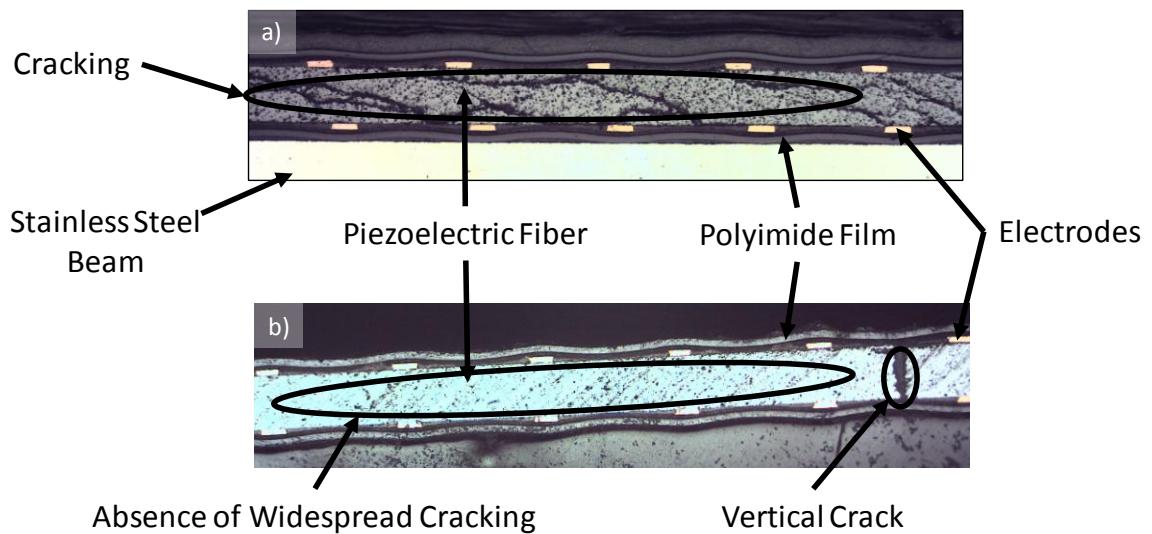


Figure 55: Microstructure image along the Y cross section comparing cracking in the piezoelectric fibers a) of a failed specimen, and b) a un-cycled MFC

Specimen Failure

Specimen failures occurred from the MFC failing electrically, and becoming non-operational. The specimens that did experience failures failed in this manner, which was characterized by a electrical shorting between the positive and negative electrodes within the MFC. The electrical failures could have stemmed from mechanical origins, such as cracking or changing material properties within the constituents. While the exact failure mechanism is unknown, the failures either stems from the mechanical or electrical degradation of one or multiple of the composite constituents, eventually resulting in electrical arching between electrodes. Figure 56 shows specimen S4 T3 after it was cycled to failure. The figure shows

the location of the electrical failure which appears as a brown discoloration on the surface of the MFC. The discoloration is caused by burning of the surface from the heat of the electrical arching that occurs after failure.

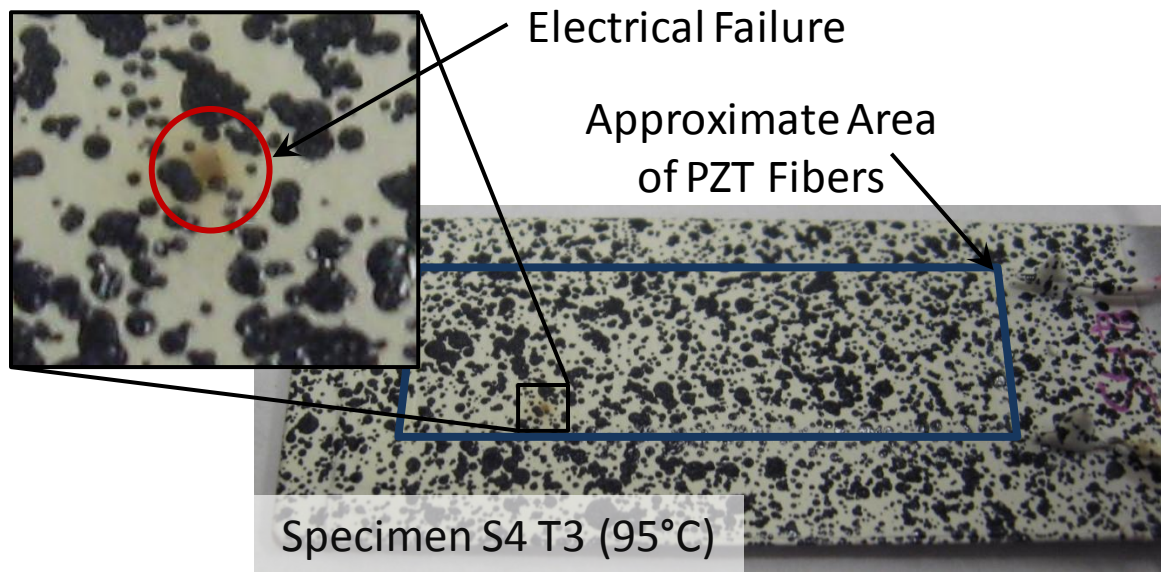


Figure 56: Specimen S4 T3 with the point of failure indicated

CONCLUSIONS

MFC's have been evaluated and experimentally tested to determine the usable life and performance of the composite structure under a variety of operating temperatures as the MFC was cyclically actuated. The usable life of the MFC shows significant temperature dependence, with failures occurring after fewer actuation cycles as the operating temperature is increased. The dependence of the operating temperature on the usable life of the MFC is an important parameter to be considered when incorporating an MFC into any system design. The MFC's exhibit an extremely long operational life under cyclic actuation, making the MFC's a good solution for any actuator design where reliability is a primary consideration.

The experimental testing has shown MFC's to exhibit minimal degradation in performance as the MFC's are cyclically actuated. The performance even showed minimal degradation up to specimen failure, making the operational life of the MFC extend out to the point of failure. This characteristic also makes the MFC a useful actuator, as the performance characteristics do not exhibit any dependence on number of cyclic actuations the MFC has endured.

For use as a valve actuator for lunar exploration, the experimental testing of the MFC's has produced valuable data for determining the required thermal environment that any actuator using an MFC must maintain. The testing effort has also produced useful information for predicting the usable life of the MFC when operated at elevated temperatures, where eventual failure from cyclical actuation is either expected or the required number of cyclical actuations is low.

Further investigation could include investigating the dependence of the MFC's operational life on the mechanical boundary conditions. This would be done by changing the beam geometry, and thereby changing the mechanical boundary conditions that the MFC is constrained by. In a similar manor to investigating the influence of the mechanical boundary conditions on the useable life the MFC, the influence of the electrical boundary conditions could also be investigated. Experimental testing could also be performed at a variety of frequencies including non-resonate frequencies to determine the influence actuation frequency on operational life.

WORKS CITED

Bent, Aaron A. and Alessandro E. Pizzochero. "Recent Advances in Active Fiber Composites for Structural Control." Smart Structures and Materials 2000: Industrial and Commercial Applications of Smart Structures Technologies 2000.

Bent, Aaron A. and Nesbitt W. Hagood. "Improved performance in Piezoelectric Fiber Composites using interdigitated electrodes." Proc. SPIE. San Diego, 1995. 196-212.

Brown, Dwayne. NASA-NASA Instrument... 24 9 2009. 10 4 2010
<<http://www.nasa.gov/topics/moonmars/features/moon20090924.html>>.

Hagood, N., et al. "Improving Transverse Actuation of Piezoceramics using Interdigitated Surface electrodes." 1917 (1993).

Hyde, T. Tupper and Gregory Agnes. "Adaptive Structures." Aerospace America (2000): 68.

Kim, Dae-Kwan, Jae-Hung Han and Ki-Jung Kwon. "Wind tunnel tests for a flapping wing model with a changeable camber using macro-fiber composite actuators." SMART MATERIALS AND STRUCTURES 2009.

Kunzmann, J. and Th. P. Daue. "MFC-Piezoactuators for Optimized Energy Harvesting Systems." n.d.

Leo, Donald J. Engineering Analysis of Smart Material Systems. Hoboken: John Wiley & Sons, Inc., 2007.

Levy, David H and Dr. Tony Phillips. NASA - Moon Water. 10 4 2010
<http://www.nasa.gov/vision/universe/solarsystem/14apr_moonwater.html>.

Martel, Linda M. V. "Planetary Science Research Discoveries." 4 6 2003. 28 8 2009
<<http://www.psrhawaii.edu/June03/lunarShadows.html>>.

Matt, Howard M and Francesco Lanza di Scalea. "Macro-fiber Composite Piezoelectric Rosettes for Acoustic Source Location in Complex Structures." Smart Materials and Structures (2007): 1489-1499.

NASA- JPL. "Space Program Summary No. 37-27, Vol 1." 1964.

NASA-Home. 8 April 2010 <<http://www.nasa.gov>>.

Nuffer, Dr. J., et al. "Reliability Investigation of Piezoelectric Macro Fiber Composite (MFC) Actuators." Adaptronic Congress. Göttingen, 2007.

Omega Piezo. Vibrating Elements. 2008. 13 4 2010
<http://www.omegapiezo.com/vibrating_elements_unimorph_equivalent.html>.

Optotune. Optotune. 2008. 2009 28 8 <<http://www.optotune.com>>.

Ruggiero, Eric, Gyuhae Park and Daniel Inman. "Smart Materials in Inflatable Structure Applications." (n.d.).

Scalea, Francesco Lanza di, et al. "Health Monitoring of UAV Wing Skin-to-spar Joints Using Guided Waves and Macro Fiber Composite Transducers." n.d.

Schönecker, Andreas J., Thomas Daue and Bruckner. "Overview on Macro Fiber Composite Applications." Smart Structures and Materials 2006 2006.

Schultz, Marc R and Michael W Hyer. "A Morphing Concept Based on Unsymmetric Composite Laminates and Piezoceramic MFC Actuators." 45th AIAA/ASME/ASCE/AHS/ASC. Palms Springs : American Institute of Aeronautics and Astronautics, 2004. 1-13.

Smart Material. 12 4 2010. 14 4 2010 <<http://www.smart-material.com/Smart-choice.php?from=Whatis>>.

Smart Material Corporation. 22 4 2010 <http://www.smart-material.com/media/Publications/MFC-brochure_2010_V3.0.pdf>.

Sodano, Henry A., Gyuhae Park and Daniel J. Inman. "An Investigation into the performances of macro-fiber composites for sensing and structural vibration applications." n.d.

Solar System Exploration. 11 2 2008. 21 8 2009 <<http://solarsystem.nasa.gov/index.cfm>>.

Srinivasan, A. V. and D. Michael McFarland. Smart Structures Analysis and Design. New York: Cambridge University Press, 2001.

Whitesides, Loretta Hidalgo. "Micro-Fiber Composite Actuator Named NASA Government Invention of the Year." Wired Science 2007.

Wilkie, W. Keats, et al. "Low-Cost Piezocomposite Actuator for Structural Control Applications." 3991 (2000).

Wilkie, W., J. High and J. Bockman. "Reliability Testing of NASA Piezocomposite Actuators." n.d.

Williams, Dr. David R. Ice on the Moon. 10 4 2010 <http://nssdc.gsfc.nasa.gov/planetary/ice/ice_moon.html>.

Williams, R. Brett, Daniel J. Inman and W. Keats Wilkie. "Temperature-Dependent Coefficients of Thermal Expansion for Macro Fiber Composite Actuators." n.d.

Williams, R. Brett, et al. "An Overview of Composite Actuators with Piezoceramic Fibers."
n.d.

—. "Manufacturing and Cure Kinetics Modeling for Macro Fiber Composite Actuators."
1741 (2004).

APPENDIX A:

GRAPHS SHOWING DISPLACEMENT AND STRAIN DATA FOR EACH SPECIMEN
AFTER EACH CYCLICAL INTERVAL

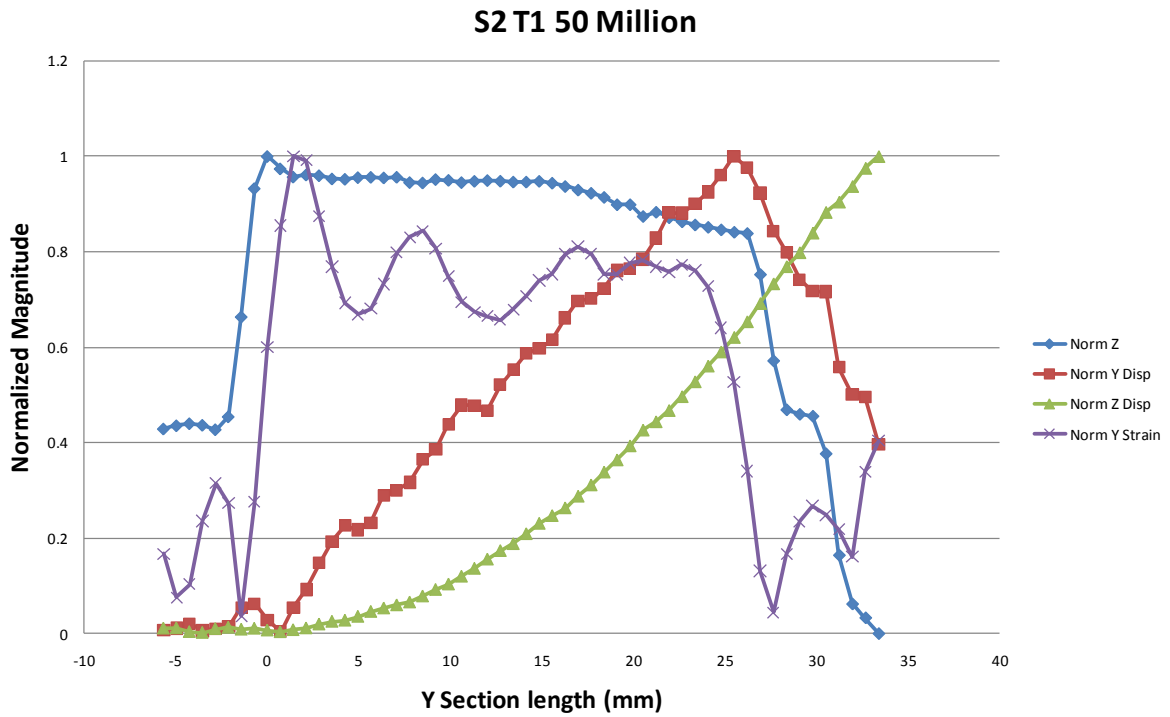


Figure 57: Normalized displacement and strain data for S2 T1 after 50 million cycles

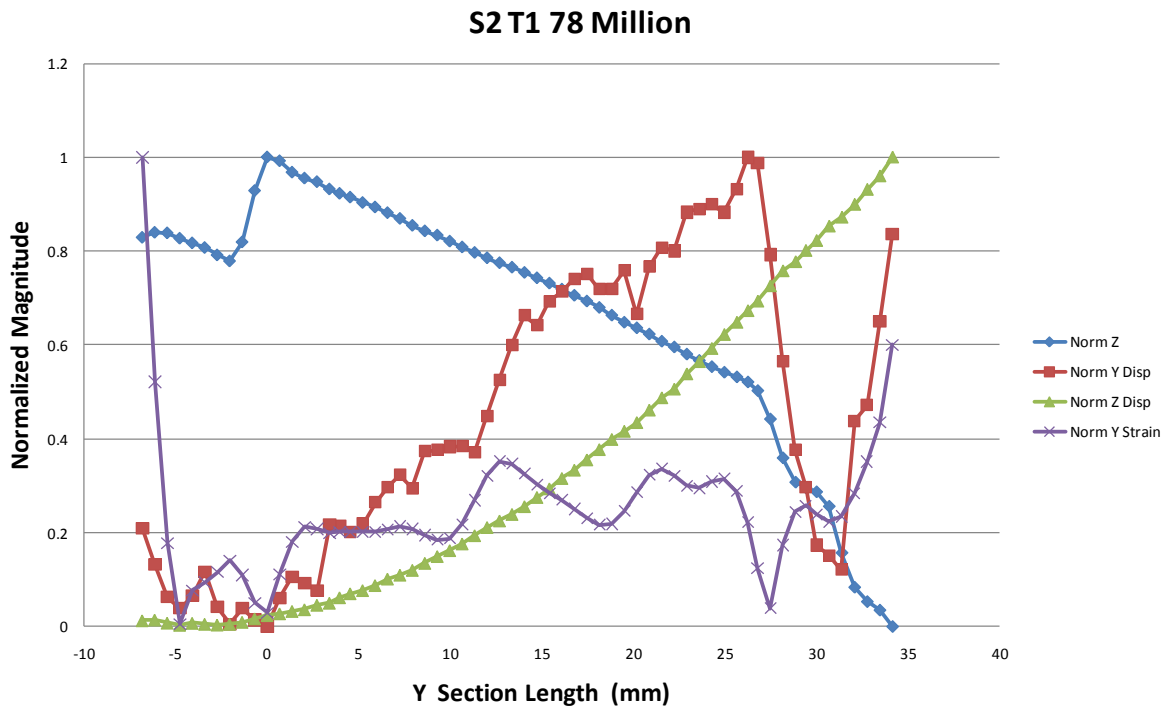


Figure 58: Normalized displacement and strain data for S2 T1 after 78 million cycles

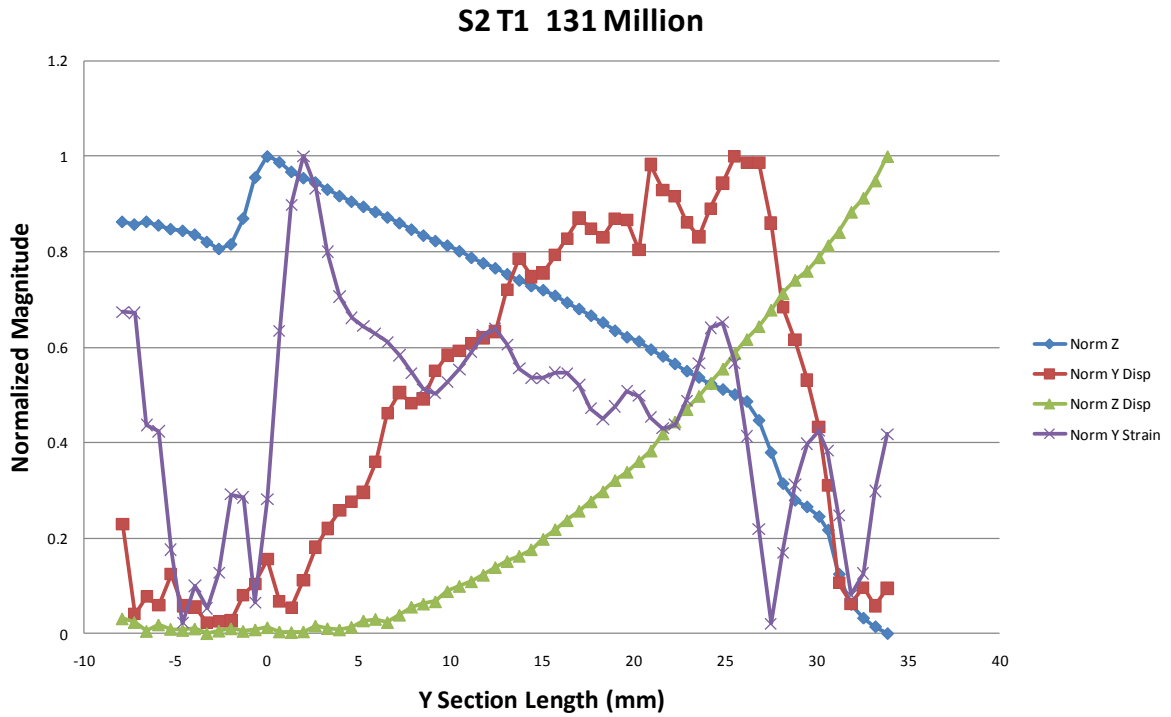


Figure 59: Normalized displacement and strain data for S2 T1 after 131 million cycles

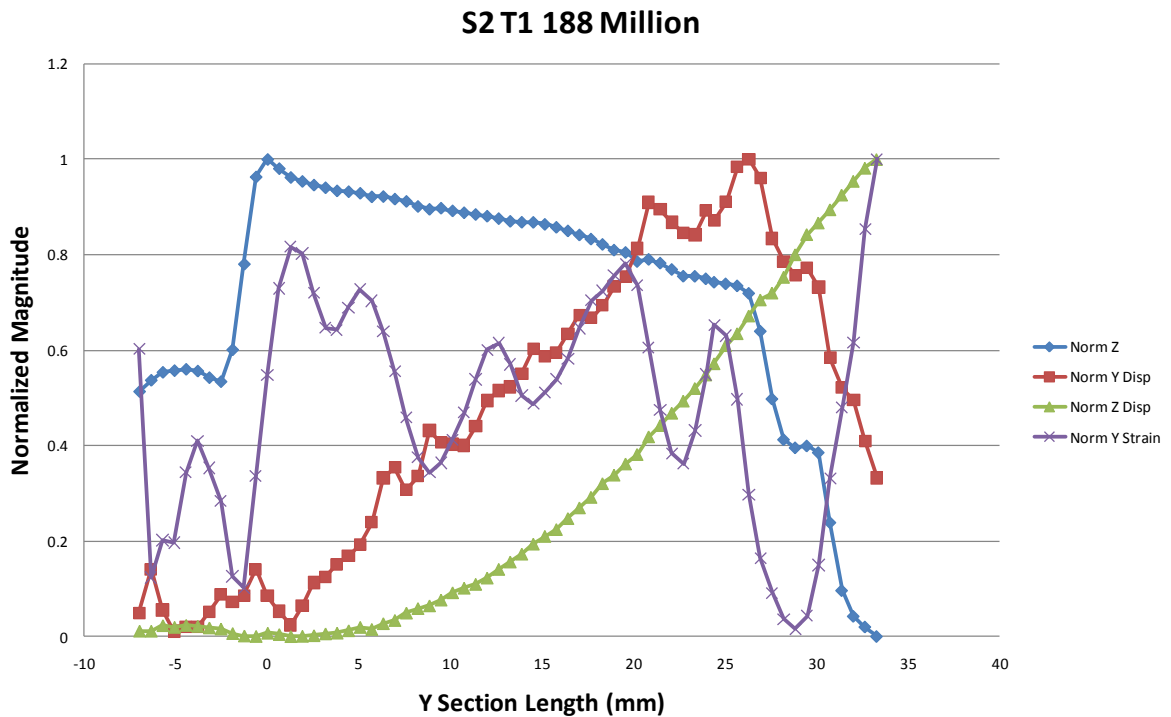


Figure 60: Normalized displacement and strain data for S2 T1 after 188 million cycles

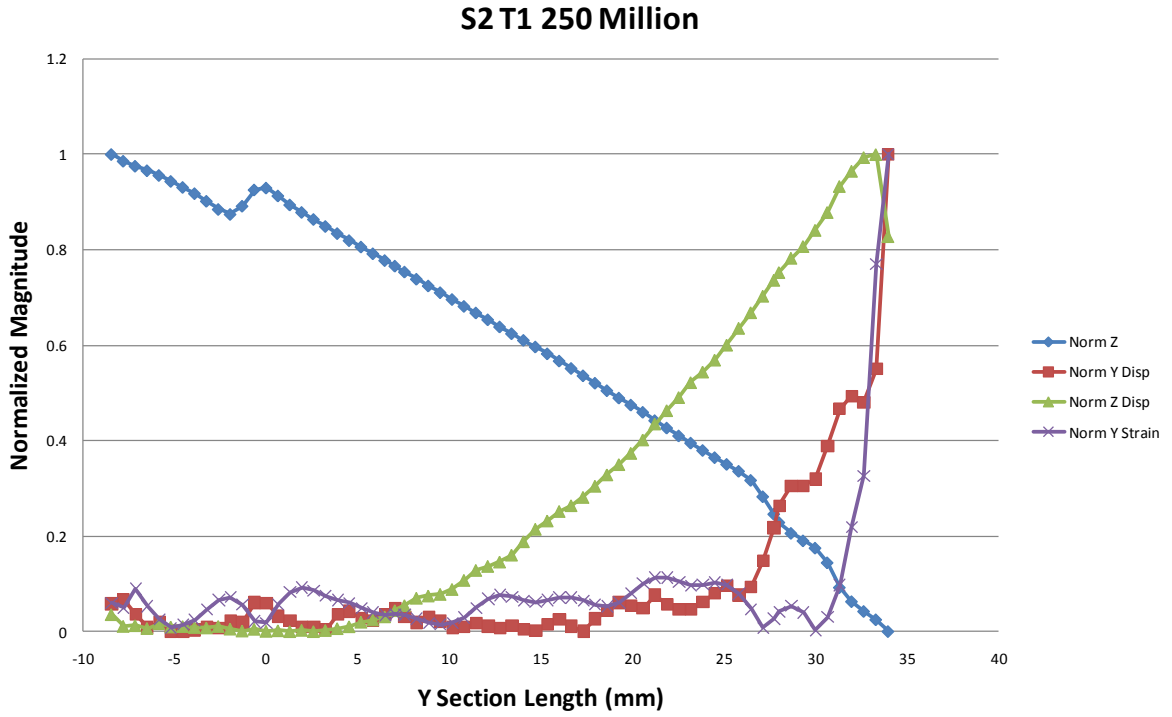


Figure 61: Normalized displacement and strain data for S2 T1 after 250 million cycles

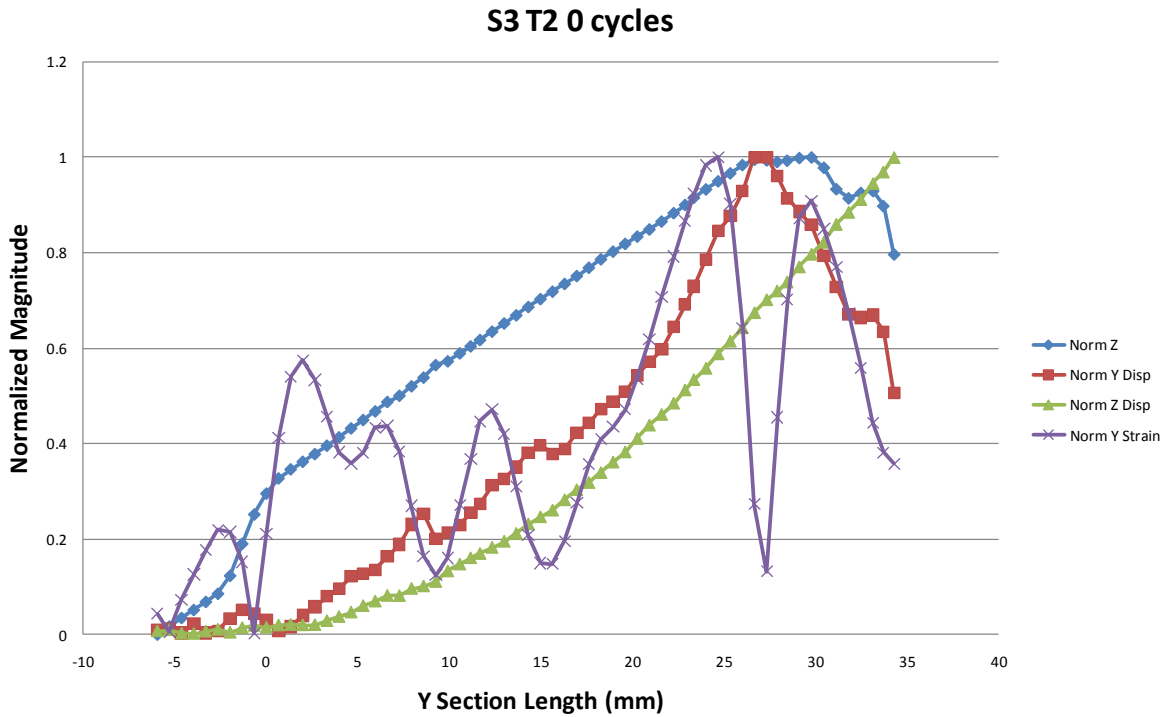


Figure 62: Normalized displacement and strain data for S3 T2 after 0 cycles

S4 T3 0 Cycles

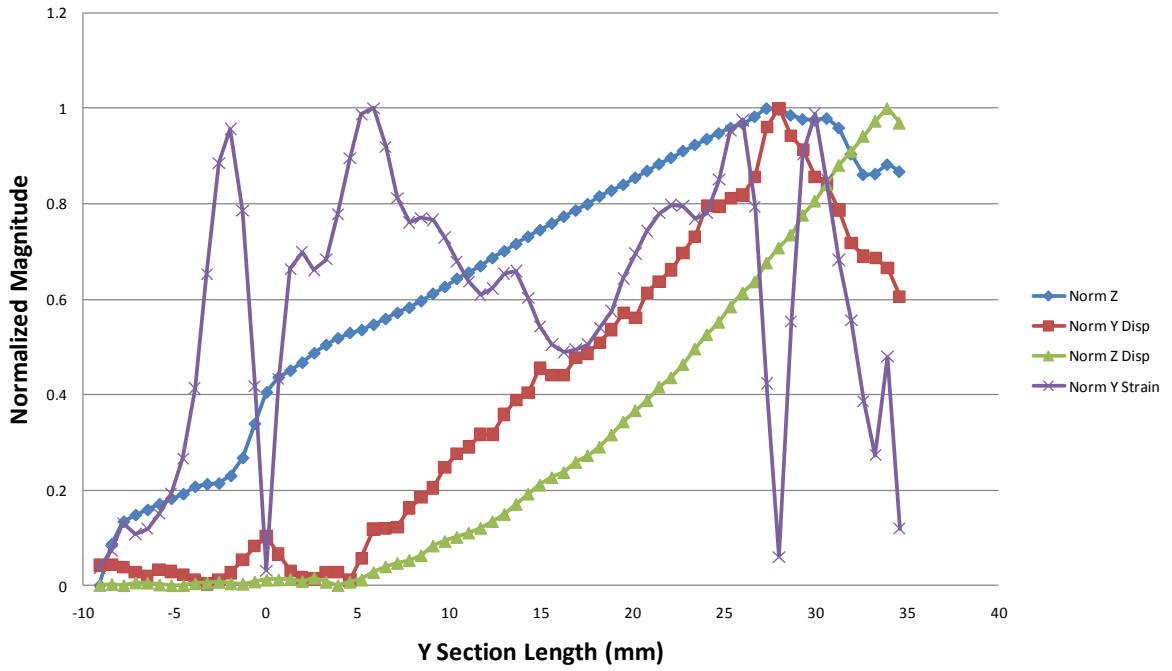


Figure 63: Normalized displacement and strain data for S4 T3 after 0 cycles

S5 T4 0 Cycles

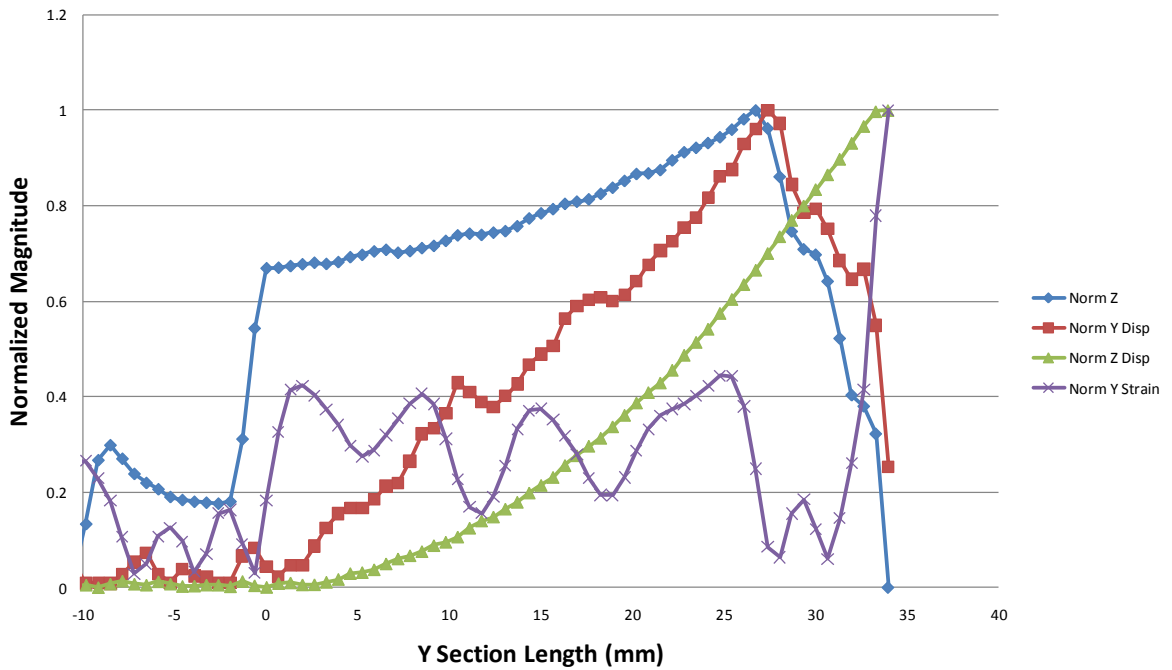


Figure 64: Normalized displacement and strain data for S5 T4 after 0 cycles

S5 T4 50 Million

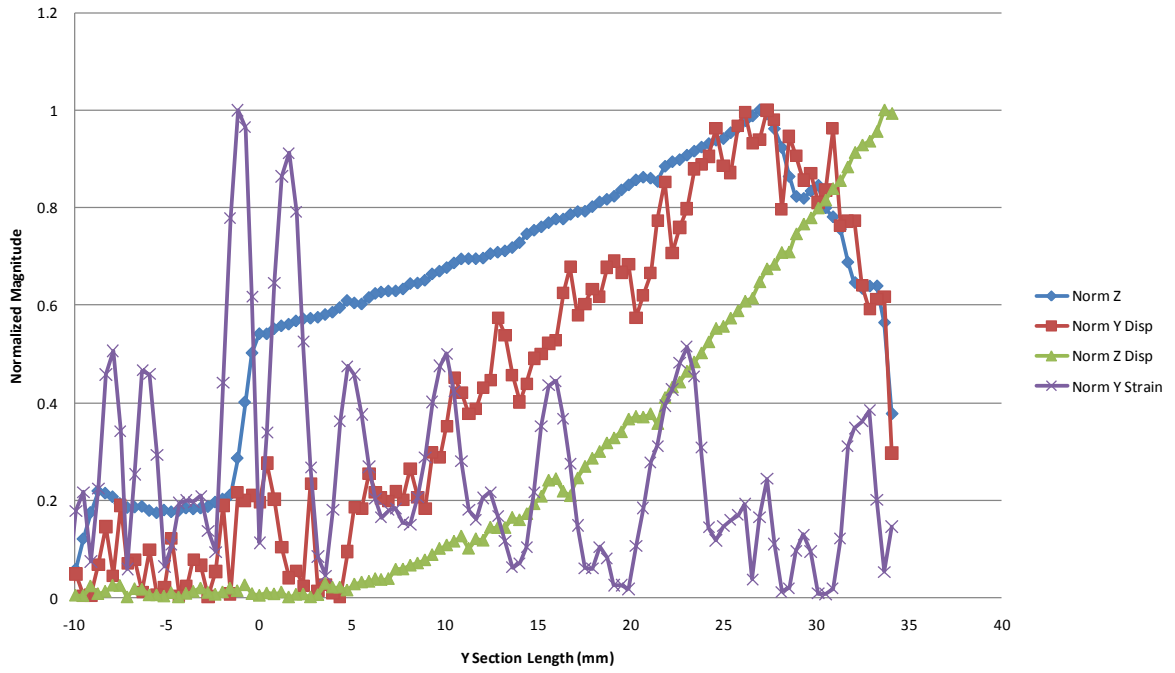


Figure 65: Normalized displacement and strain data for S5 T4 after 50 million cycles

S6 T5 0 cycles

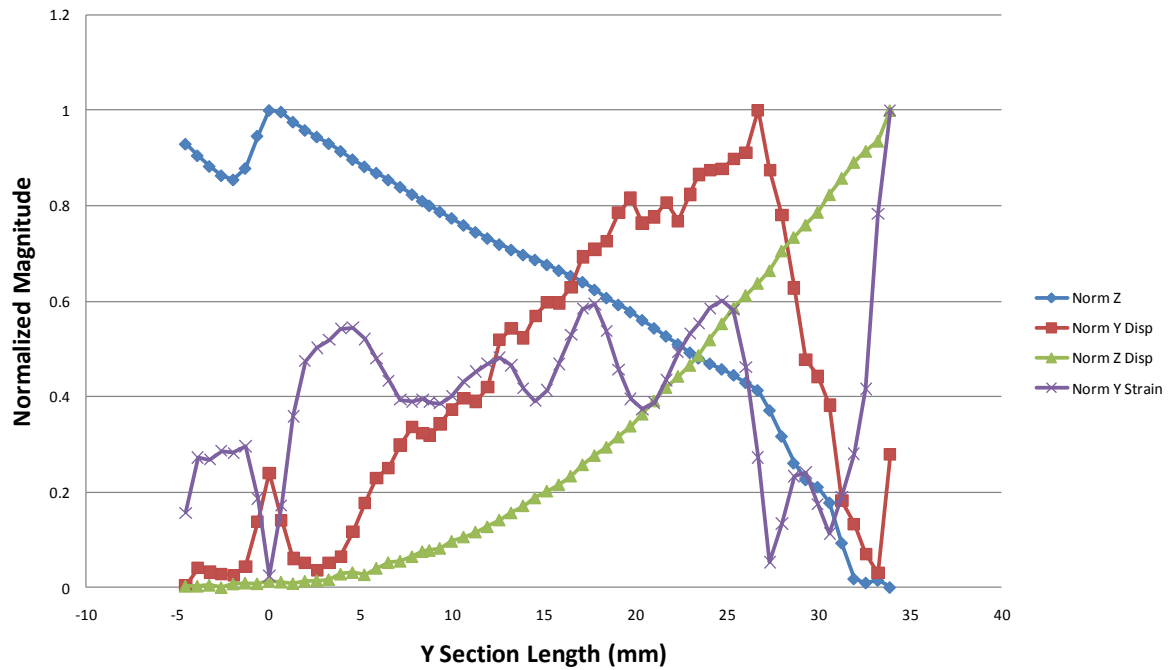


Figure 66: Normalized displacement and strain data for S6 T5 after 0 cycles

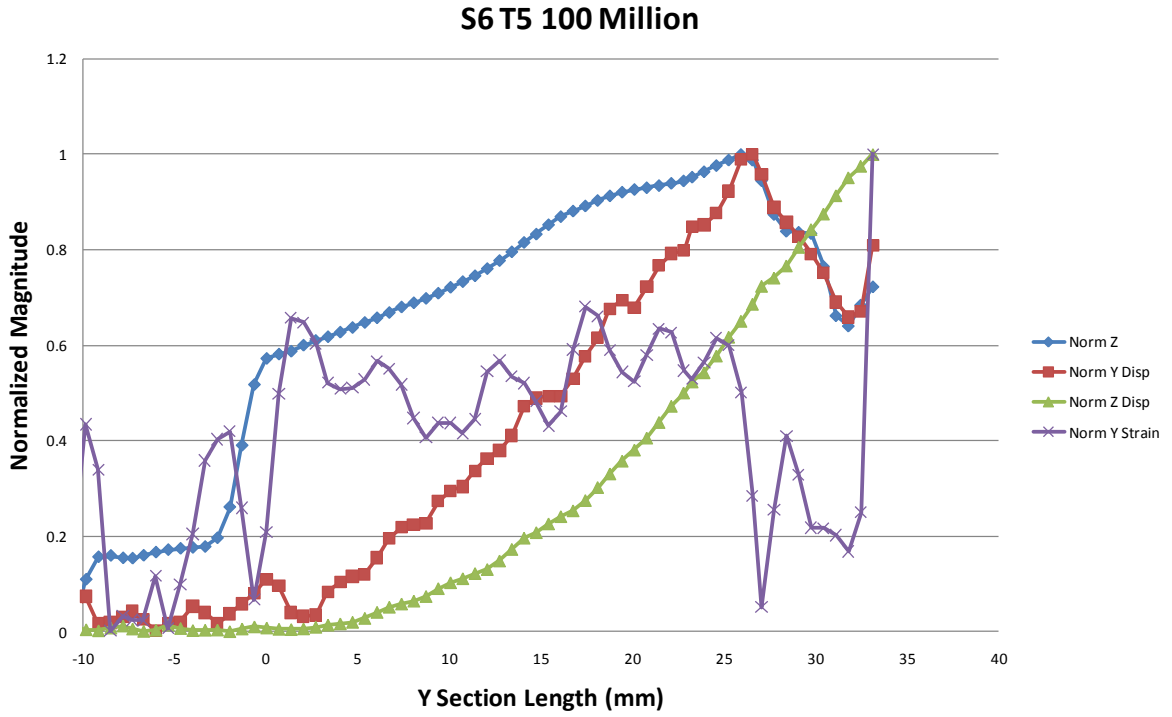


Figure 67: Normalized displacement and strain data for S6 T5 after 100 million cycles

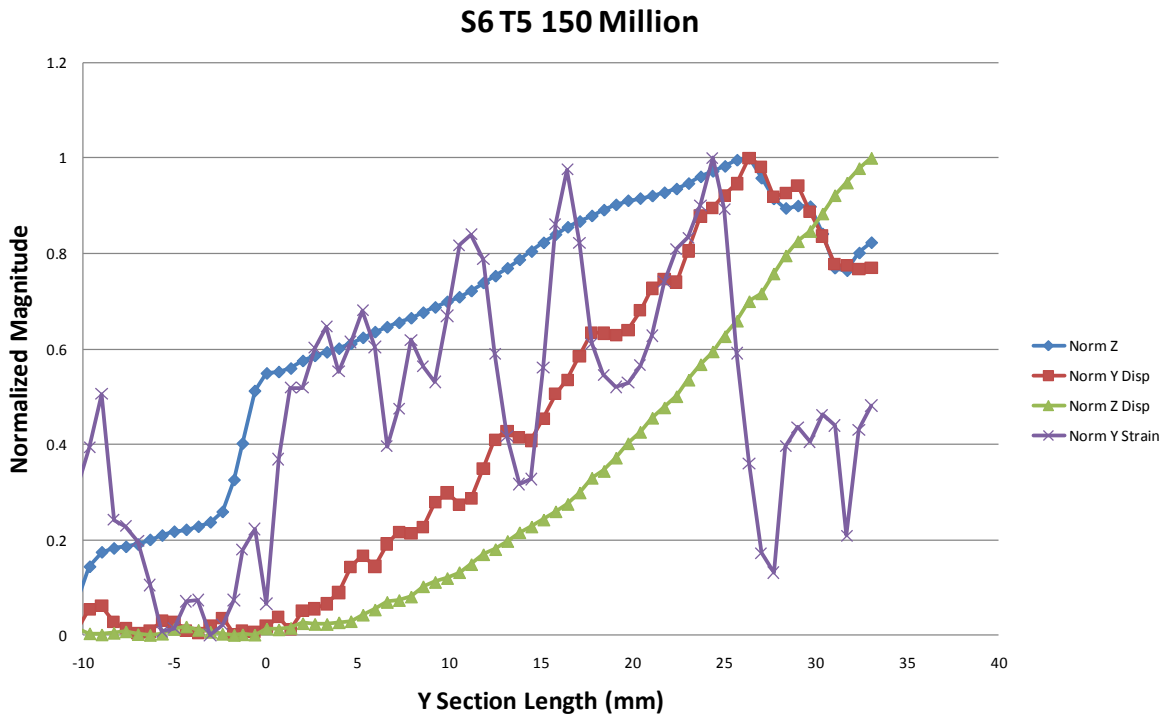


Figure 68: Normalized displacement and strain data for S6 T5 after 150 million cycles

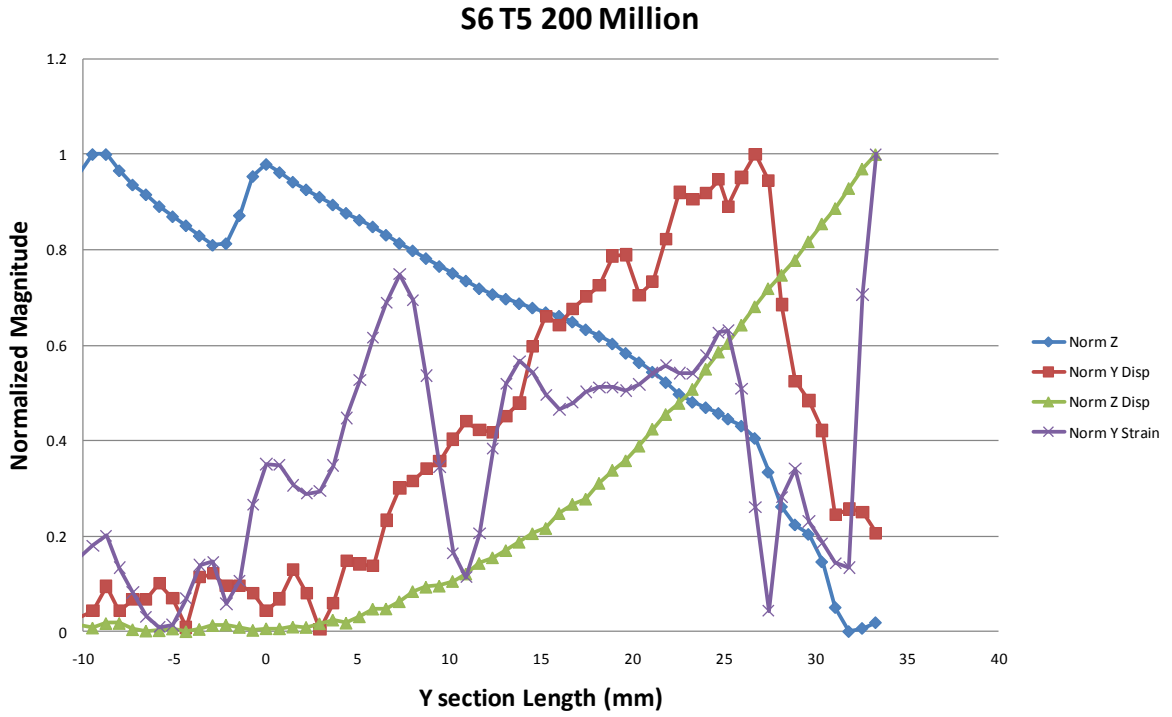


Figure 69: Normalized displacement and strain data for S6 T5 after 200 million cycles

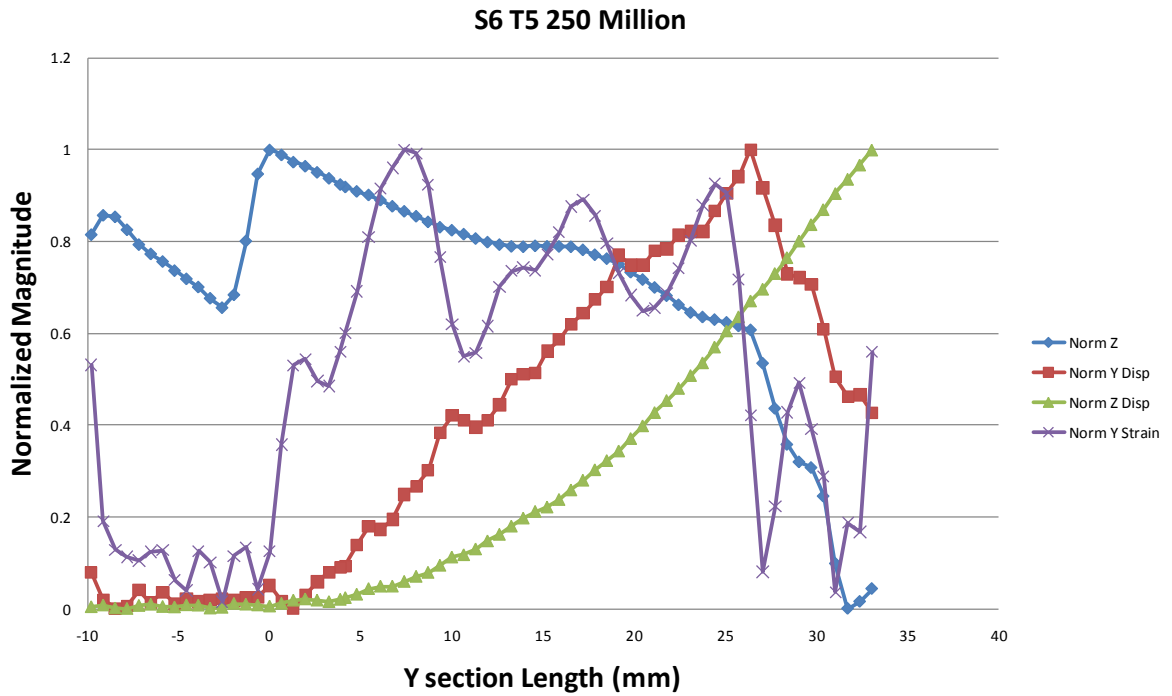


Figure 70: Normalized displacement and strain data for S6 T5 after 250 million cycles

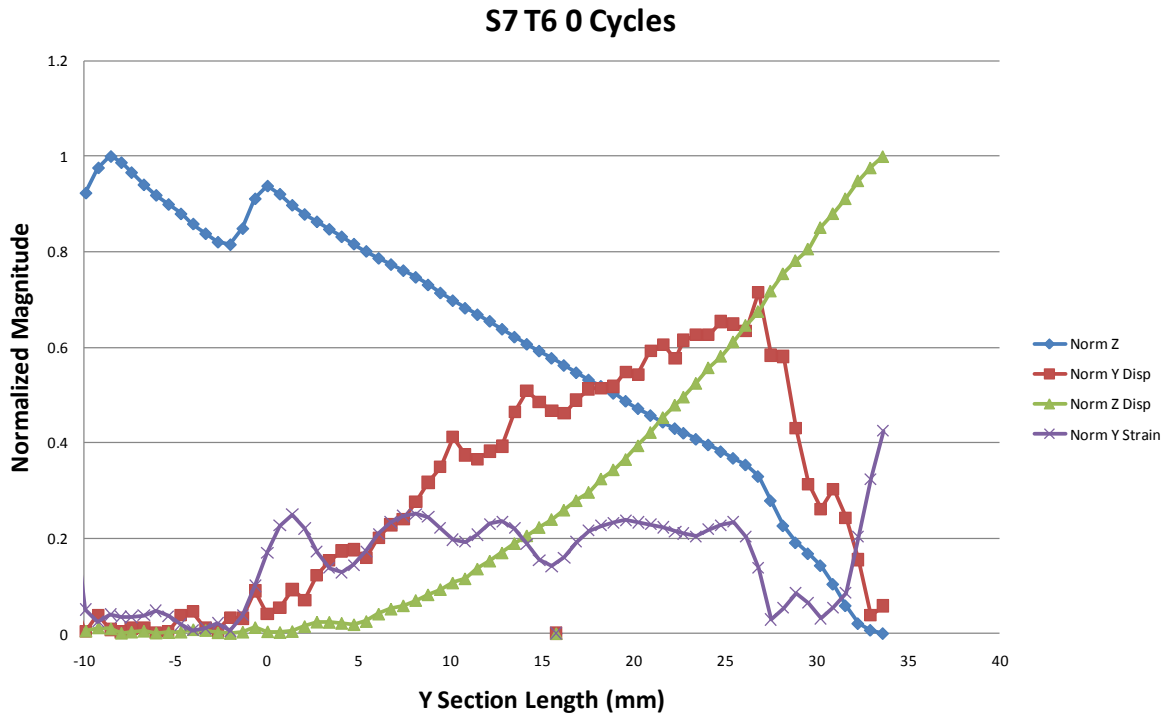


Figure 71: Normalized displacement and strain data for S7 T6 after 0 cycles

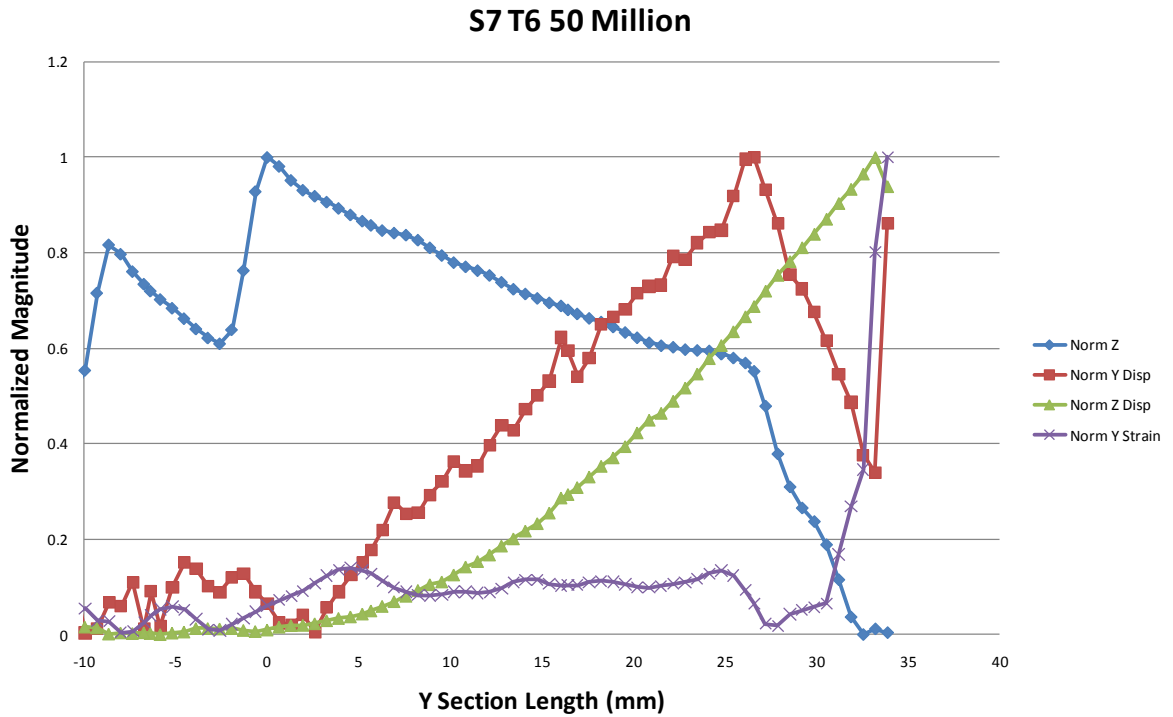


Figure 72: Normalized displacement and strain data for S7 T6 after 50 million cycles

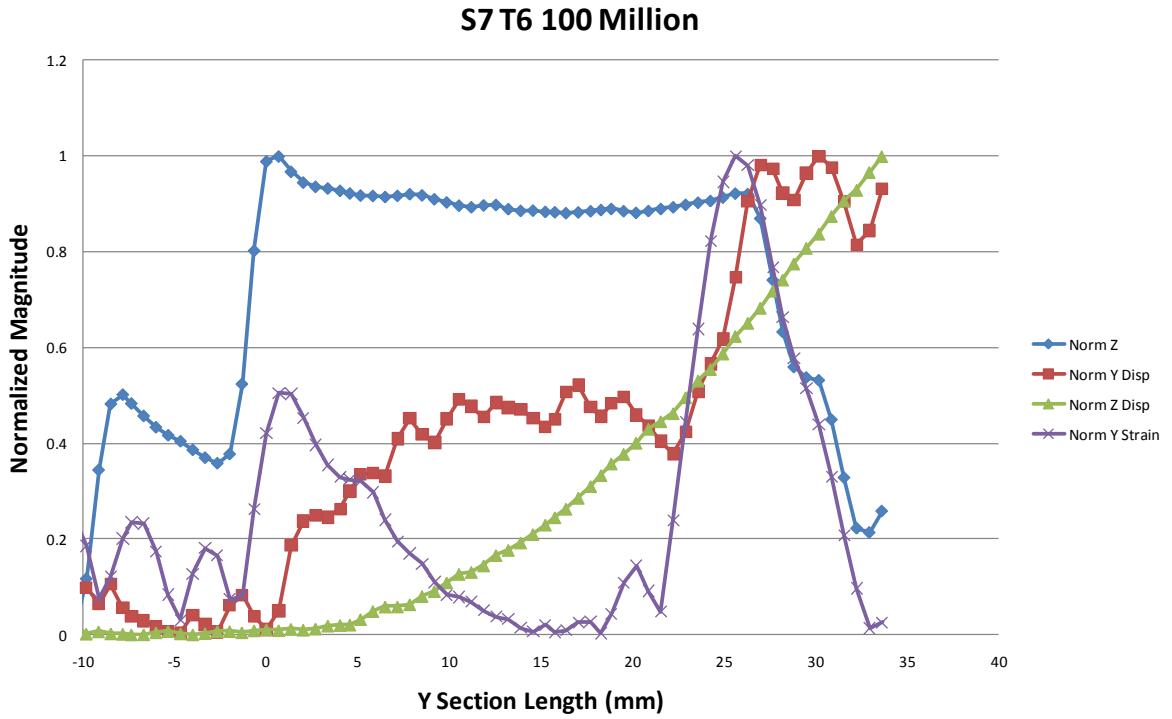


Figure 73: Normalized displacement and strain data for S7 T6 after 100 million cycles

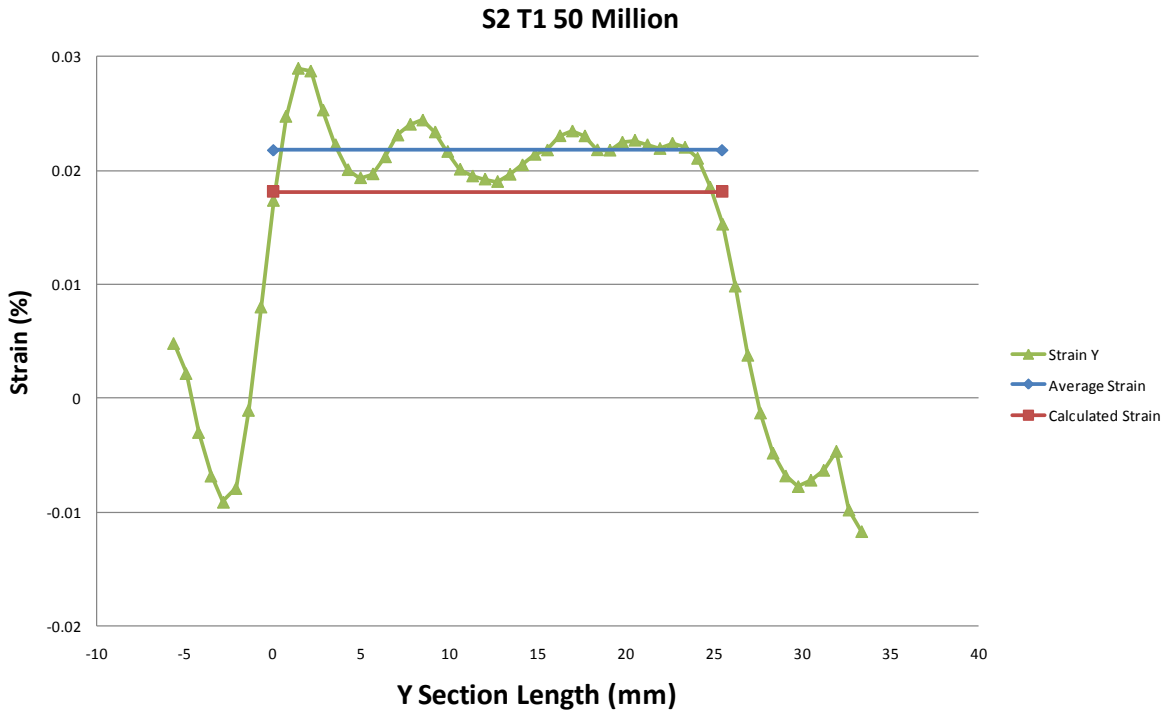


Figure 74: Strain data compared to the average strain and calculated strain for the specified section length for S2 T1 after 50 million cycles

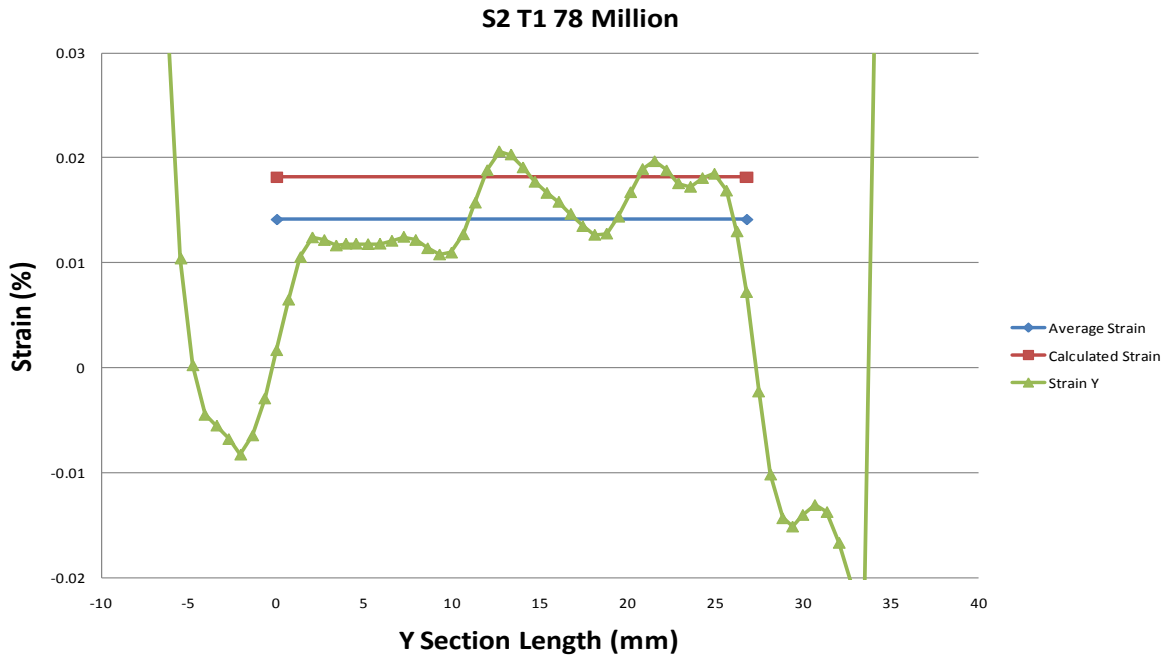


Figure 75: Strain data compared to the average strain and calculated strain for the specified section length for S2 T1 after 78 million cycles

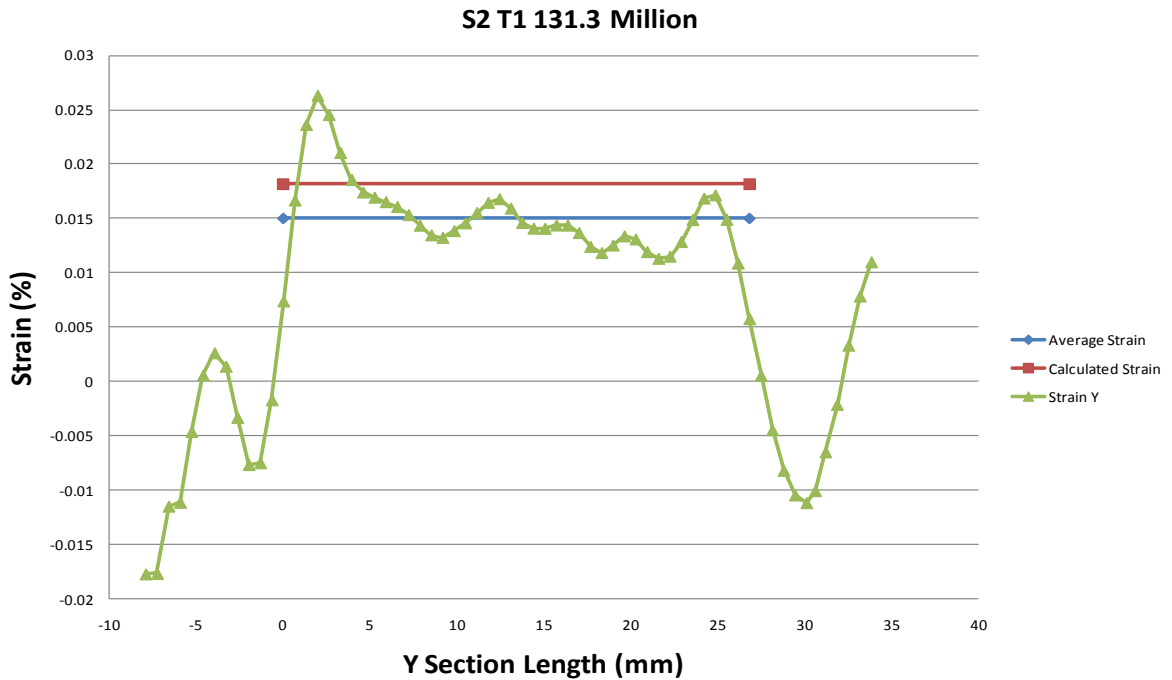


Figure 76: Strain data compared to the average strain and calculated strain for the specified section length for S2 T1 after 131.3 million cycles

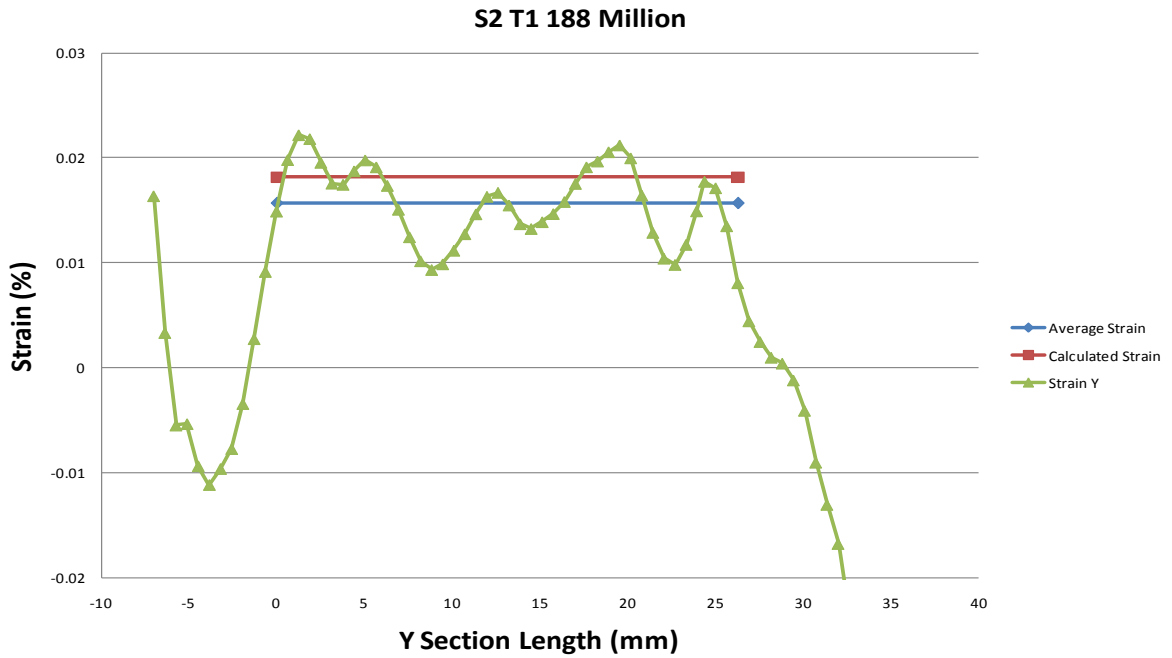


Figure 77: Strain data compared to the average strain and calculated strain for the specified section length for S2 T1 after 188 million cycles



Figure 78: Strain data compared to the average strain and calculated strain for the specified section length for S2 T1 after 250 million cycles

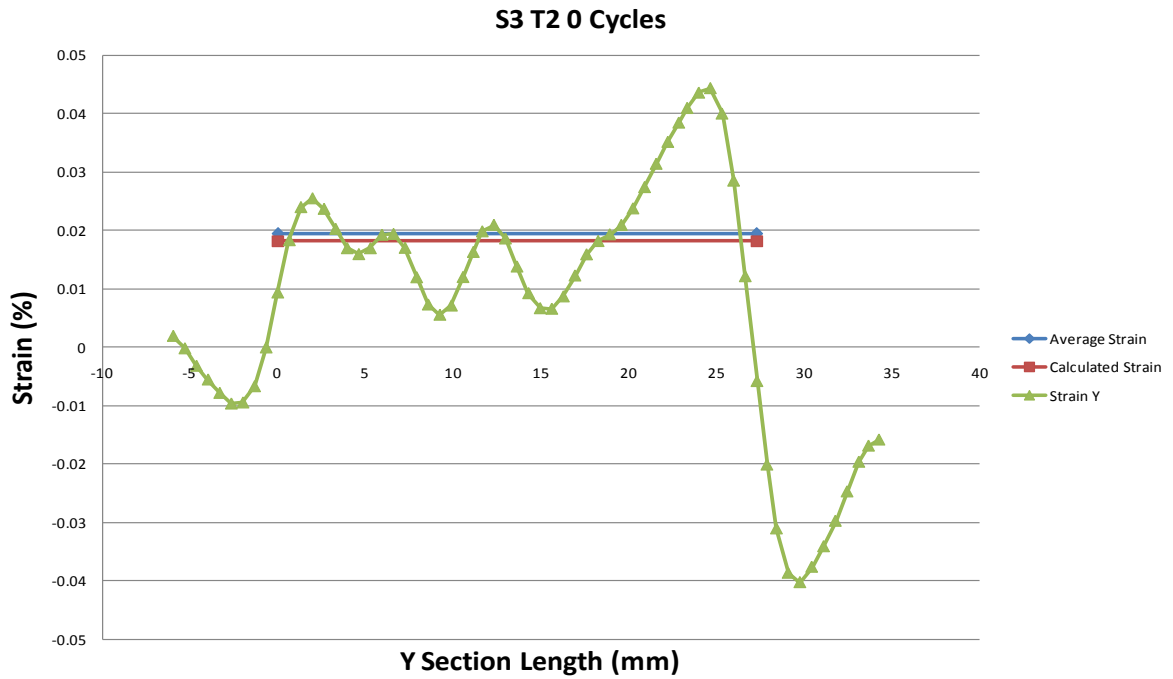


Figure 79: Strain data compared to the average strain and calculated strain for the specified section length for S3 T2 after 0 cycles

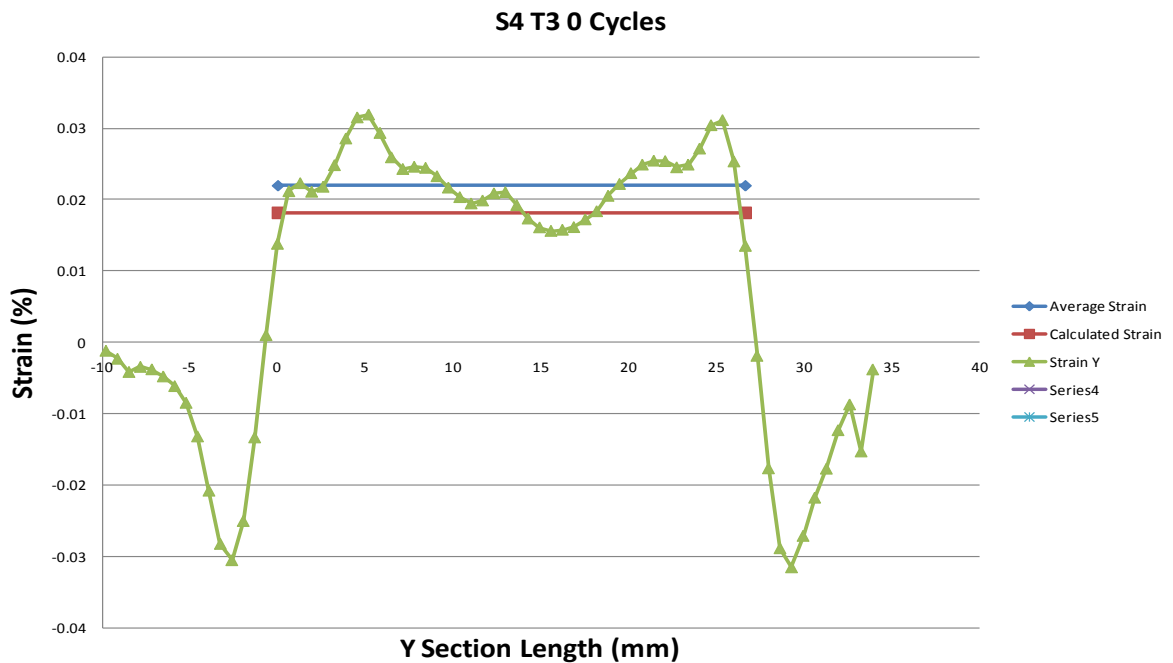


Figure 80: Strain data compared to the average strain and calculated strain for the specified section length for S4 T3 after 0 cycles

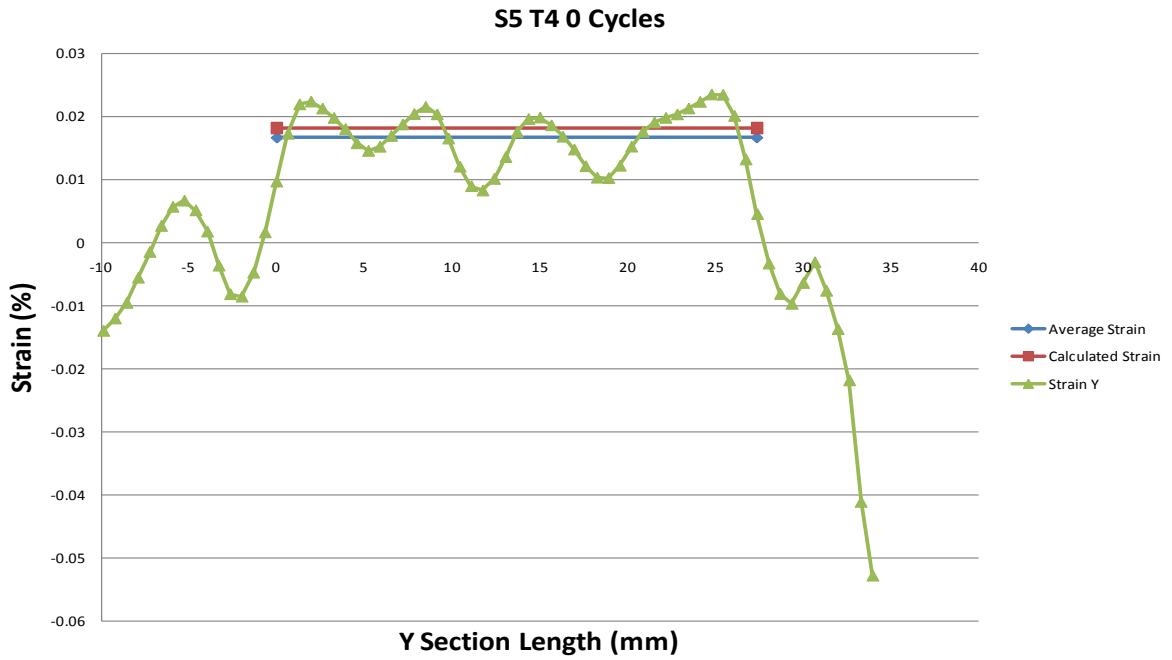


Figure 81: Strain data compared to the average strain and calculated strain for the specified section length for S5 T4 after 0 cycles

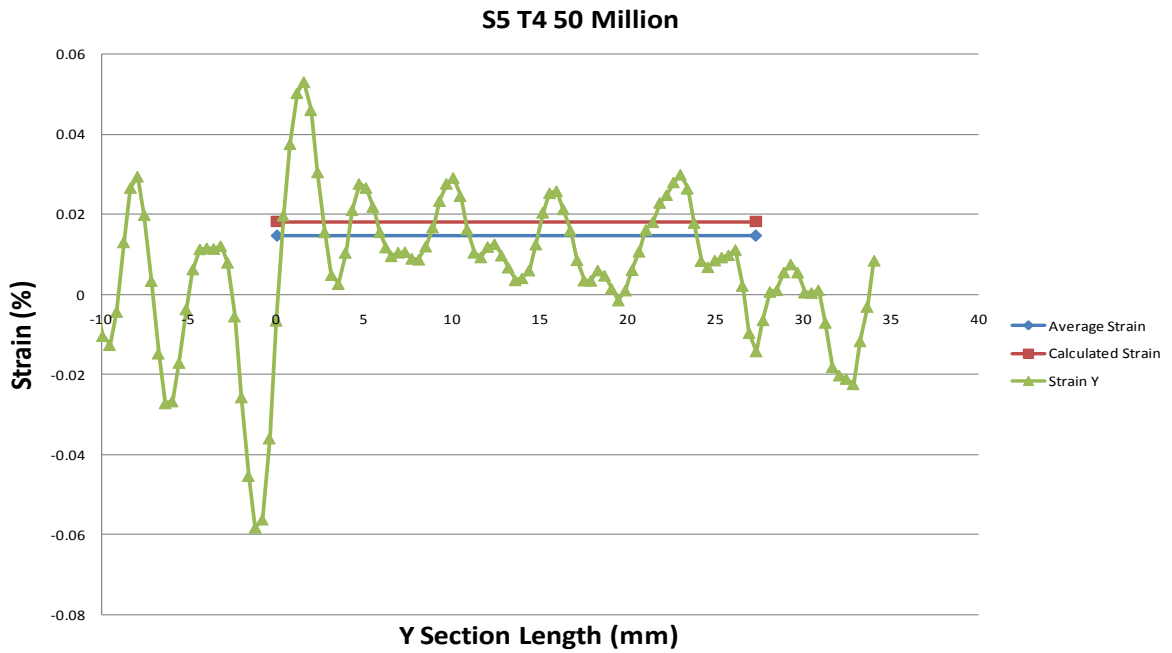


Figure 82: Strain data compared to the average strain and calculated strain for the specified section length for S5 T4 after 50 million cycles

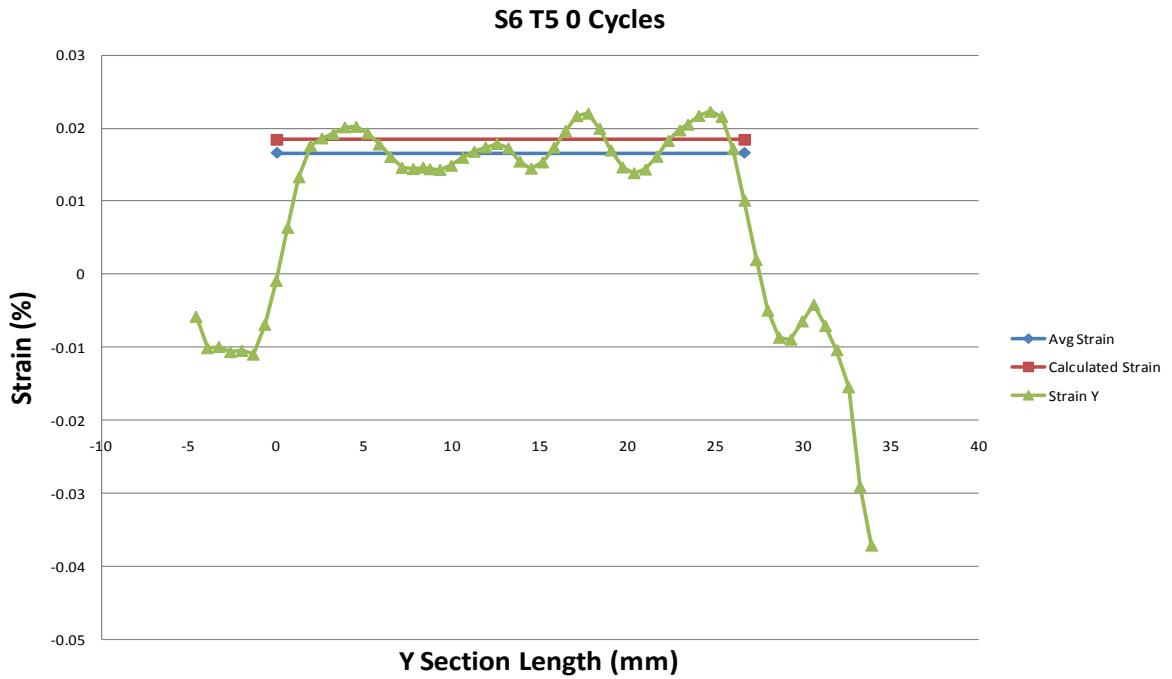


Figure 83: Strain data compared to the average strain and calculated strain for the specified section length for S6 T5 after 0 cycles

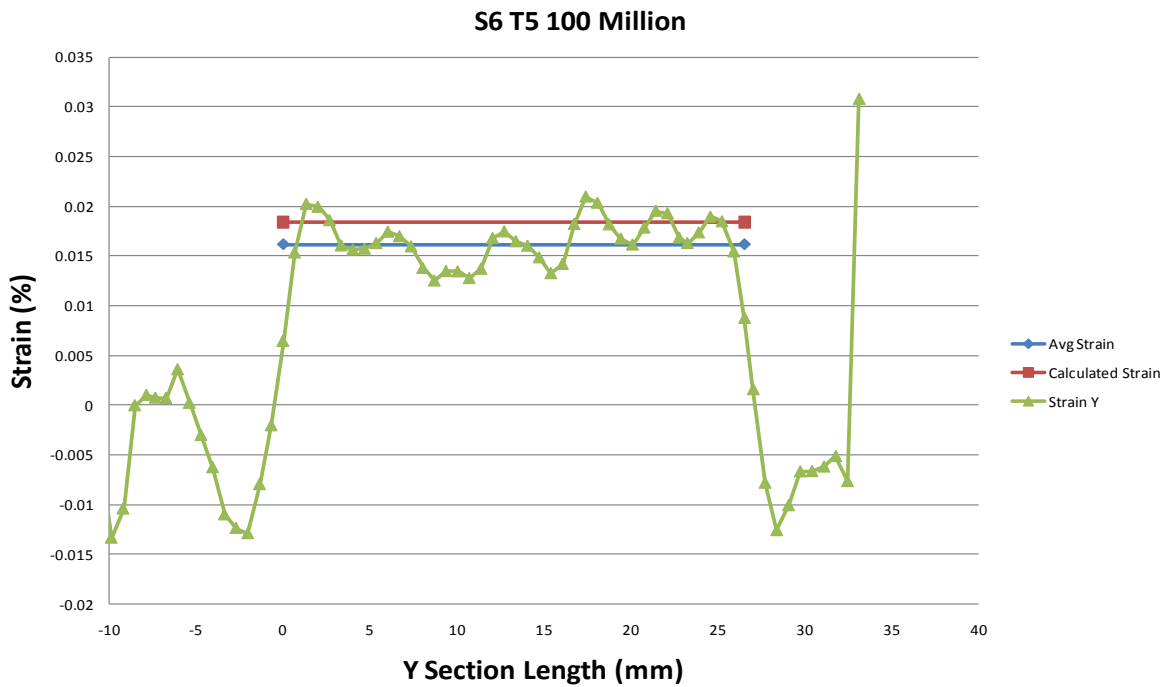


Figure 84: Strain data compared to the average strain and calculated strain for the specified section length for S6 T5 after 100 million cycles

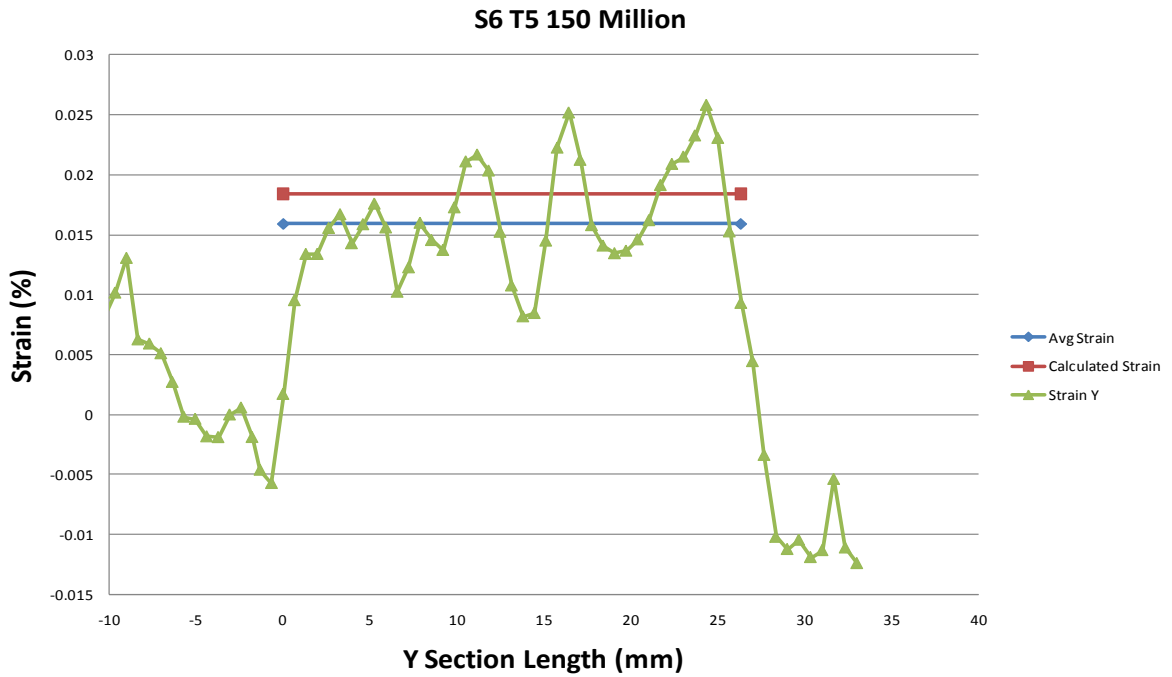


Figure 85: Strain data compared to the average strain and calculated strain for the specified section length for S6 T5 after 150 million cycles

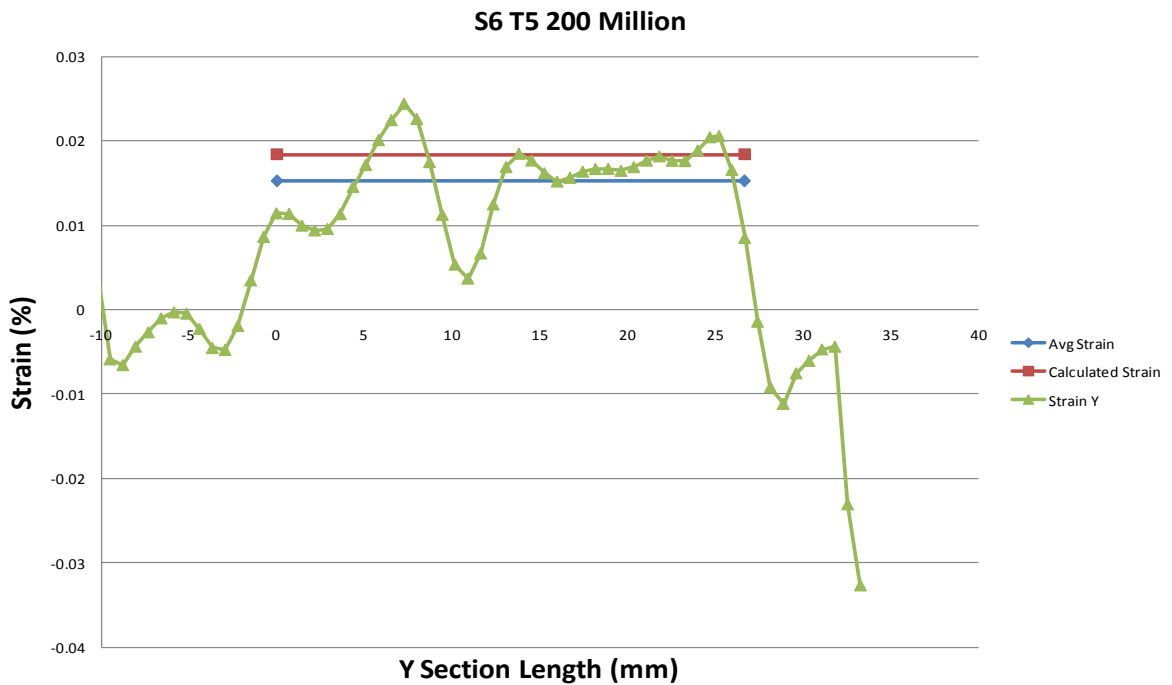


Figure 86: Strain data compared to the average strain and calculated strain for the specified section length for S6 T5 after 200 million cycles

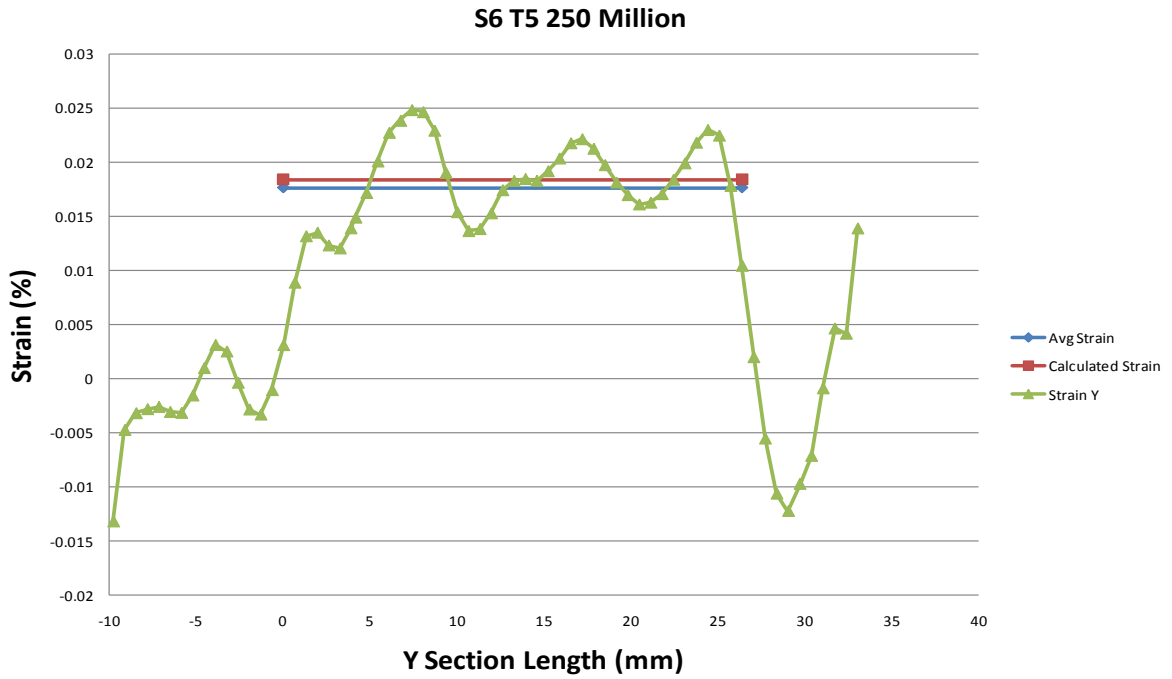


Figure 87: Strain data compared to the average strain and calculated strain for the specified section length for S6 T5 after 250 million cycles

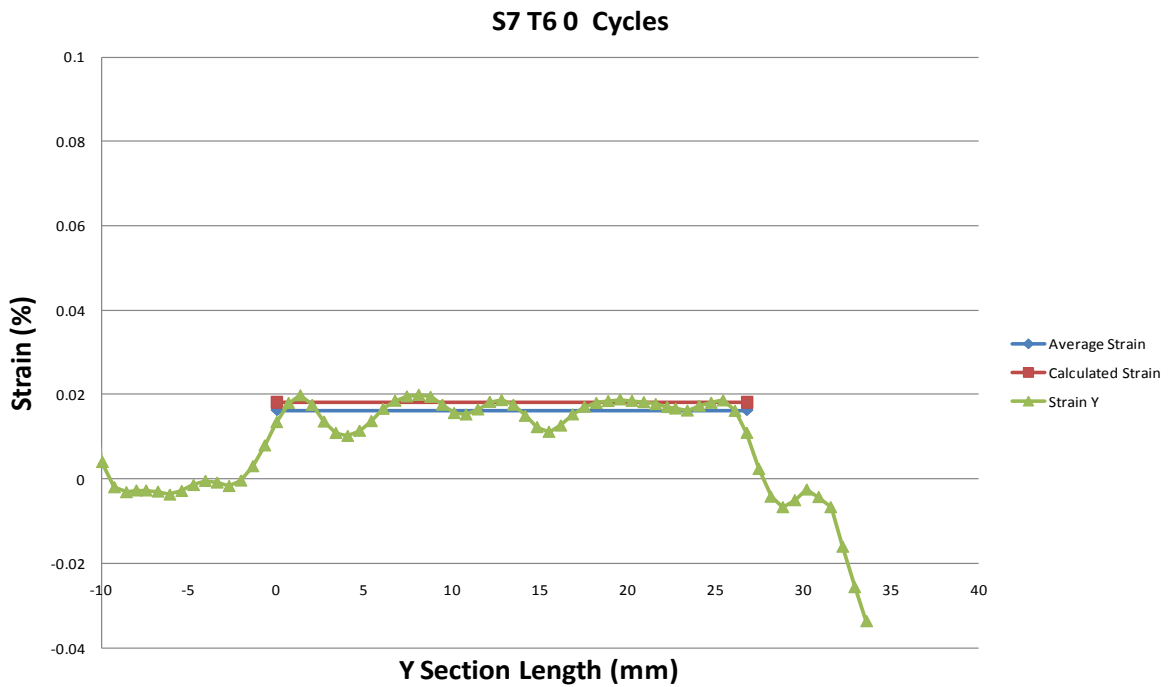


Figure 88: Strain data compared to the average strain and calculated strain for the specified section length for S7 T6 after 0 cycles

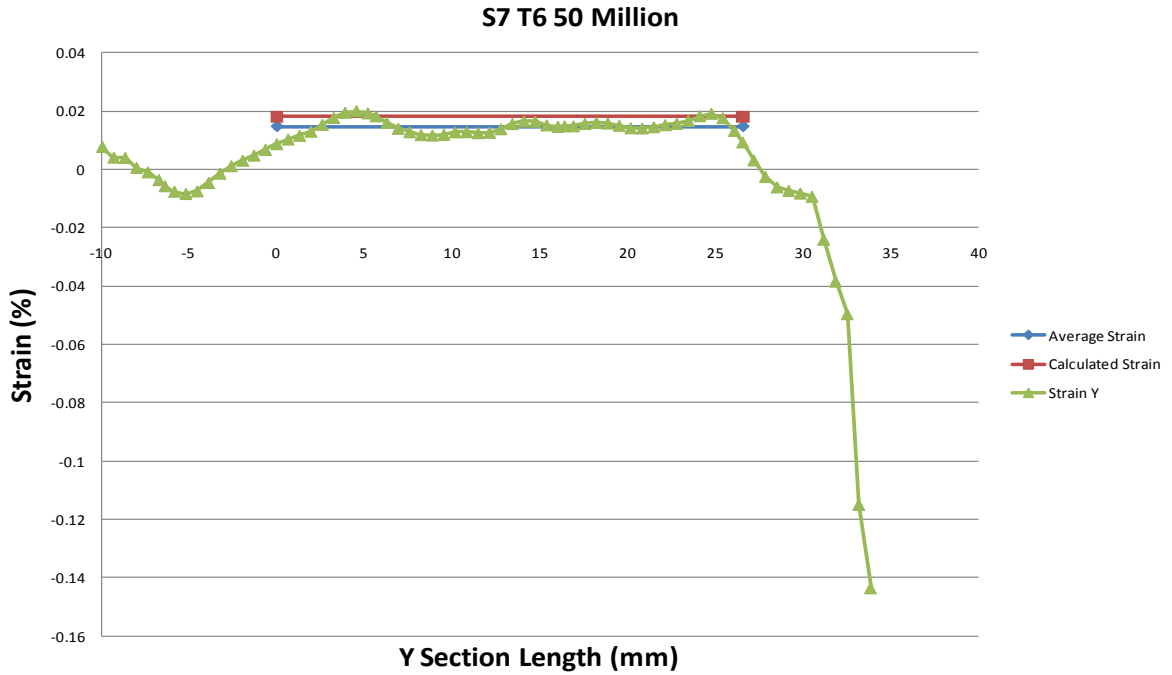


Figure 89: Strain data compared to the average strain and calculated strain for the specified section length for S7 T6 after 50 million cycles

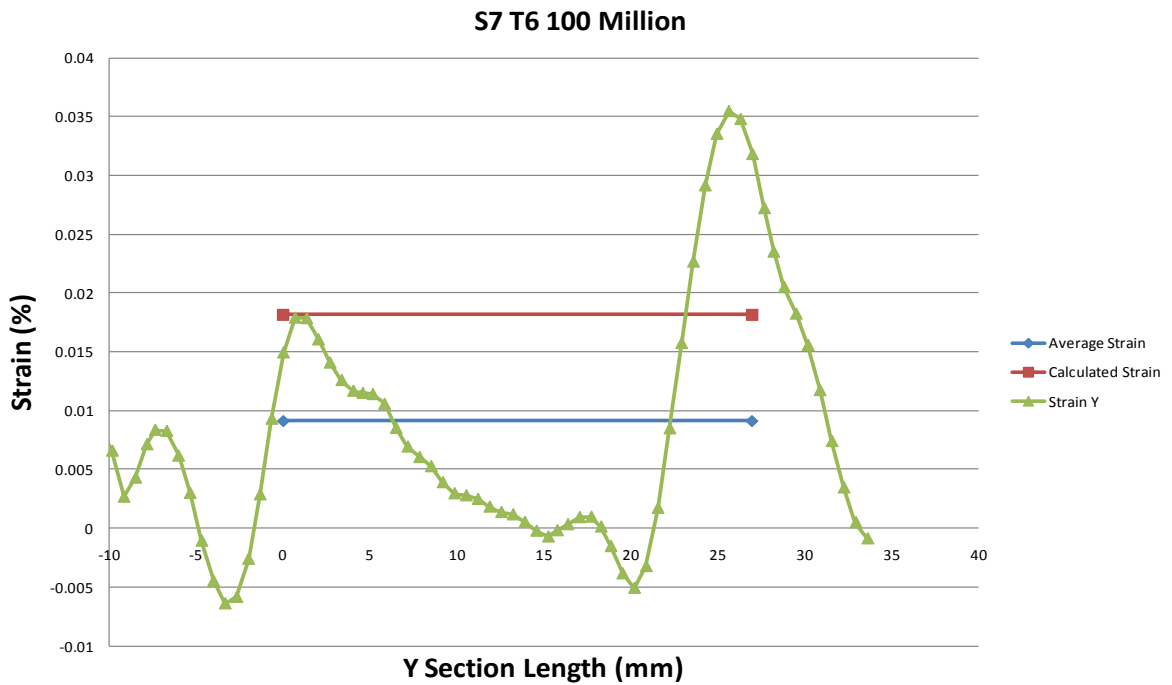


Figure 90: Strain data compared to the average strain and calculated strain for the specified section length for S7 T6 after 100 million cycles

S2 T1

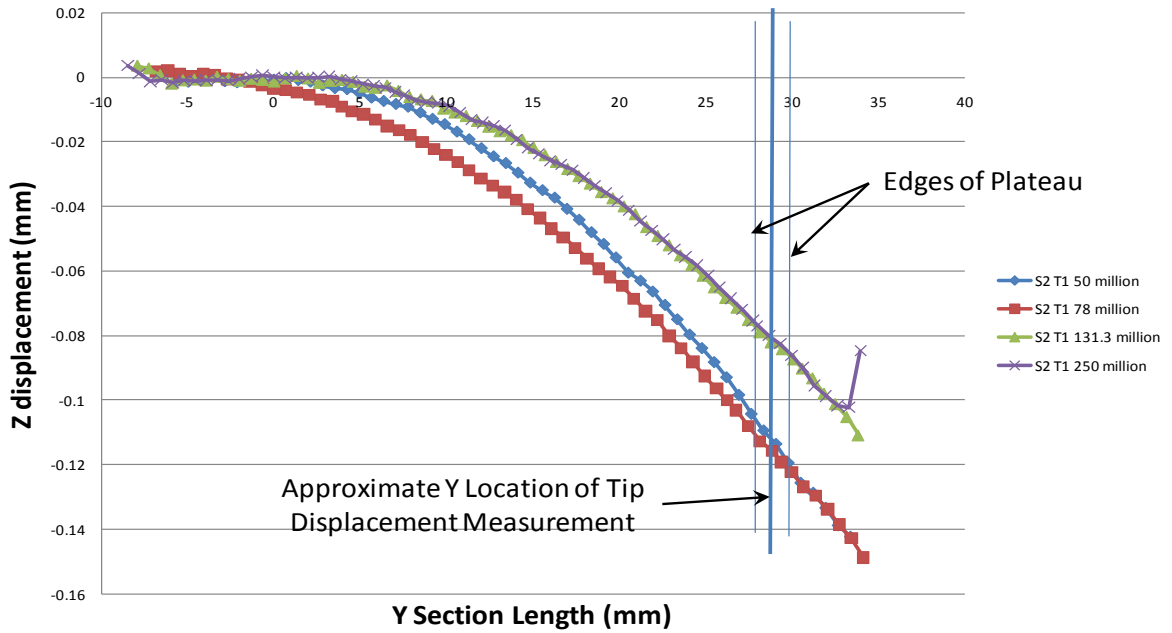


Figure 91: Z displacement data showing edges of the plateau used to measure the tip displacement, as well as the approximant location of the tip displacement measurement for S2 T1

S3 T2

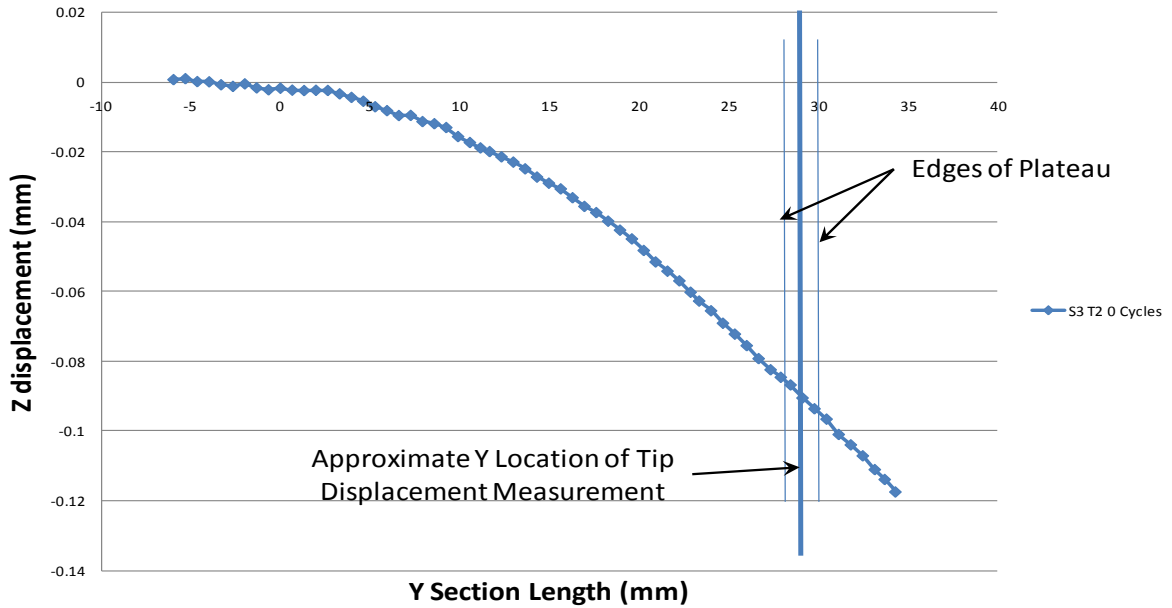


Figure 92: Z displacement data showing edges of the plateau used to measure the tip displacement, as well as the approximant location of the tip displacement measurement for S3 T2

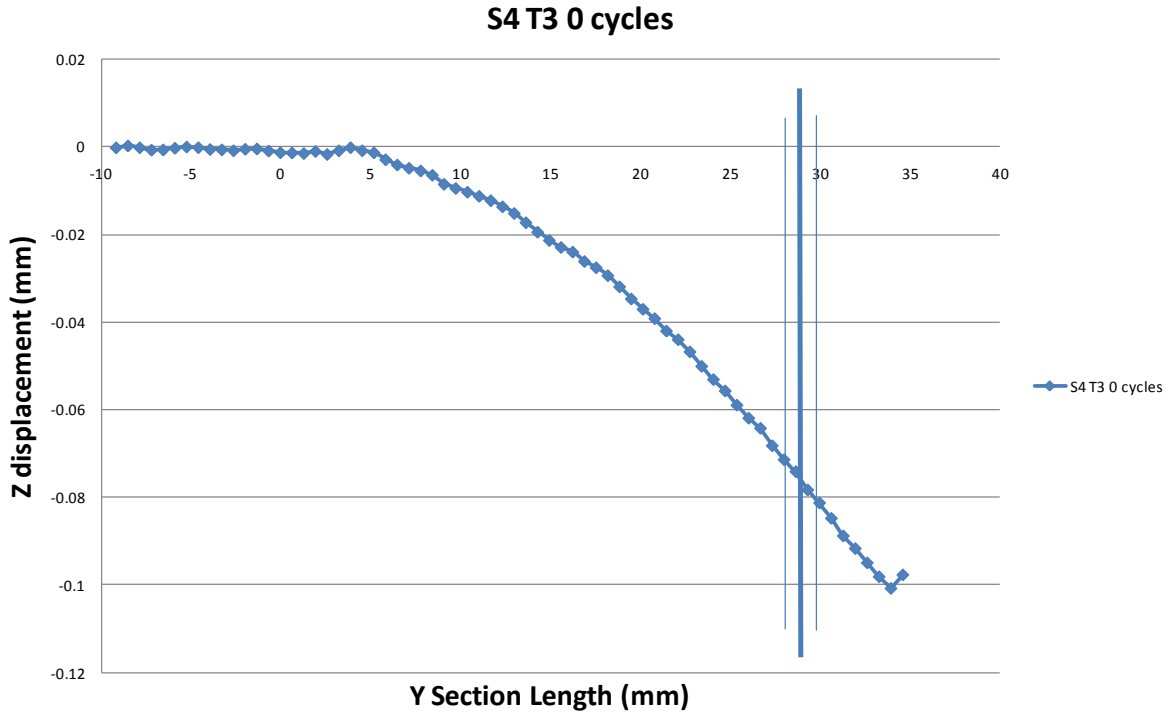


Figure 93: Z displacement data showing edges of the plateau used to measure the tip displacement, as well as the approximant location of the tip displacement measurement for S4 T3

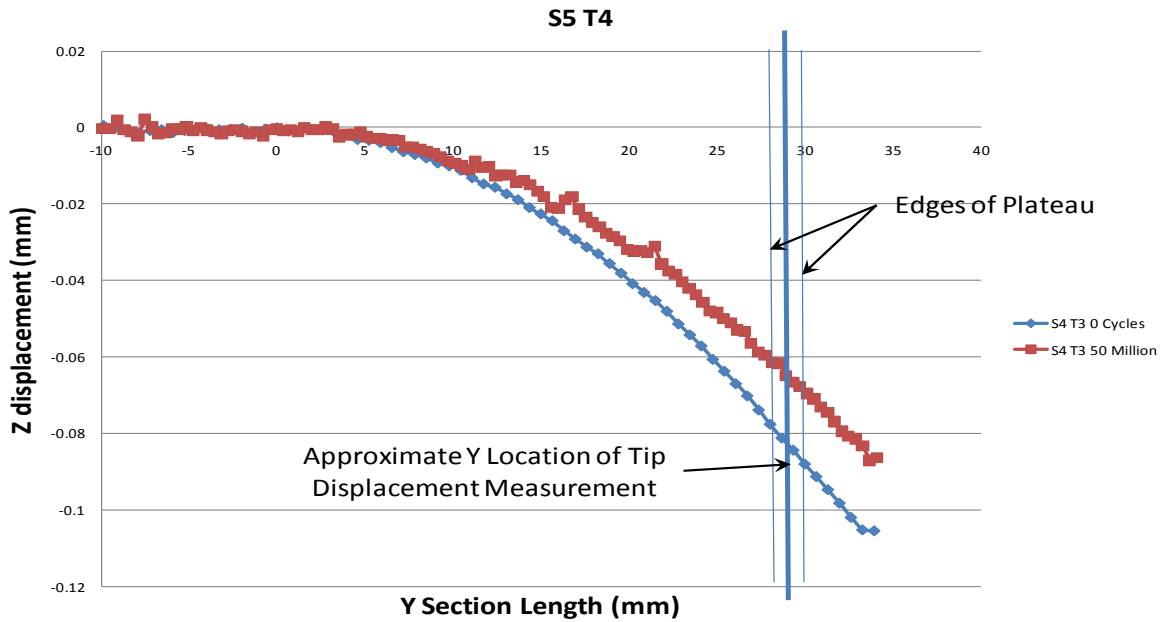


Figure 94: Z displacement data showing edges of the plateau used to measure the tip displacement, as well as the approximant location of the tip displacement measurement for S5 T4

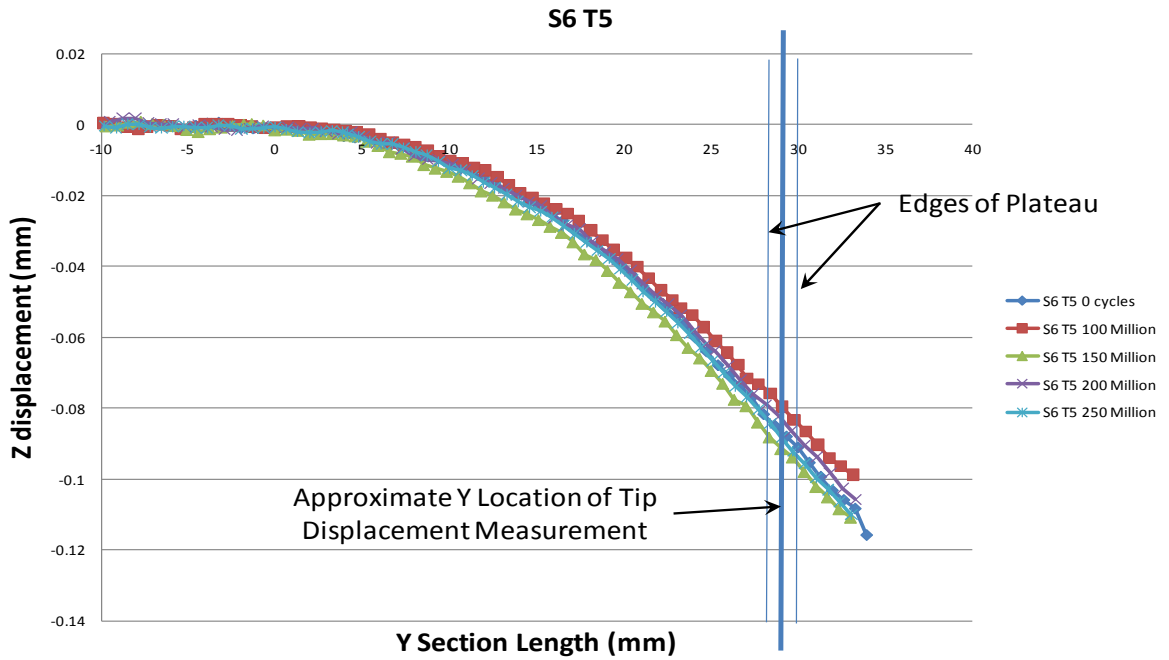


Figure 95: Z displacement data showing edges of the plateau used to measure the tip displacement, as well as the approximant location of the tip displacement measurement for S6 T5

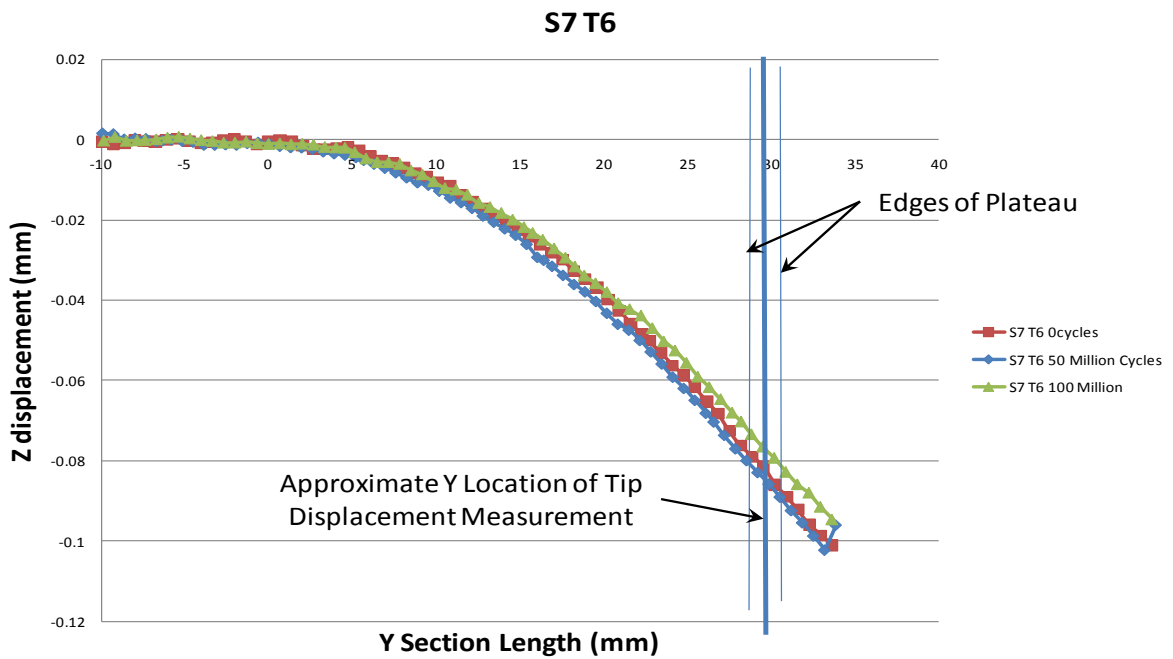


Figure 96: Z displacement data showing edges of the plateau used to measure the tip displacement, as well as the approximant location of the tip displacement measurement for S7 T6